$l.1$

NASA TN D-3516

PRESSURE DISTRIBUTIONS DUE TO TWO-DIMENSIONAL FABRICATION-TYPE SURFACE ROUGHNESS ON AN OGIVE CYLINDER AT TRANSONIC SPEEDS

by K. R. Czarnecki and William J. Monta

Langley Research Center
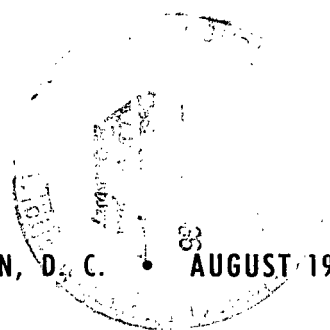Langley Station, Hampton, Va.

NASA TN D-3516

PRESSURE DISTRIBUTIONS DUE TO TWO-DIMENSIONAL

FABRICATION-TYPE SURFACE ROUGHNESS ON AN

OGIVE CYLINDER AT TRANSONIC SPEEDS

By K. R. Czarnecki and William J. Monta

Langley Research Center
Langley Station, Hampton, Va.

NATIONAL AERONAUTICS AND SPACE ADMINISTRATION

PRESSURE DISTRIBUTIONS DUE TO TWO-DIMENSIONAL

FABRICATION-TYPE SURFACE ROUGHNESS ON AN

OGIVE CYLINDER AT TRANSONIC SPEEDS

By K. R. Czarnecki and William J. Monta
Langley Research Center

SUMMARY

An investigation has been made in the transonic Mach number range from 0.70 to 1.20 and over a range of free-stream Reynolds number per foot from about 0.8×10^6 to 6.0×10^6 to determine the pressure distributions over essentially two-dimensional fabrication-type surface roughness immersed in a turbulent boundary layer. Six types of surface roughness, including step, wave, crease, and swept configurations, were investigated. The tests were made on an ogive cylinder of fineness ratio 12.2, the roughness elements covering the cylindrical portion of the model. The results have been examined with the objective of establishing the basic types of flow phenomena over the roughness elements so that the proper theoretical and empirical methods of investigating the phenomena of roughness drag in more detail can be delineated.

Examination of the subsonic results in the form of longitudinal pressure distributions did not indicate the process by which drag is generated subsonically, but did show the need for developing theories for predicting pressure for arbitrary roughness shapes at these speeds. At transonic and supersonic Mach numbers, the pressure distributions indicated the generation and expansion of local supersonic flows over the roughness elements with the onset of supersonic wave drag. Similarities in the effects of Mach number, free-stream Reynolds number per foot, and between longitudinal stations suggested that it may be possible to correlate the surface roughness drags, if not the pressures, in terms of the local boundary-layer profile characteristics and roughness height and shape.

INTRODUCTION

As part of a program to provide design information for supersonic aircraft, a general investigation is being made at the Langley Research Center to determine the effects of fabrication-type surface roughness on turbulent skin friction. Various techniques, including model force tests, roughness-element surface pressure distributions, boundary-layer profile surveys, and schlieren photography, are being utilized in this research. The

tests are being conducted in a variety of facilities and over a wide range of operating conditions. Some of the results obtained in this investigation have been presented in references 1 to 5.

Analysis of the aforementioned results disclosed that, at supersonic speeds, the greatest component of drag due to surface roughness in a turbulent boundary layer is contributed by pressure or wave drag. (See refs. 4 and 5.) Theoretical considerations further indicated that this wave drag would be greatest and subject to the most complex Mach-number—boundary-layer interactions near sonic velocity. Consequently, it was deemed desirable to extend the investigation to turbulent boundary layers in the transonic-flow regime. This paper presents the pressure distributions and schlieren photographs obtained in these transonic-flow tests. The objective of the presentation is to establish the basic types of flow phenomena over the roughness elements so that proper theoretical and empirical methods of investigating the phenomena of roughness drag in more detail can be delineated.

The pressure-distribution tests were made on six types of fabrication roughness built into the cylindrical portion of an ogive cylinder with a fineness ratio of 12.2 and on a smooth-surface reference model. The tests were made over a Mach number range from 0.70 to 1.20 and over a range of free-stream Reynolds number per foot from about 0.8×10^6 to 6.0×10^6. The model axis was always alined with the free stream, and turbulent boundary-layer flow was assured by means of a carborundum-grain trip near the tip of the model nose. Where appropriate, a comparison has been made of the experimental pressures with linearized subsonic or supersonic theory.

SYMBOLS

C_p pressure coefficient, $\dfrac{p_l - p_\infty}{q_\infty}$

ΔC_p increment in pressure coefficient between basic smooth body and model with surface roughness

h height of roughness element from mean smooth surface

l length of one-half cycle of roughness element

M_l local Mach number just outside the boundary layer

M_∞ free-stream Mach number

p_l local static pressure

2

p_t free-stream stagnation pressure

p_∞ free-stream static pressure

q_l local dynamic pressure just outside the boundary layer

q_∞ free-stream dynamic pressure

R radius of ogive

R/ft free-stream Reynolds number per foot

r local model radius measured normal to body axis

r_m mean radius of cylindrical portion of models with surface roughness elements

x axial distance from model nose

x_1 axial distance downstream from point where surface of roughness element crosses mean radius of cylindrical portion of model with negative or rearward slope

δ estimated total boundary-layer thickness

APPARATUS AND METHODS

Wind Tunnel

This investigation was conducted in the Langley 8-foot transonic pressure tunnel (ref. 6), which is a single-return closed-circuit pressure tunnel, capable of operating at stagnation pressures from 0.25 to 2 atmospheres. The Mach number in the slotted test section, which is square, can be continuously varied from 0 to 1.20. The Mach number distribution without a model is reasonably uniform throughout the test-section length of about 5 feet with the maximum deviation from the average stream Mach number being on the order of ±0.005 at the subsonic Mach numbers to about ±0.02 at the highest test Mach numbers (ref. 7).

Models and Instrumentation

A 50.0-inch-long, 4.096-inch-diameter, 3-caliber-nose, ogive cylinder was the basic configuration of the seven sting-mounted models tested. One model was a plain or

essentially smooth ogive cylinder without roughness elements. (See fig. 1.) The remaining six models were smooth on the ogive sections, but each had a number of cycles of a particular type of fabrication roughness constructed into the whole length of the cylindrical portion of the body. (See figs. 2 and 3.) These roughness cycles included steps with grooves, rearward-facing steps, creases, and protruding waves, each having a nearly constant cycle length of from 1.5 to 4.0 inches and a constant height of from 0.014 to 0.053 inch. The heights of the various roughness elements were selected to represent fabrication imperfections found on recent production transonic aircraft of aluminum construction, and the cycle lengths were chosen to provide enough cycles on models (table I) so that a measurable difference in drag would be obtainable in the related force tests. On four of these models the roughness cycles were wrapped around the model unswept; on the reamining two, they were swept 45°. The relationship of the maximum roughness height to the estimated total boundary-layer thickness (by the method of ref. 8) is shown in figure 4 for $M_\infty = 1.00$. There was little change for the other Mach numbers.

The plain ogive cylinder was constructed of aluminum and uniformly roughened to 85 microinches with scratches similar to those made by a lathe tool. Previous tests (for example, see ref. 3) have already indicated that the skin friction of this model is identical to that of an ogive cylinder with a smooth (5 to 6 microinch) surface. The remaining models were made of wood covered with Paraplex and fiber glass. The first 2 inches of the nose of each of the fabrication-roughness ogive cylinders were aluminum in order to minimize tip damage.

The surface finish of all the models except that of the plain ogive cylinder was very smooth, usually less than 10 microinches. Small scale waviness was often present on the models - superimposed on some of the roughness cycles. Although this condition prevented all cycles on any model from being identical, the deviations from the desired contours were generally few enough and small enough to have no influence upon the conclusions drawn from these tests.

Each model was instrumented with a number of static-pressure orifices (see table II) in a single row parallel to the model center line. The plain ogive cylinder had 34 orifices. The fabrication-roughness ogive cylinders had orifices usually located along the second and next-to-last cycles of roughness on each model. There were 12 to 20 orifices per station with one or two orifices on adjacent cycles for comparison. A greater number of orifices was utilized in this investigation than in that made on the identical roughness models in reference 4, because analysis of the latter results had indicated a need for more adequate surface coverage.

Other instrumentation consisted of a tetrabromoethane (specific gravity of 2.95) manometer board to register model pressures, a 9-inch camera to photograph the

manometer board, and several precision automatic indicating manometers for measuring reference pressures.

Test Methods

All tests were made at an angle of incidence of 0° with a fully turbulent boundary layer, transition being promoted by No. 60 carborundum grains cemented to the model 0.75 inch from the tip. All data were obtained with the tunnel conditions being held in equilibrium. During all runs the dewpoint temperature was maintained low enough to prevent condensation effects.

During the tests a strong effort was made to allow for the inherent lag in the response of the orifice and pressure-tubing system connected to the manometer boards and to insure enough time for the liquid levels on the manometer boards to reach full equilibrium before the boards were photographed. Subsequent evaluation of the data indicated that this objective was not always achieved for all the models at the lowest stagnation pressure of 500 psf where the lag problem was most severe. In such cases the levels of the pressure-distribution curves were too high or too low according to how the test condition was approached, and, consequently, some pressure distributions taken at 500 psf have been omitted.

Range of Tests

Tests were made on each model at Mach numbers of 0.70, 0.90, 1.00, 1.10, and 1.20. Data were taken at nominal stagnation pressures of 3000, 2000, 1000, and 500 pounds per square foot absolute. The Reynolds numbers per foot corresponding to these pressures vary with Mach number and range from about 0.8×10^6 to 5.0×10^6 at $M_\infty = 0.70$ and from about 1.0×10^6 to 6.0×10^6 at $M_\infty = 1.20$. Stagnation temperature was maintained at a value of $120^O \pm 2^O$ F throughout the tests.

RESULTS AND DISCUSSION

Pressure Distributions Over Smooth Reference Model

The pressure distributions determined for the essentially smooth-surface reference model are presented in figure 5. A solid line has been faired through the average data at each Mach number. These average curves are used as reference pressures in presenting distributions over the roughness elements in the next section. An experimental reference was chosen because it would eliminate any errors or distortions in making comparisons or theoretical estimates that might occur if an erroneous theoretical reference were used. An experimental reference also incorporates tunnel-flow disturbances which cannot be readily included in theoretical calculations. The approximate locations

of the stations at which pressure distributions were determined over the roughness elements on the other test models are shown by the braces.

An examination of the pressure distributions at each Mach number indicates that, just as was found for Mach numbers 1.61 and 2.01 in reference 4, there is no significant effect of stagnation pressure, and hence Reynolds number, for the range of Reynolds number per foot of the tests. The results also indicate that there is a recompression shock on the model at $x = 24$ inches at $M_\infty = 1.0$ and that the nose shock is reflected back onto the model at the supersonic Mach numbers. The impingement location of the reflected shock varies from an x of about 30 inches at $M_\infty = 1.1$ to an x of about 48 inches at $M_\infty = 1.2$.

In general, the forward roughness elements over which pressures were measured were located in a region of adverse pressure gradient. The rearward elements were generally in a region of favorable pressure gradient, and, at $M_\infty = 1.20$, some configurations were also located in a region of shock impingement and shock—boundary-layer interaction.

Pressure Distributions Over Roughness Elements

The pressure distributions determined over the roughness elements are presented in figures 6 to 11 as C_p plotted against x with the stagnation pressure p_t as the parameter at constant Mach number and in figures 12 to 17 as ΔC_p plotted against x with Mach number as the parameter at constant p_t. In the latter case only the results for the highest stagnation pressures and for the lowest stagnation pressures for which the lag problem was generally not too severe were used. Included in each figure is a plot of the surface profile at the measuring station, the vertical scale of the profile expanded by a factor of 25 relative to the horizontal scale to simplify a comparison of the various surface shapes and to enable a recognition of local surface irregularities. Also included in most figures for the data at constant Mach number are the smooth-body experimental pressure distributions (long dashes), the theoretical roughness pressure distributions (short dashes), and a theoretical sonic-flow line (where it fits within the graph). The sonic-flow line was computed by assuming that there were no nose-shock stagnation-pressure losses.

The supersonic theory was calculated from linearized two-dimensional methods. The theoretical pressure distributions for the supersonic Mach numbers were obtained by combining the experimental pressure coefficients for the plain model with the increments in pressure coefficient computed for the roughness element by two-dimensional linearized theory as shown by the expression

$$\left(C_p\right)_{\text{roughness model}} = \left(C_p\right)_{\text{plain model}} + \frac{2 \text{ (local slope of roughness)}}{\sqrt{M_l^2 - 1}} \frac{q_l}{q_\infty}$$

where M_l and q_l are the experimental local Mach number and dynamic pressure just outside the boundary layer on the plain model at about the axial location of the midpoint of the roughness elements and $\left(C_p\right)_{\text{plain model}}$ is the experimental pressure-coefficient distribution over the area of interest on the basic or smooth model. In essence, the increment in pressure coefficient due to roughness was computed on the basis of the average experimental conditions existing on the smooth body at the roughness-element location and this increment was then corrected to free-stream reference conditions. The exact procedure for making the theoretical calculations and some justification for the use of this approach are presented in reference 4. It should be noted that the vertical theoretical lines of the step-type configurations (figs. 6 and 10) for the faces perpendicular to the free stream have ended arbitrarily and merely signify an expansion or compression of unknown peak value.

The subsonic theory is presented only for the 0.053-inch protruding waves and is computed for a sinusoidal wave roughness by three-dimensional theory for an infinite number of repeating waves. Subsonic theoretical pressure distributions were derived in a manner similar to the supersonic distributions by combining the experimental pressure coefficients for the plain model with the theoretical increments in pressure due to the roughness. The incremental pressure coefficients were obtained by utilizing the subsonic theory for a series of identical sinusoidal waves on a cylinder due to Reissner (ref. 9) as presented in reference 10, page 75. The final equation used was

$$\left(C_p\right)_{\text{roughness model}} = \left(C_p\right)_{\text{plain model}} - \frac{2\pi}{\sqrt{1 - M_l^2}} \frac{h}{l} \frac{K_0\left(\pi \sqrt{1 - M_l^2} \frac{r_m}{l}\right)}{K_1\left(\pi \sqrt{1 - M_l^2} \frac{r_m}{l}\right)} \cos\left(\frac{\pi x_1}{l}\right) \frac{q_l}{q_\infty}$$

where the subscript l denotes local conditions just outside the boundary layer on the plain model at the axial location of the midpoint of the roughness element and K_0 and K_1 are modified Bessel functions of the second kind of zero and first order, respectively.

Transverse step-type roughness.- The experimental pressure distributions and incremental pressures over the model with 0.021-inch transverse steps with grooves indicate that at subsonic speeds (figs. 6(a), 6(b), and 12) negative pressure increments are induced (relative to those for the smooth model) over those portions of the roughness elements projecting above the mean line and positive pressure increments are induced over those portions recessing below the mean line of the roughened surface. Except for being

inverted in direction, the shapes of the incremental pressure distributions induced by the projecting surfaces are similar to those induced by the recessing surfaces. Immediately behind the forward-facing step corner and ahead of the rearward-facing step corner there is a strong acceleration of the flow.

At either roughness station the effects of stagnation pressure or R/ft are small, except in areas close to the actual steps or corners, with the change in pressure level occurring at $p_t = 997$ psf at $M_\infty = 0.70$ (fig. 6(a)) being ascribed to lag. The lag problem was acute on this model and necessitated the omission of data taken at $p_t = 500$ psf. In the comparison of stations 1 and 2, however, it is noted that the negative pressure peaks at the corners of the projecting surface are smaller at station 2 than at station 1. The explanation can be found readily by examination of figure 4. From this figure it is apparent that the boundary-layer thicknesses at station 2, even at the highest R/ft, were larger than the boundary-layer thicknesses at station 1 over the range of R/ft investigated. In particular, the boundary-layer thickness at station 2 is about 75 percent larger at a R/ft of 6×10^6 than the thickness at station 1 at a R/ft of 1×10^6. Apparently, it is the ratio of roughness height to boundary-layer thickness that is the significant parameter in determining the flow characteristics over the roughness element.

As the Mach number is increased from 0.70 to 0.90 (figs. 6(a), 6(b), and 12), there is usually an increase in the magnitude of the pressure increments induced by the presence of the roughness. A further increase in M_∞ to 1.00 (figs. 6(c) and 12) continues this general trend but also changes the character of the flow ahead of the forward-facing step at station 1 (x = 16 inches) so that the pressure rise begins much further ahead and is more gradual. This phenomenon is probably related to the generation of a detached shock. Also, the compression just behind the rearward-facing step is replaced by an expansion. Further increases in M_∞ initiate this same flow change at station 2 (figs. 6(d) and 12), decrease the magnitude of the flow expansion at the forward corner of the protruding surfaces, and force the pressures over the central portions of the cylindrical surfaces to conform more closely with the pressure distributions for the basic smooth model (figs. 6(d), 6(e), and 12). The latter trend is in accordance with the theoretical indications (two dimensional) that surfaces parallel to the median line or basic model contour will not induce increments in pressure at supersonic speeds, and all are in agreement with the trends determined experimentally on this model at $M_\infty = 1.61$ and 2.01 (ref. 4). Finally, the data indicate that as M_∞ is increased from 1.00 (see data in ref. 4 also), the pressure rise ahead of the forward-facing step is progressively concentrated closer to the face of the step in accordance with the movement of the detached shock closer to the step face. This trend is interrupted only by nose shock impingement at station 2 at $M_\infty = 1.2$.

Transverse wave-type roughness.- The experimental pressure distributions and incremental pressures for the transverse wave-type roughness (figs. 7 to 9 and 13 to 15) go

through alternate cycles of increasing and decreasing pressures at subsonic Mach numbers. Negative increments in pressure are induced on those portions of the roughness protruding above the mean cylinder surface and positive increments in pressure are induced on those portions recessing below the mean surface just as for the step configuration. The exact shape of the pressure distributions is dependent upon the shape of the roughness and Mach number. For the approximately sinusoidal roughness elements (figs. 7 and 13), the variation in pressure with x is relatively smooth. For the waves with the relatively low-curvature or flat-top surfaces and sharp troughs (figs. 8, 9, 14, and 15), the experimental pressure distributions show somewhat slower changes in pressure over the outer or top surfaces and very abrupt reversals in pressure in the troughs or valleys. At subsonic Mach numbers (parts (a) and (b) of figs. 7 to 9) the shapes of the pressure distributions conform remarkably well (except for a scale factor) with the shapes and phase relationships of the roughness elements. At $M_\infty = 0.70$, for the model with approximately sinusoidal waves, the increments in peak negative pressures generated by the roughness elements are slightly larger in magnitude than the increments in peak positive pressures. This trend is ascribed both to compressibility effects, which are greater on the negative pressures than on the positive pressures and to boundary-layer interaction effects. From considerations only of the departures of the surface contours from the smooth mean surface, the maximum increments would be expected to be equal. At the same Mach number for the models with the transverse creases (figs. 8(a), 9(a), 14, and 15), however, the peak increments in positive pressure are much larger than the peak increments in negative pressure. In these cases, the deviations of the surface contours from the mean smooth surface are greater in the troughs than over the top surfaces, so that the effects of compressibility and boundary-layer interaction are overcome. For all transverse wave configurations, the peak negative incremental pressures are smaller at station 2, where the boundary layer is thicker, than at station 1; this difference again emphasizes the importance of the ratio of roughness height to boundary-layer thickness in determining flow characteristics over roughness elements. The positive pressure increments, on the other hand, generally show much less change.

As M_∞ is increased from 0.70 to 0.90 there again is mainly an increase in the incremental pressures (parts (a) and (b) of figs. 7 to 9 and figs. 13 to 15) with the greatest change generally occurring in the regions of the negative pressures. A further increase in M_∞ to 1.00 (part (c) of figs. 7 to 9 and figs. 13 to 15) continues this general trend but also causes the negative pressure peaks to occur behind or downstream of the geometrical peaks. This downstream shift of the negative pressure peaks increases as the supersonic flow continues its expansion to a Mach number of 1.10 because of the availability of more space for the stream tubes behind the surface peaks, and it also signals the onset of supersonic wave drag. With a still further increase in Mach number, the flow expansion proceeds even farther downstream of the surface peak, but both the positive and negative

incremental peak pressure coefficients are usually reduced as is normally expected with increases in M_∞. (See parts (d) and (e) of figs. 7 to 9 and figs. 13 to 15.) For the model with the approximately sinusoidal roughness the expansion has proceeded to about the inflection point in the surface slope at $M_\infty = 1.20$ at the highest R/ft (fig. 13) and, as expected from theoretical considerations, further increases to $M = 1.61$ and 2.01 do not result in any further expansion (ref. 4). For the more flat-top or crease-type models the expansion does not proceed fully to the surface inflection point at $M_\infty = 1.20$ (figs. 14 and 15) or even at $M_\infty = 2.01$ at any R/ft (ref. 4), although the expansion continues to move further downstream very slowly with increasing M_∞. The occurrence of this flow expansion behind the peaks of the roughness elements at sonic and supersonic speeds also results in moving the peak recompression downstream of the trough toward the next inflection point in the surface profile. For the crease-type roughness configurations, the maximum recompression occurs close to the surface inflection point at even the low supersonic and sonic Mach numbers (figs. 14 and 15); for the sinusoidal-wave type configuration, it does not reach the inflection point until near $M_\infty = 1.6$ (fig. 13 and ref. 4). In essence, the local surface pressures for these wave-type surface-roughness elements appear to depend primarily upon the deviation of the local surface from the mean surface line at the subsonic speeds and to change gradually through the transonic Mach number regime to depend upon the local surface slope at supersonic speeds.

The effects of Reynolds number per foot, or of boundary-layer thickness, are generally much stronger for the wave-type surface roughnesses (figs. 7 to 9) than they are for the step-type roughness (fig. 6). Furthermore, the Reynolds number effects are most severe in the Mach number range from 1.00 to 1.20 and in the areas of supersonic expansion behind the surface geometric peaks and in the recompression areas of the troughs. Reynolds number effects are also largest for the highest surface waves, ostensibly because the largest roughnesses induced the largest changes in local pressure distributions and in the boundary-layer characteristics. In general, the effects of decreasing Reynolds number per foot are to decrease the increments in both negative and positive pressure in the affected regions. There is also a strong tendency, however, for decreasing R/ft to delay the supersonic expansion behind the surface peak and a weaker tendency to eliminate the recompression downstream of the trough at sonic and supersonic Mach numbers in a manner similar to the effects of decreasing the supersonic Mach numbers. This trend, coupled with a similar trend to be noted in going from station 1 to station 2, where the boundary layer is thicker, suggests that all these effects may be closely related and that it may be ultimately possible to correlate the surface roughness pressures in terms of the local boundary-layer velocity profiles and roughness height and shape. A physically oversimplified, and hence only partially successful, attempt to develop such a theory can be found in reference 11.

For the subsonic-flow case, a comparison of experiment with theory was possible only for the configuration with the approximately sinusoidal surface (fig. 7, parts (a) and (b)). This comparison shows that the agreement between the theoretical and experimental pressure distribution curves is not too good. The disagreement is ascribed primarily to the use of a theory for an infinite number of repeating waves whereas there are actually only a finite number. A small part of the disagreement can also be ascribed to the differences between the theoretical and experimental roughness shapes. Still other contributing factors may be the neglect of the perturbation velocities normal to the model surface in deriving the theoretical expression for the pressure coefficients (ref. 10, p. 78) and the use of first-order theory in estimating compressibility effects. (See discussion of compressibility effects in ref. 10, pp. 352-373.)

At the supersonic Mach numbers ($M_\infty = 1.10$ and 1.20) the experimental pressure distributions are in poor agreement with linearized theory for all wave configurations (parts (d) and (e) of figs. 7 to 9). The disagreement results from the fact that the supersonic-flow expansion downstream of the geometric surface peak does not proceed all the way to the next surface inflection point as was assumed to have occurred in the linearized supersonic theory, and this lack of expansion in turn reduces the amount of the following recompression. A comparison of these results with those of reference 4 indicates that the agreement between theory and experiment improves with increasing Mach number. From these trends and from theoretical considerations it is apparent that a large part of the discrepancy is due to the transonic nature of the flow and any accurate prediction of pressure distributions in the Mach number 1.00 to 1.20 range may require a transonic-flow approach. Again, it should be noted that the effects of decreasing Reynolds number per foot on the agreement between theory and experiment are very similar to the effects of decreasing Mach number. (Compare parts (d) and (e) of figs. 7 to 9 with figs. 13 to 15.) The effects of increasing ratio of boundary-layer thickness to roughness height are also similar to the effects of decreasing Mach number. It is apparent that these effects of boundary-layer thickness to roughness height are generally strong enough to require inclusion in any accurate theory for predicting the surface pressure distributions. Finally, some of the disagreement between theory and experiment may be ascribed to the use of two-dimensional theory instead of three-dimensional theory in this low supersonic Mach number range.

Roughness with sweep.- The pressure distributions for the roughness configurations with sweep (figs. 10, 11, 16, and 17) exhibit subsonic-flow characteristics throughout the test speed range. This means that, as for the unswept wave-type roughnesses at subsonic Mach numbers, the shapes of the pressure distributions closely follow (except for a scale factor) the contours of the roughness surface. The pressure distributions for these swept roughness configurations apparently do not change much in character until near $M_\infty = 1.61$ and do not approach good agreement with supersonic theory until a Mach

number of 2.01 (ref. 4). This agreement with supersonic theory is slower than was found for the unswept configurations. Sweeping the roughness element, therefore, does result in delaying the onset of compressibility effects. An analysis of the results on the basis of the component of local Mach number outside the boundary layer normal to the roughness element indicates that the onset of compressibility effects is in good agreement with those of the similar unswept configurations. Thus, it appears that it may be possible to treat long swept roughness elements on a two-dimensional basis at sufficient distances (as yet unknown) from the roughness apex or downstream ends.

The effects of changes in Reynolds number per foot on the pressure distributions for the roughness elements with sweep were small over the present Mach number range. The effects were small because, first, the roughness height was small and, consequently, as was noted for the unswept configurations, the ability of this roughness to affect the local pressures and boundary-layer characteristics was small. Second, the effects were small because the sweep of the roughness elements also delayed the appearance of the supersonic flow expansions behind the surface peaks, where the influence of Reynolds number per foot is greatest, to higher Mach numbers. The greatest effects of Reynolds number per foot would thus be expected to occur in the Mach number range from 1.5 to 2.0 This deduction is verified by the data of reference 4.

<center>Schlieren Photographs of Flows</center>

Schlieren photographs of the flows over the basic smooth model and over the various models with fabrication-type surface roughness are presented in figures 18 to 22. For the roughness configurations, the flows over the forward cylindrical portion of the model where station 1 is located are depicted in the (a) parts of the figures; the flows over the rear part of the model where station 2 is located are shown in the (b) parts of the figures. All schlieren photographs had to be limited to a vertical knife edge in the system; hence, it is difficult, if not impossible, to distinguish the actual boundary layer because the largest boundary-layer density gradients occur normal to the model surface and this direction is parallel to the knife edge. Frequent malfunctions resulted in the loss of many photographs, particularly those over the smooth model. Most of the photographs presented were obtained at the highest test stagnation pressure of 3000 psf. Inclusion of photographs obtained at lower stagnation pressures does not present any problems inasmuch as effects of Reynolds number per foot were generally indistinguishable.

Smooth reference model.- The schlieren photograph for the smooth reference model at $M_\infty = 1.2$ shows little of interest except that the model nose shock is reflected from the tunnel wall and impinges on the model just ahead of the base. This impingement apparently is not symmetrical around the model. The shock impingement has already been noted in the discussion of the smooth model pressure distributions (fig. 5).

12

Transverse step-type roughness.- The schlieren photographs of the flow over the model with 0.021-inch transverse steps with grooves (fig. 19) show areas of flow expansion (dark fans) at the forward-facing steps and flow compression (light fans) at the rearward-facing steps at the subsonic Mach numbers. The existence of such indications is readily explainable in terms of the existing pressure distributions (fig. 6). At the forward-facing step, the expansion is sharply concentrated at the upper corner of the step, whereas the compression is diffused for some distance forward of the step and for some distance behind the upper corner. Also, the total magnitude of the expansion is larger than the combined total of the compressions in this area. Hence, the expansion effects tend to predominate in the schlieren photographs for the forward-facing steps because the schlieren system is most sensitive to the sharpest pressure gradients. At the rearward-facing steps the exact reverse holds true.

At $M_\infty = 1.00$ the flow is definitely supersonic over the forward part of the model and essentially sonic over the rearward part. For the forward station, the schlieren shows an expansion at the rearward-facing step, followed by an oblique shock or compression at the point where the separated flow reattaches to the cylindrical surface a short distance behind the step face. At the upper corner of the forward-facing step, the schlieren shows an expansion with normal shocks standing some distance forward of the step faces. Similar trends appear on the model at the rearward station except that the oblique shocks are more nearly normal and there is generally no evidence of any detached normal shocks standing ahead of the step. (See fig. 6(c).)

The schlieren flows at the supersonic Mach numbers ($M_\infty = 1.10$ and 1.20) are similar to those discussed for station 1 at $M_\infty = 1.00$ except that the shocks are inclined more to the rearward and the detached shocks are closer to the forward-facing steps because of the higher local Mach numbers. In general, the shocks and expansions at station 2 (particularly at the forward-facing step) appear more diffuse, owing no doubt to the thicker boundary layer which allows greater leeway in positioning and softening the phenomena. Because of the lower Mach numbers within the boundary layer, the oblique shocks tend to become more of a normal shock in this region. From the much greater heights of these normal shock portions at station 2, it is apparent that the boundary layer at station 2 is much thicker than at station 1.

Transverse wave-type roughness.- The schlieren photographs of the flows over the models with the transverse wave-type surface roughness indicate basically similar characteristics for all configurations within this group (figs. 20 to 22). At the subsonic speeds there is a flow expansion on the roughness surfaces inclined toward the front (left in photographs) and a compression on those surfaces inclined toward the rear. The effect is generally stronger at $M_\infty = 0.90$ than at 0.70, and stronger on the models with the 0.053-inch waves than on the one with 0.017-inch waves. At sonic free-stream Mach number, shocks

appear. These shocks apparently have origins close to the peak heights of the roughness and substantiate the pressure distributions (figs. 7 to 9, part (c)) in indicating that the supersonic-flow expansions do not proceed very far downstream of the roughness peaks at this Mach number. As the free-stream Mach number is increased the shocks increase their inclination and there is evidence of a rearward movement of the origin of the shock. The light areas behind the shocks and close to the model surface indicate (as do the pressures of figs. 7 to 9, parts (c), (d), and (e)) a gradual compression in the trough areas of the surface roughness behind the shocks.

Roughness with sweep.- Schlieren flow photographs of the flow over the model with the 0.020-inch 45° rearward steps and 0.014-inch 45° creases are not presented inasmuch as little if any flow disturbances can be seen owing to the lack of proper orientation of the light of the schlieren system relative to the swept nature of the flow disturbances induced by the roughness elements.

CONCLUDING REMARKS

An investigation has been made in the transonic Mach number range from 0.70 to 1.20 and over a range of free-stream Reynolds number per foot from about 0.8×10^6 to 6.0×10^6 to determine the pressure distributions over essentially two-dimensional fabrication-type surface roughness immersed in a turbulent boundary layer. The results have been examined with the objective of establishing the basic types of flow phenomena over the roughness elements so that proper theoretical and empirical methods of investigating the phenomena of roughness drag in more detail can be delineated.

Examination of the subsonic results in the form of longitudinal pressure distributions did not indicate the process by which roughness drag is generated subsonically, but did show the need for developing theories for predicting pressures for arbitrary roughness shapes at these speeds. Investigation of at least the discrepancies in trends between theoretical and experimental pressure distributions for the various roughness shapes can possibly then indicate the actual physical mechanism.

At transonic and supersonic Mach numbers the pressure distributions indicated the generation and expansion of local supersonic flows over the roughness elements with the onset of supersonic wave drag. Similarities in the effects of Mach number, free-stream Reynolds number per foot, and between longitudinal stations suggested that it may be possible to correlate the surface roughness drags, if not the pressures, in terms of the local boundary-layer profile characteristics and roughness height and shape. At this

14

point probable methods for accounting for the effects of roughness sweepback on the pressure distributions are not readily apparent, although again, it may be possible to derive an empirical method for estimating the drag.

Langley Research Center,
    National Aeronautics and Space Administration,
        Langley Station, Hampton, Va., February 18, 1966.

15

REFERENCES

1. Czarnecki, K. R.; Robinson, Ross B.; and Hilton, John H., Jr.: Investigation of Distributed Surface Roughness on a Body of Revolution at a Mach Number of 1.61. NACA TN 3230, 1954.

2. Sevier, John R., Jr.; and Czarnecki, K. R.: Investigation of Effects of Distributed Surface Roughness on a Turbulent Boundary Layer Over a Body of Revolution at a Mach Number of 2.01. NACA TN 4183, 1958.

3. Czarnecki, K. R.; Sevier, John R., Jr.; and Carmel, Melvin M.: Effects of Fabrication-Type Roughness on Turbulent Skin Friction at Supersonic Speeds. NACA TN 4299, 1958.

4. Czarnecki, K. R.; and Monta, William J.: Pressure Distributions and Wave Drag Due to Two-Dimensional Fabrication-Type Surface Roughness on an Ogive Cylinder at Mach Numbers of 1.61 and 2.01. NASA TN D-835, 1961.

5. Czarnecki, K. R.; and Monta, William J.: Boundary-Layer Velocity Profiles and Skin Friction Due to Surface Roughness on an Ogive Cylinder at Mach Numbers of 1.61 and 2.01. NASA TN D-2048, 1963.

6. Schaefer, William T., Jr.: Characteristics of Major Active Wind Tunnels at the Langley Research Center. NASA TM X-1130, 1965.

7. Mugler, John P., Jr.: Transonic Wind-Tunnel Investigation of the Aerodynamic Loading Characteristics of a 60° Delta Wing in the Presence of a Body With and Without Indentation. NACA RM L55G11, 1955.

8. Tucker, Maurice: Approximate Calculation of Turbulent Boundary-Layer Development in Compressible Flow. NACA TN 2337, 1951.

9. Reissner, Eric: On Compressibility Corrections for Subsonic Flow Over Bodies of Revolution. NACA TN 1815, 1949.

10. General Theory of High Speed Aerodynamics: Princeton Series: High Speed Aerodynamics and Jet Propulsion, Volume VI.

11. Woolard, Henry W.: Theoretical Analysis of the Flow and Drag of Surface Irregularities Immersed in a Wall-Layer Stream in a Supersonic Main Stream. TG-425 (Contract NOrd 7486), Appl. Phys. Lab., The Johns Hopkins Univ., Oct. 1961.

TABLE I.- MODEL DESIGNATIONS

Model	Designations	Number of cycles of roughness
1	85 microinches	---------
2	0.021-inch steps with grooves	9
3	0.053-inch protruding waves	24
4	0.053-inch transverse creases	24
5	0.017-inch transverse creases	24
6	0.020-inch 45° rearward steps	5 stripes
7	0.014-inch 45° creases	6 stripes

TABLE II.- MODEL ORIFICE LOCATIONS

Orifice	x, in., for model 1
1	1.01
2	1.95
3	2.82
4	3.81
5	4.78
6	5.78
7	6.76
8	7.76
9	8.77
10	9.79
11	10.78
12	11.80
13	12.78
14	13.77
15	14.78
16	15.78
17	16.78
18	17.75
19	18.79
20	19.78
21	20.78
22	22.75
23	24.74
24	26.77
25	28.76
26	30.77
27	32.76
28	34.78
29	36.79
30	42.14
31	44.10
32	46.08
33	48.08
34	49.62

Orifice	x, in., for model 2
Station 1	
1	14.11
2	14.19
3	14.21
4	14.50
5	14.78
6	15.04
7	15.30
8	15.57
9	15.82
10	16.10
11	16.18
12	16.26
13	16.53
14	16.76
15	17.04
16	17.30
17	17.56
18	17.84
19	18.11
20	18.19
Station 2	
21	44.08
22	44.15
23	44.26
24	44.52
25	44.78
26	45.04
27	45.30
28	45.58
29	45.85
30	46.10
31	47.21
32	46.25
33	46.49
34	46.77
35	47.03
36	47.31
37	47.57
38	47.85
39	48.08
40	48.16

Orifice	x, in., for model —			
	3	4	5	7
Station 1				
1	15.64	15.03	14.99	18.24
2	15.87	15.27	15.24	18.47
3	16.11	15.52	15.49	18.73
4	16.27	15.67	15.61	18.86
5	16.38	15.78	15.71	18.98
6	16.48	15.86	15.82	19.07
7	16.55	15.96	15.90	19.15
8	16.63	16.03	15.99	19.21
9	16.72	16.11	16.07	19.31
10	16.79	16.21	16.14	19.39
11	16.87	16.29	16.23	19.48
12	16.99	16.42	16.36	19.60
13	17.13	16.52	16.48	19.71
14	17.38	16.78	16.74	19.99
15	17.62	17.04	16.98	20.22
Station 2				
16	45.66	46.55	46.55	44.01
17	45.91	46.78	46.79	44.23
18	46.15	47.02	47.03	44.50
19	46.29	47.14	47.17	44.62
20	46.40	47.28	47.30	44.75
21	46.49	47.37	47.38	44.84
22	46.56	47.44	47.46	44.92
23	46.65	47.52	47.54	45.01
24	46.73	47.60	47.63	45.09
25	46.80	47.67	47.72	45.17
26	46.88	47.78	47.81	45.26
27	47.01	47.91	47.93	45.39
28	47.14	48.04	48.05	45.51
29	47.41	48.28	48.29	45.75
30	47.63	48.54	48.54	46.01

Orifice	x, in., for model 6
Station 1	
1	15.65
2	15.81
3	15.95
4	16.12
5	16.25
6	16.60
7	16.90
8	17.20
9	17.55
10	17.84
11	18.06
12	18.22
Station 2	
13	44.07
14	44.23
15	44.40
16	44.54
17	44.71
18	45.03
19	45.38
20	45.68
21	45.98
22	46.36
23	46.48
24	46.66

Figure 1.- Sketch of basic model. All dimensions are in inches unless otherwise stated.
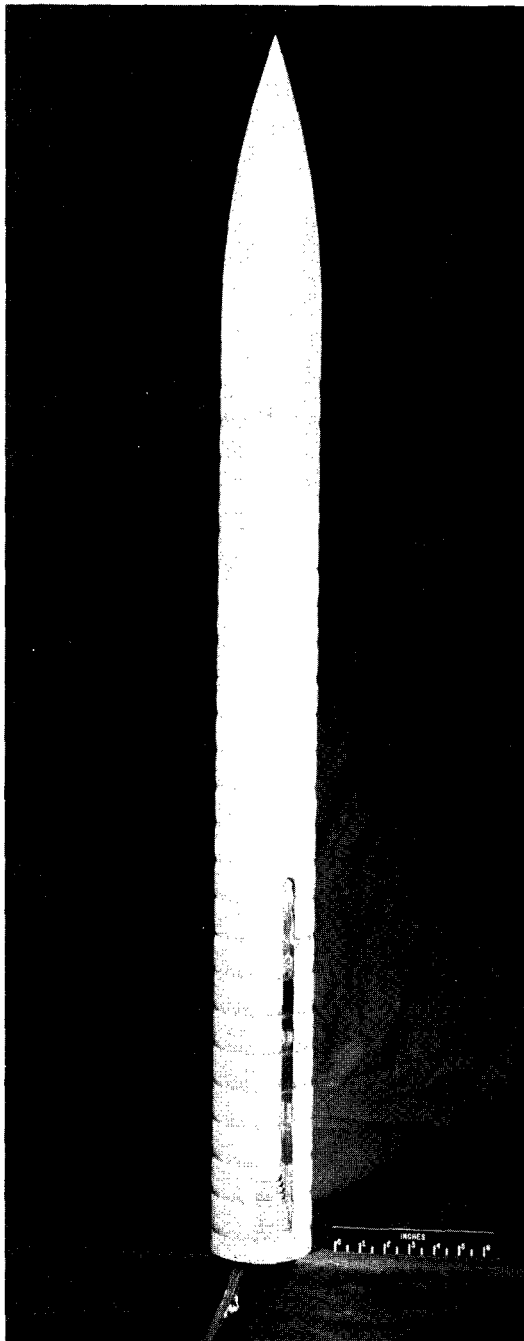
(a) 0.053-inch transverse creases.
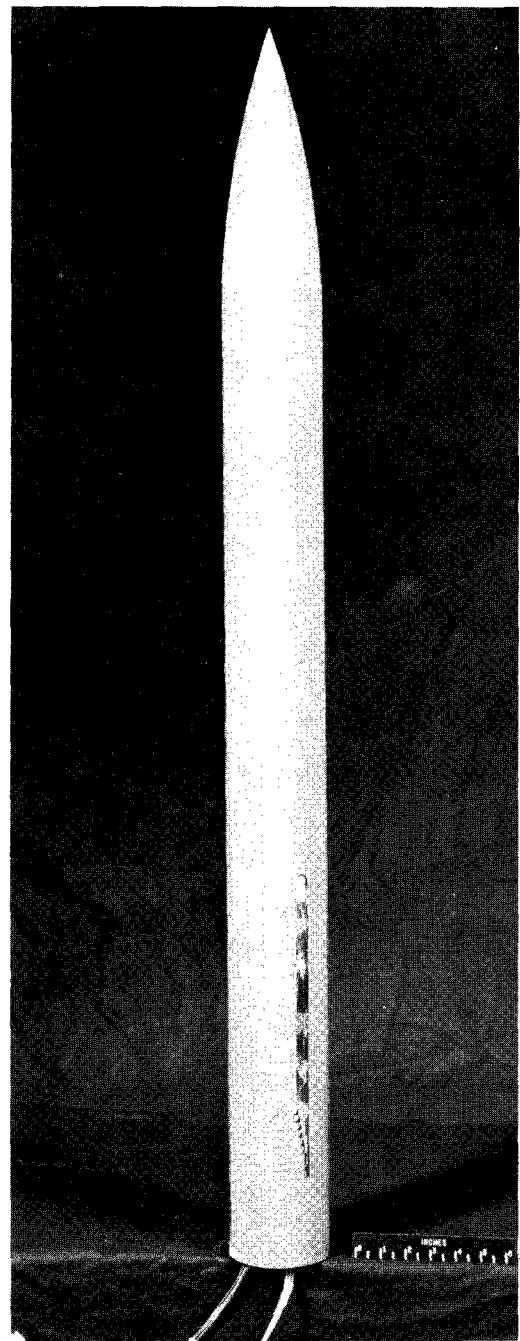
(b) 0.020-inch 45° rearward steps.

Figure 2.- Photographs of typical roughness models.   L-61-1039
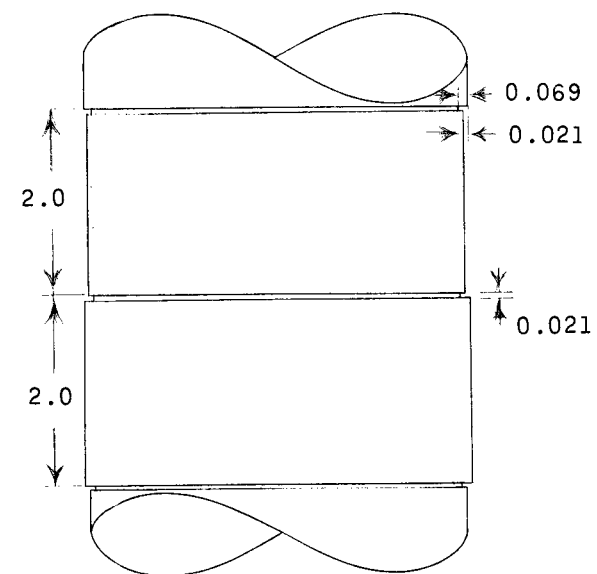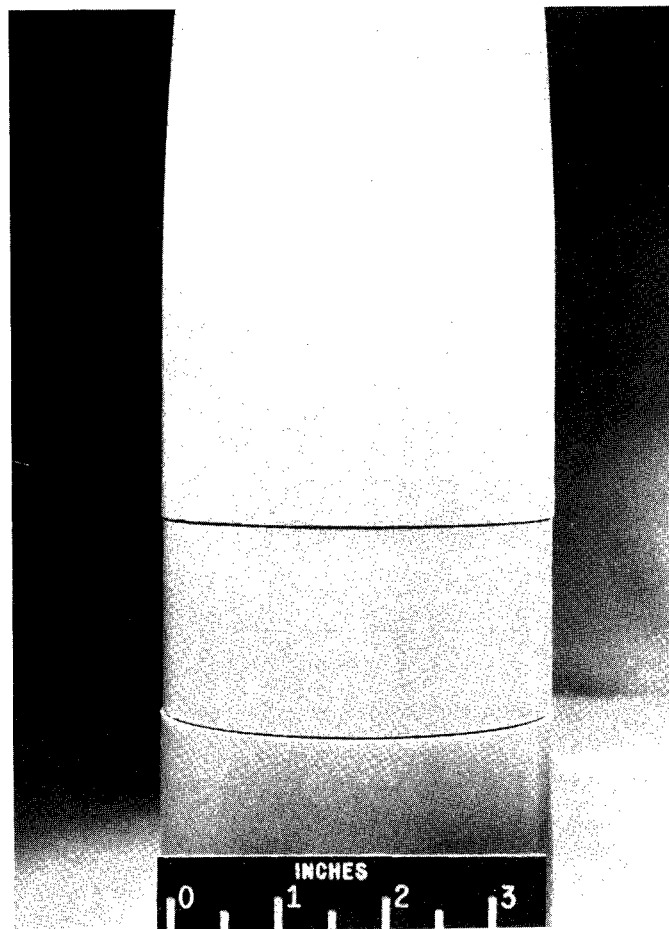
(a) 0.021-inch steps with grooves.   L-61-1040

Figure 3.- Details of fabrication-type roughness. All dimensions are in inches unless otherwise stated.
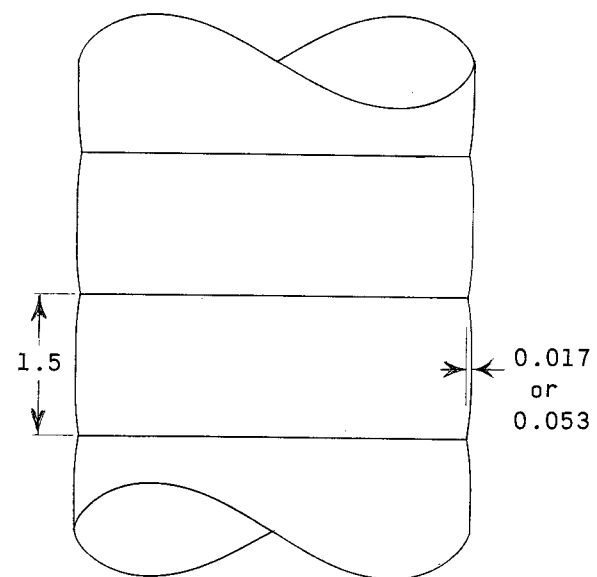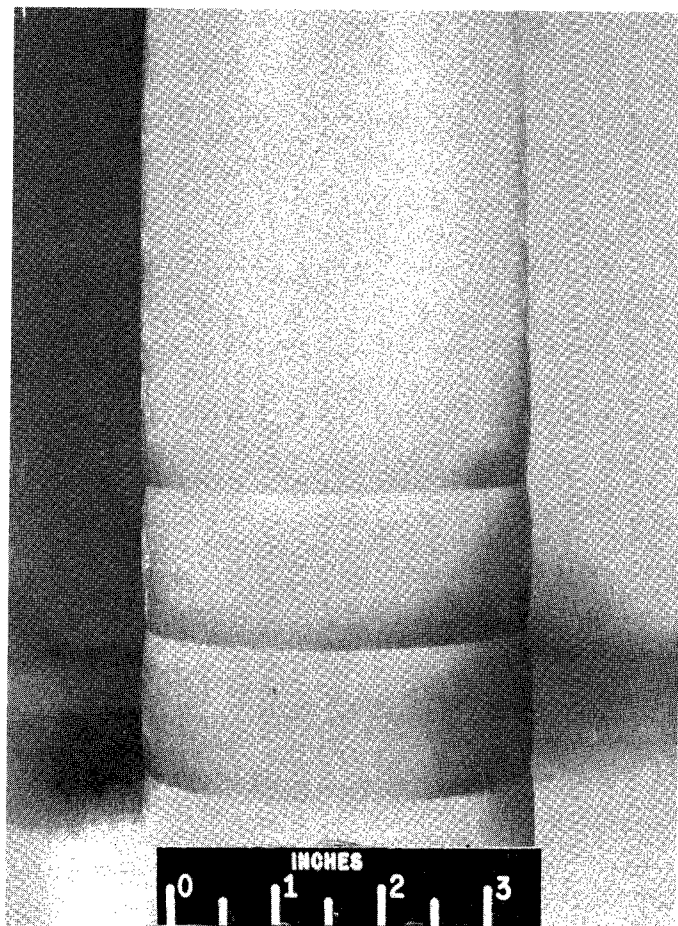
(b) 0.017-inch and 0.053-inch transverse creases.   L-61-1044

Figure 3.- Continued.
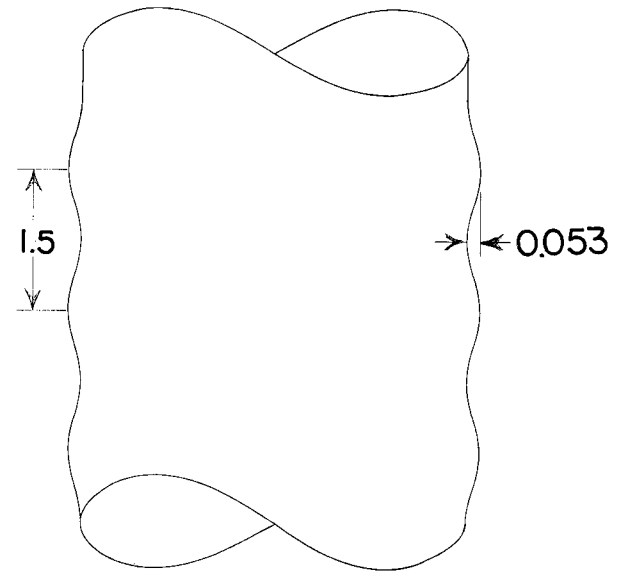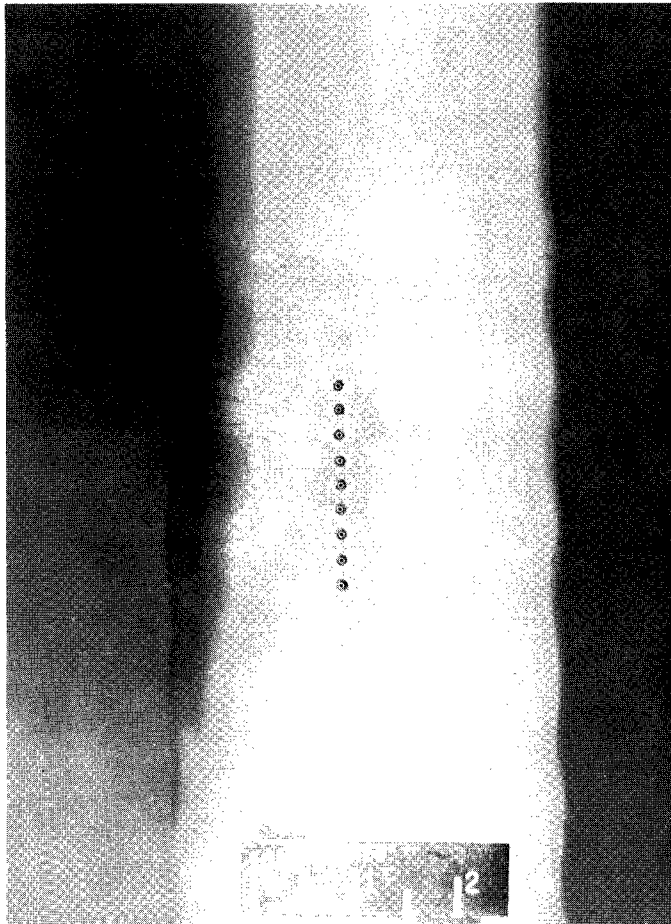
(c) 0.053-inch protruding waves.   L-61-1043

Figure 3.- Continued.
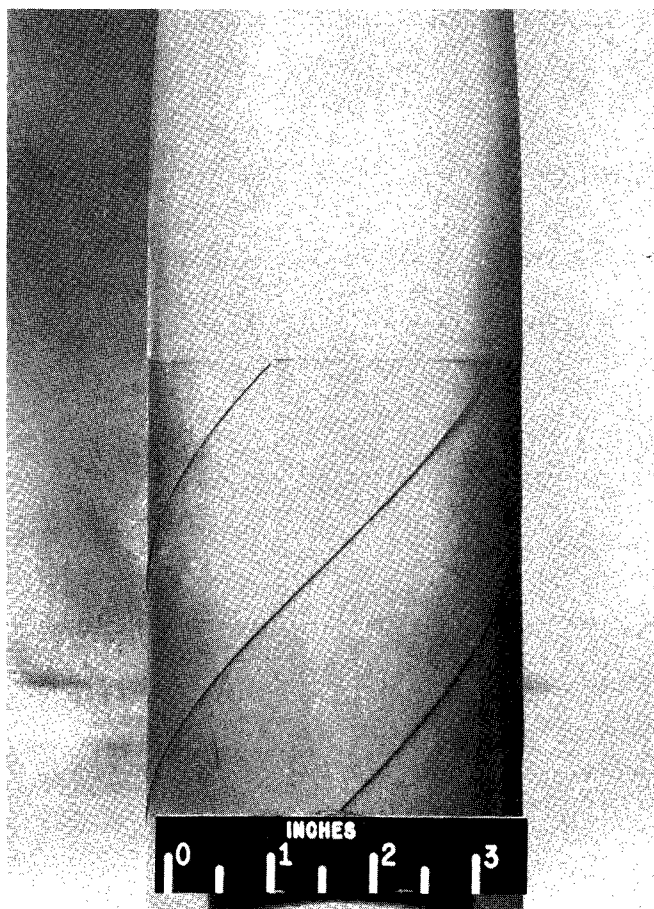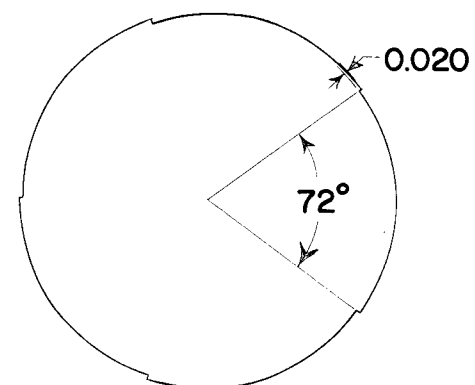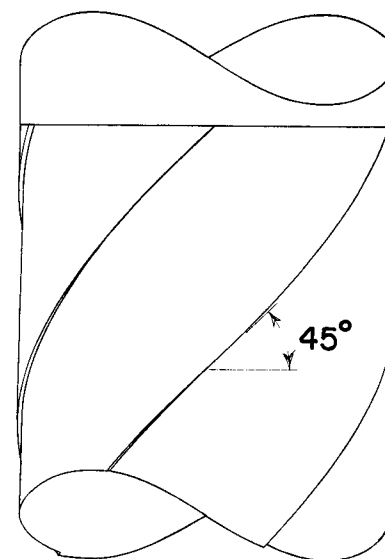
(d) 0.020-inch 45° rearward steps.   L-61-1045

Figure 3.- Continued.
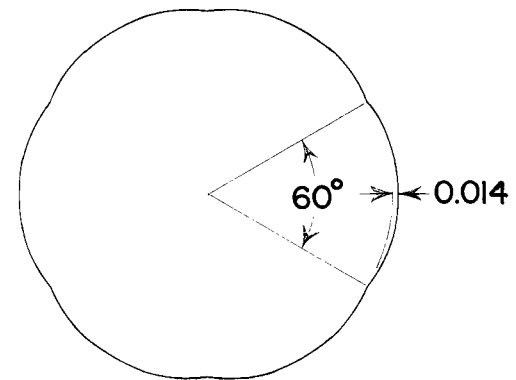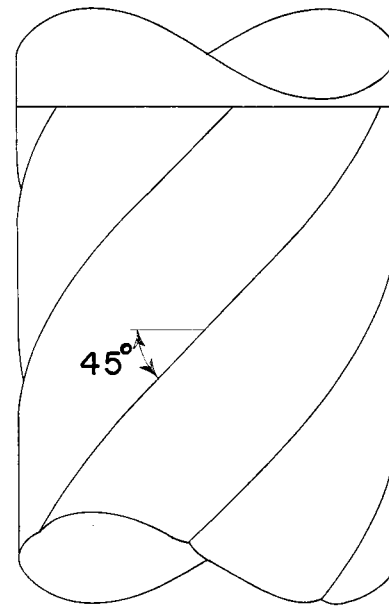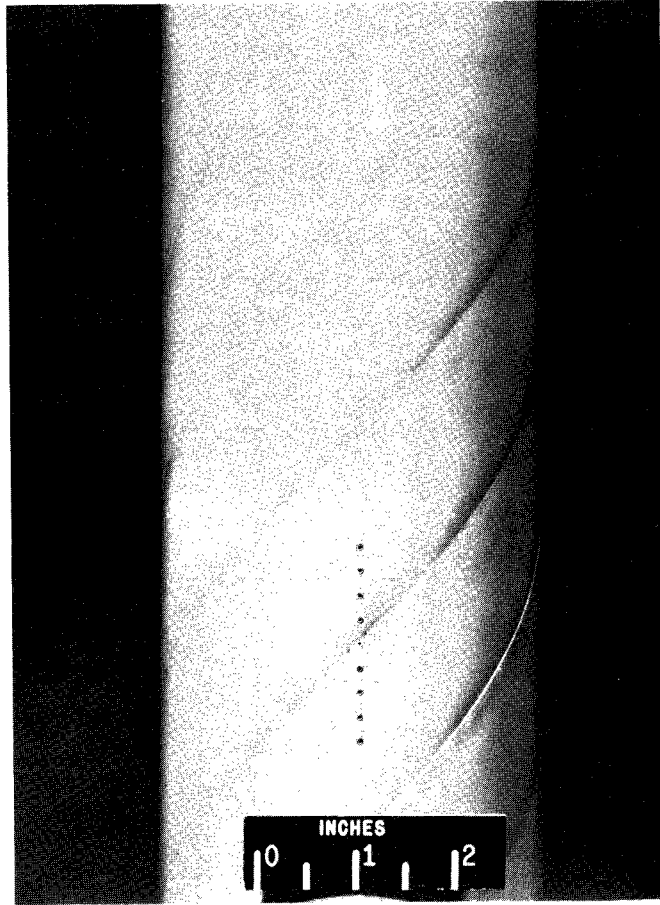
(e) 0.014-inch 45° creases.

Figure 3.- Concluded.

L-61-1046
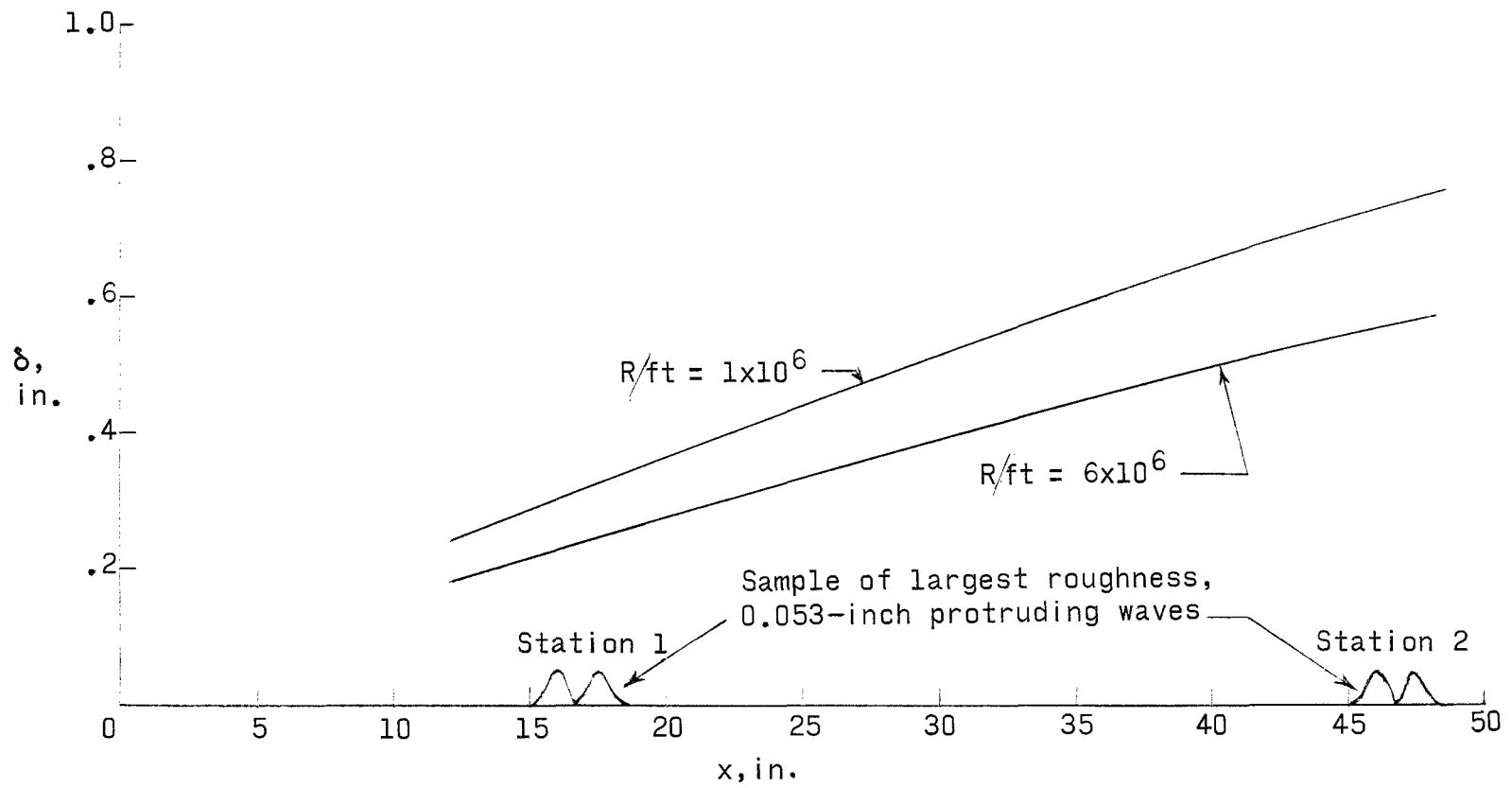
Figure 4.- Comparison of estimated total boundary-layer thickness δ for configuration with highest roughness, 0.053-inch protruding waves. $M_\infty = 1.00$.

Figure 5.- Pressure distributions over basic smooth model.
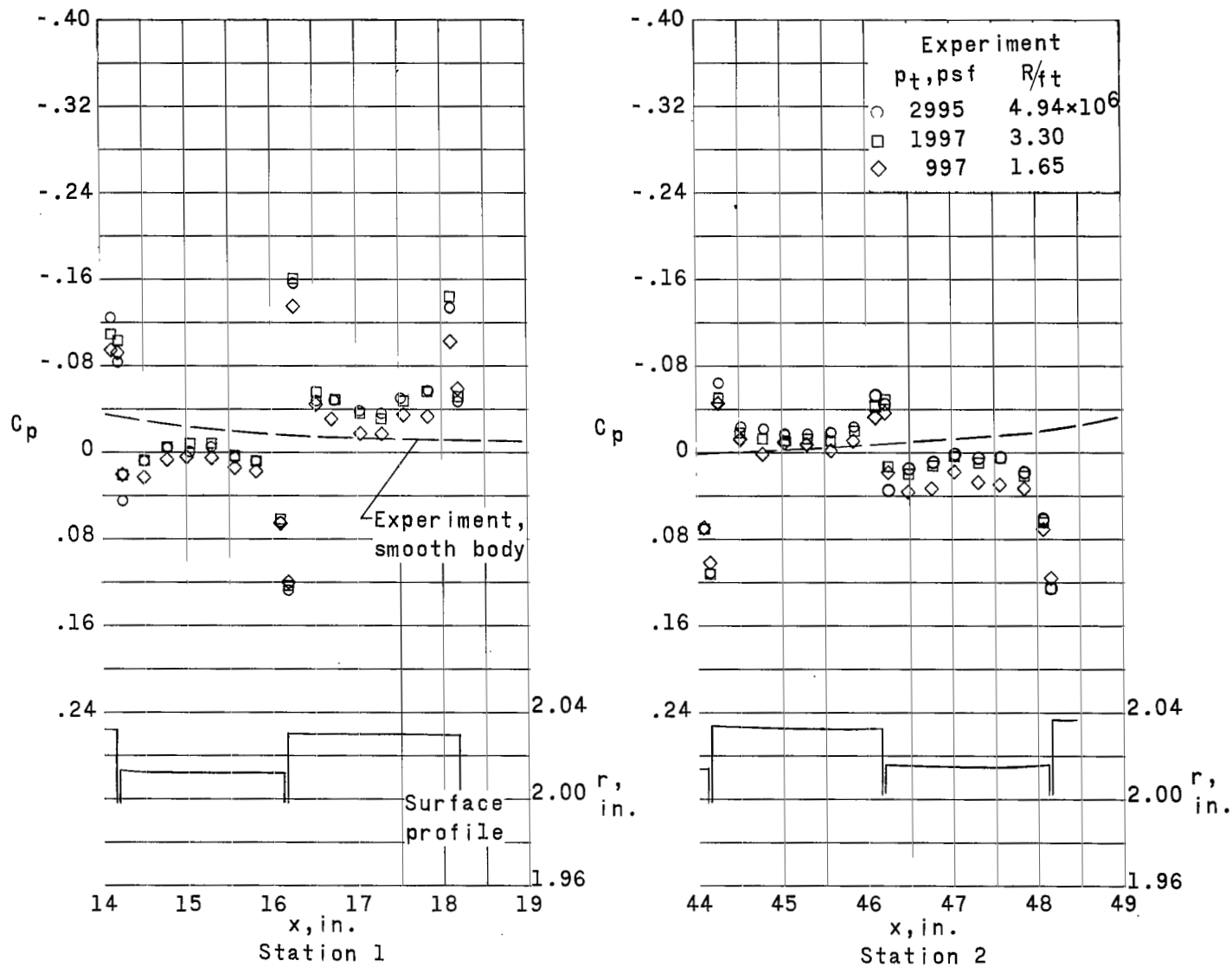
(a) $M_\infty = 0.70$.

Figure 6.- Pressure distributions over model with 0.021-inch steps with grooves at constant M_∞.
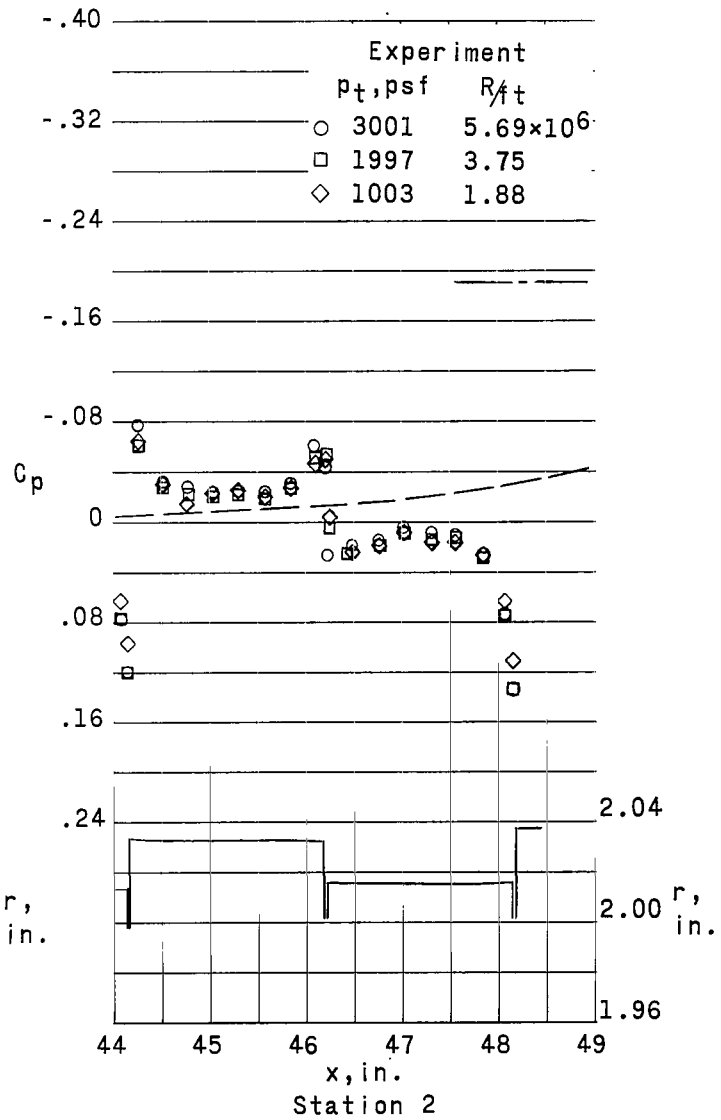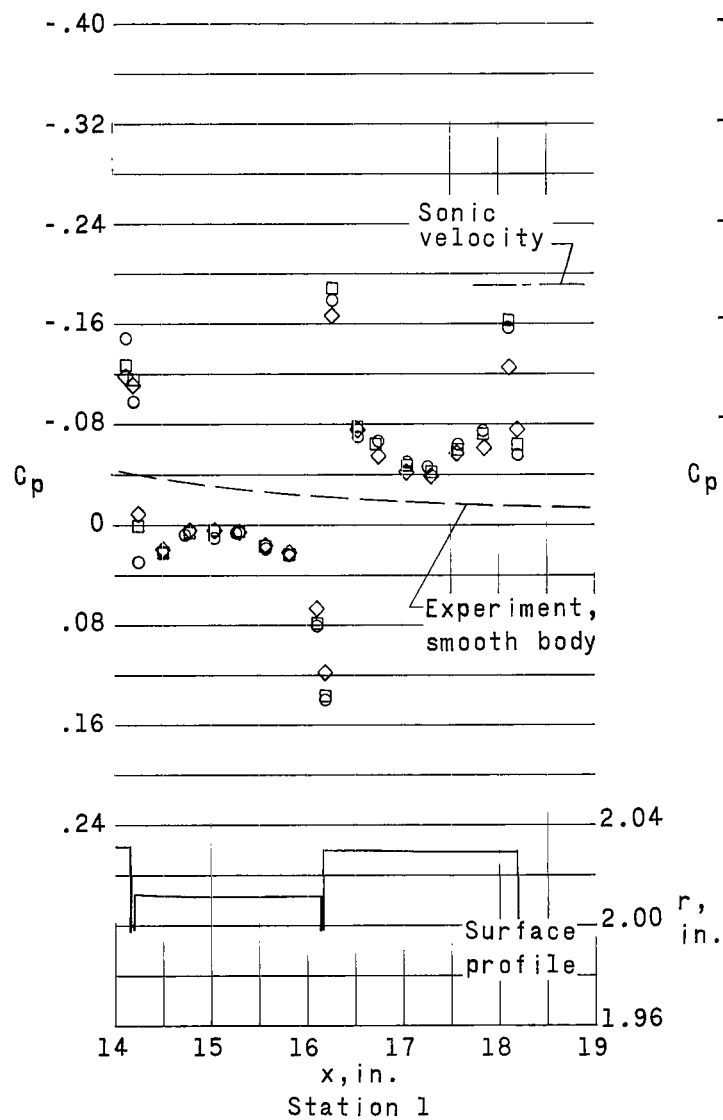
(b) $M_\infty = 0.90$.

Figure 6.- Continued.

(c) $M_\infty = 1.00$.

Figure 6.- Continued.

Supersonic
theory

C_p

Experiment,
smooth body

Sonic
velocity

Surface
profile

Experiment
p_t,psf R/ft
○   3000 5.95×10^6
□   2002   3.97
◇   1001   1.98

C_p

-.40
-.32
-.24
-.16
-.08
0
.08
.16
.24

2.04
2.00 r,
      in.
1.96

14   15   16   17   18   19
x,in.
Station 1

44   45   46   47   48   49
x,in.
Station 2
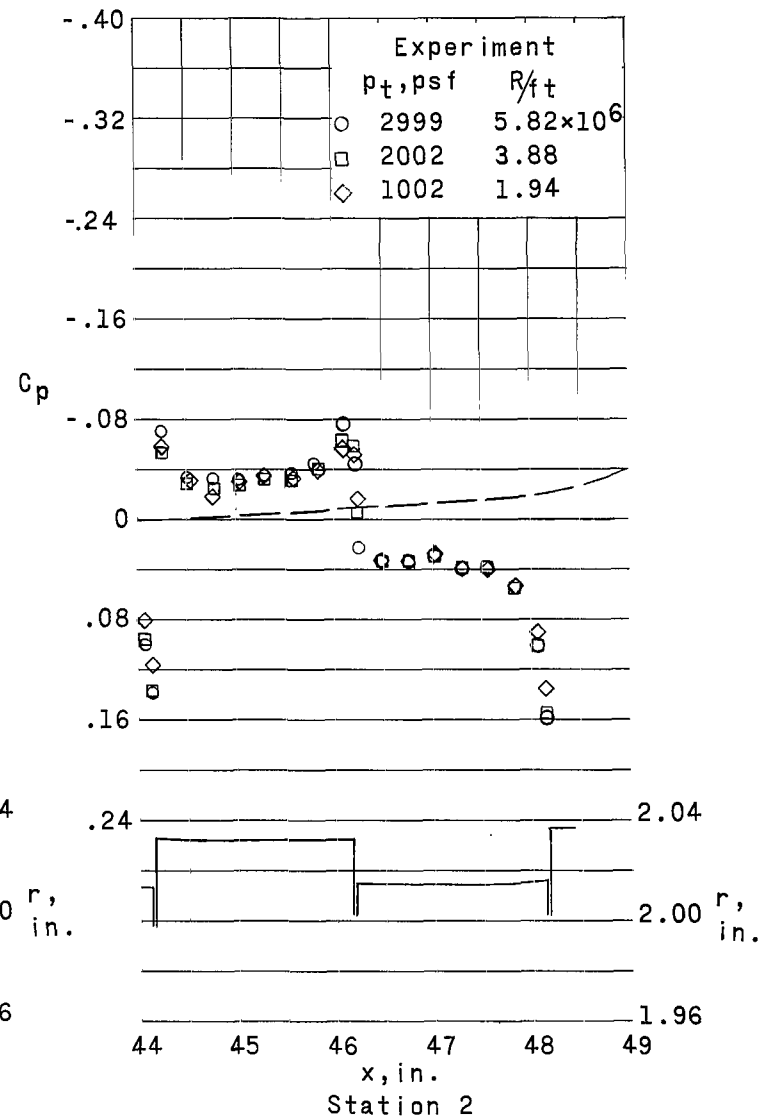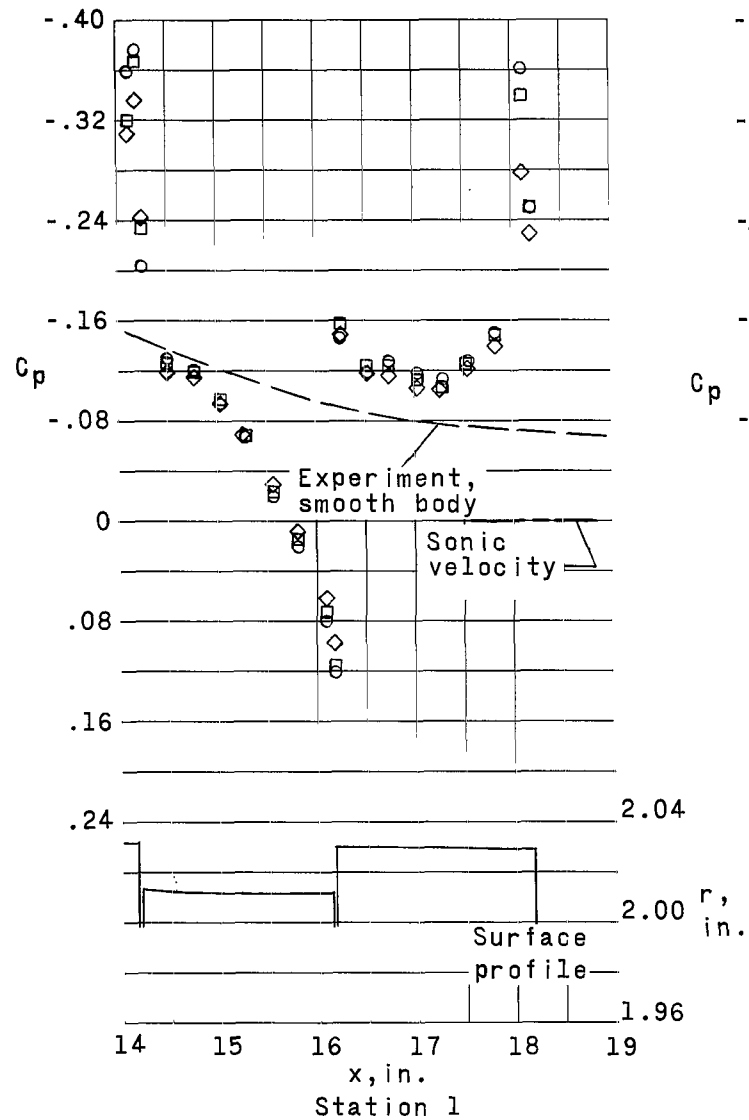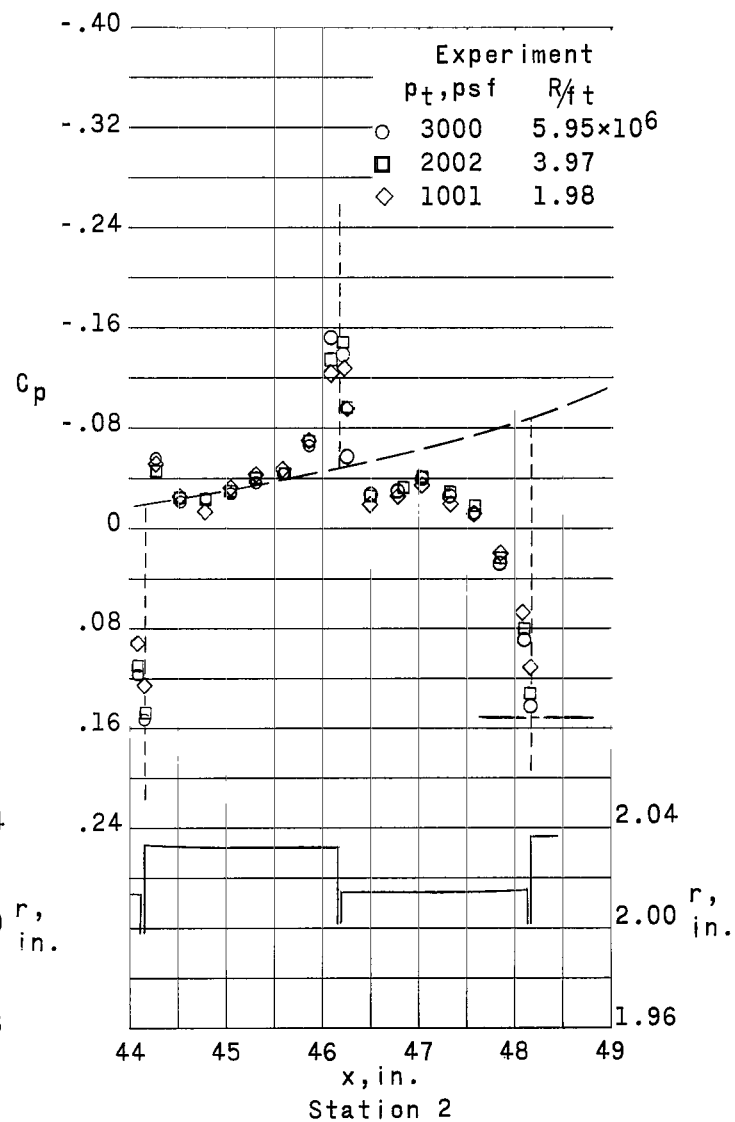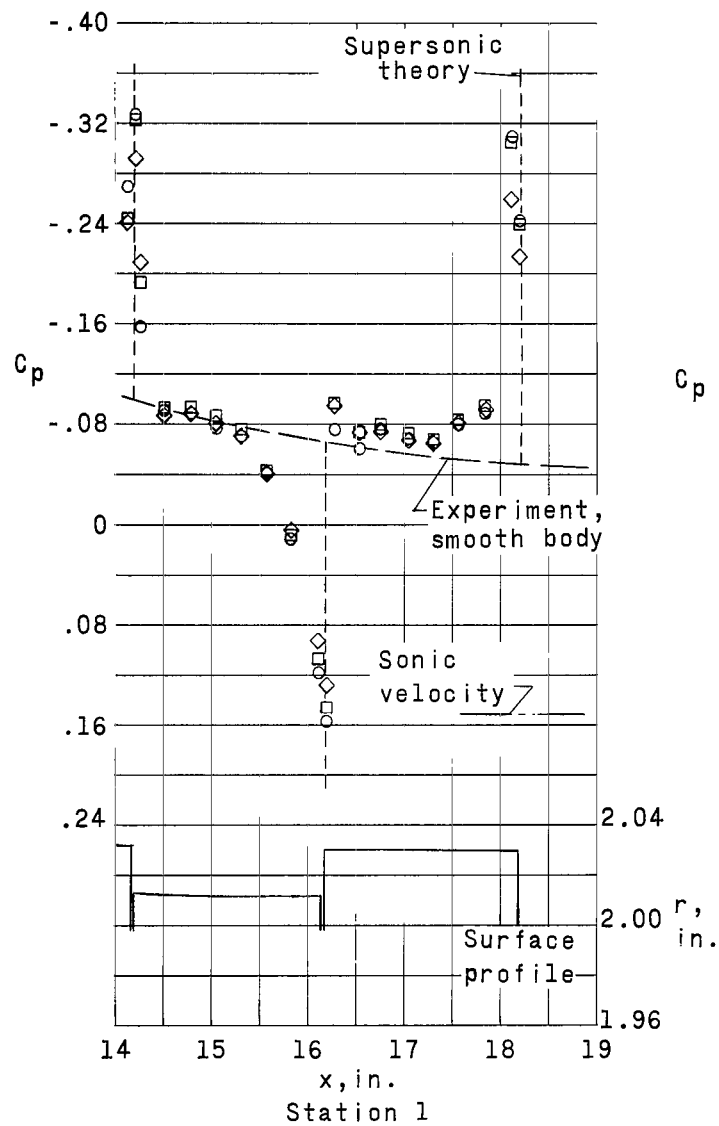
(d) $M_\infty = 1.10$.
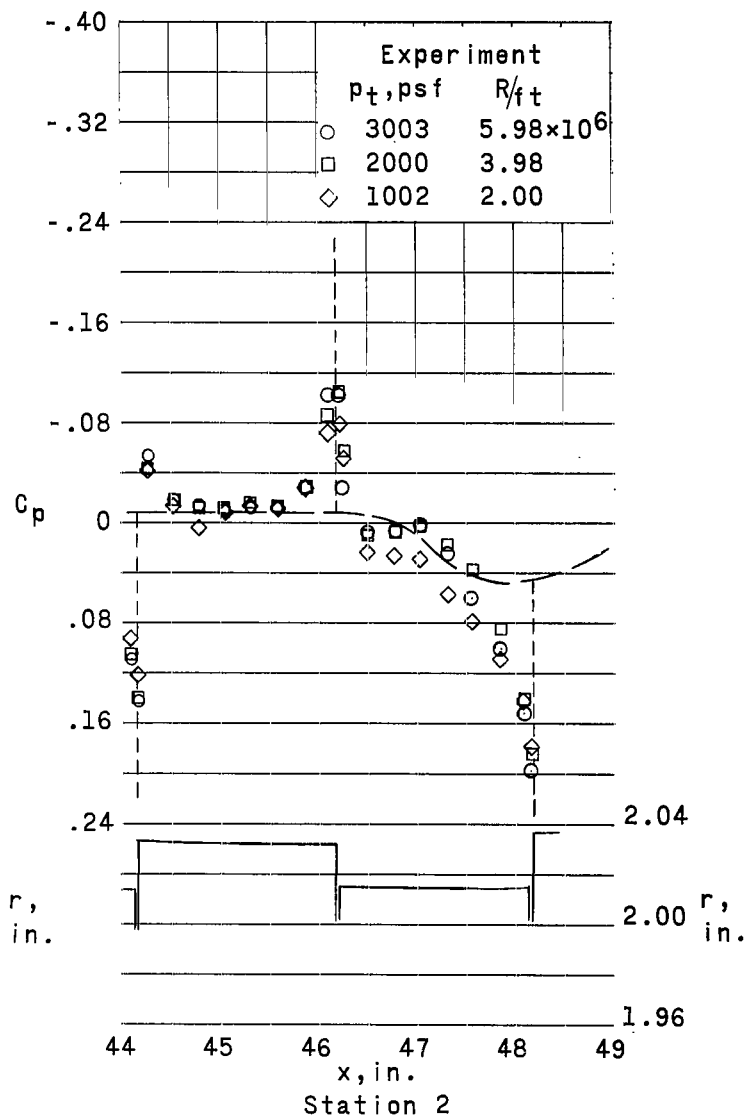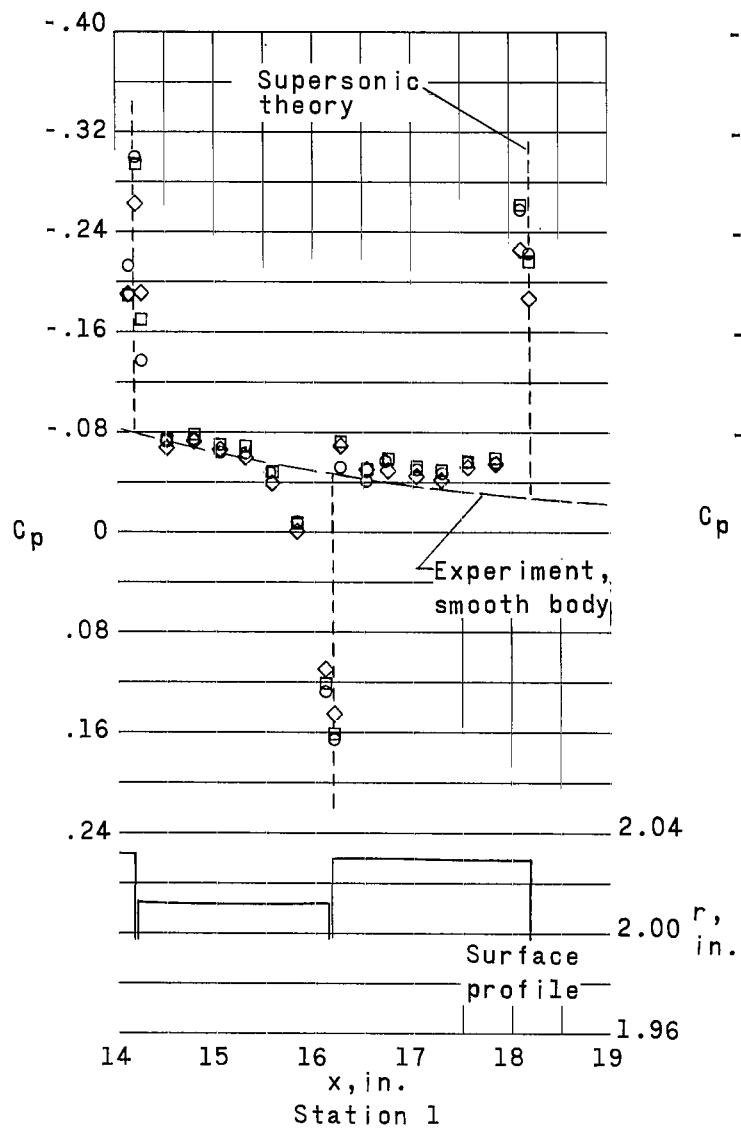
Figure 6.- Continued.

(e) $M_\infty = 1.20$.

Figure 6.- Concluded.
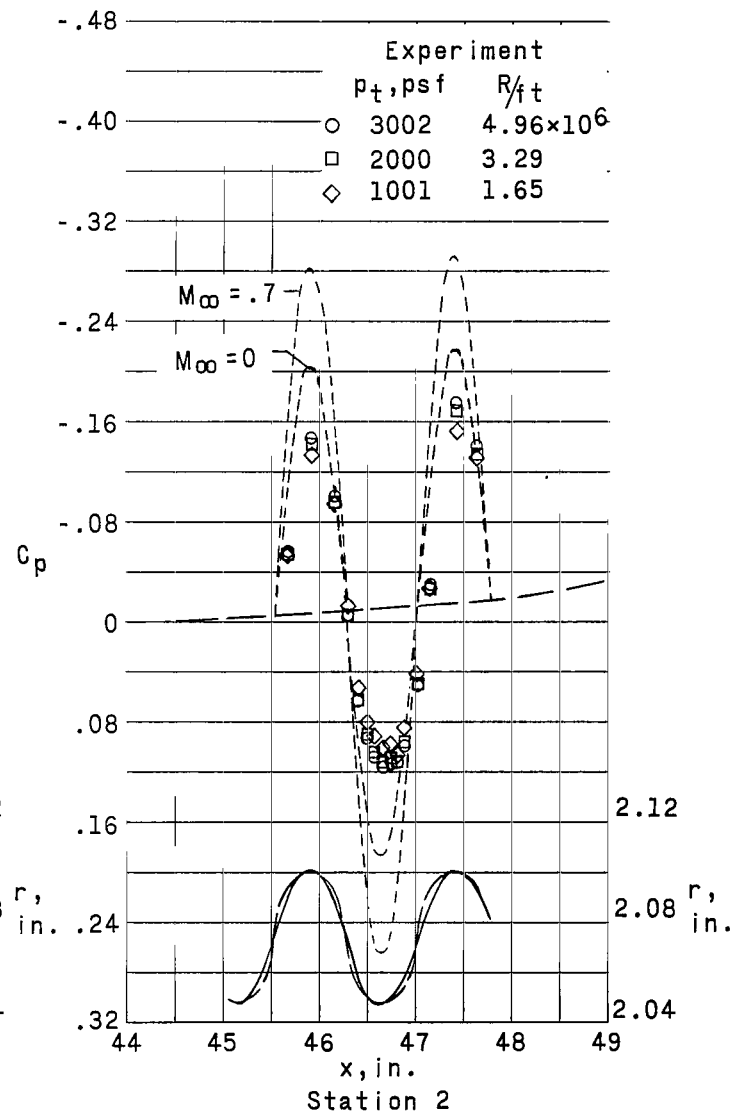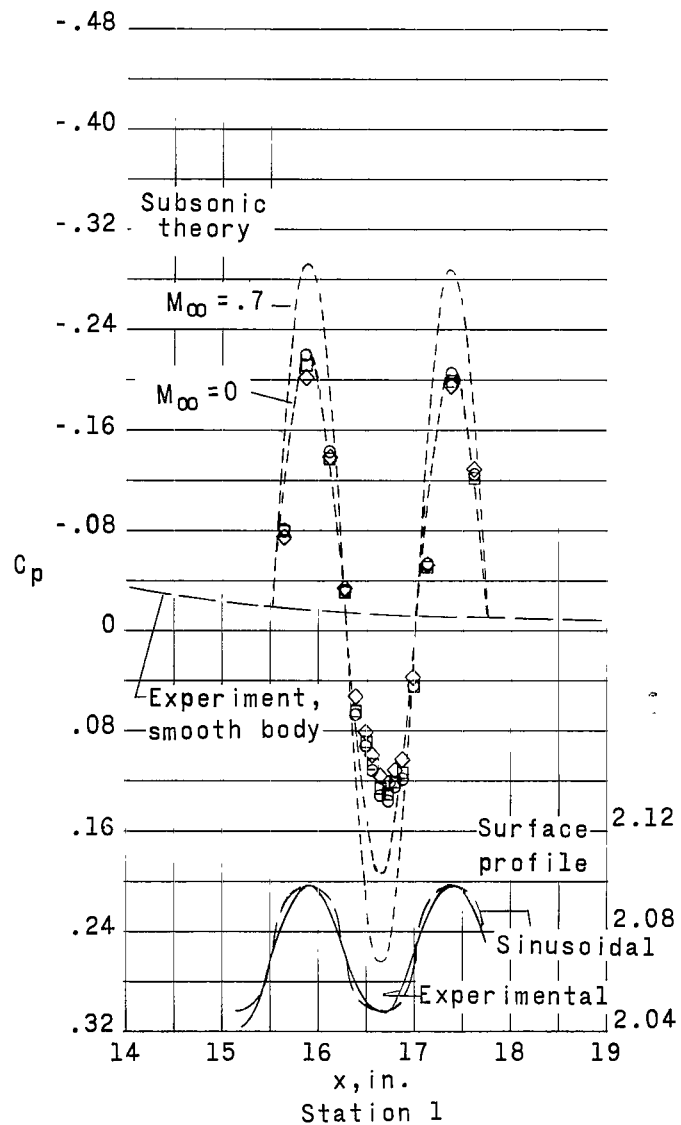
(a) $M_\infty = 0.70$.

Figure 7.- Pressure distributions over model with 0.053-inch protruding waves at constant M_∞.
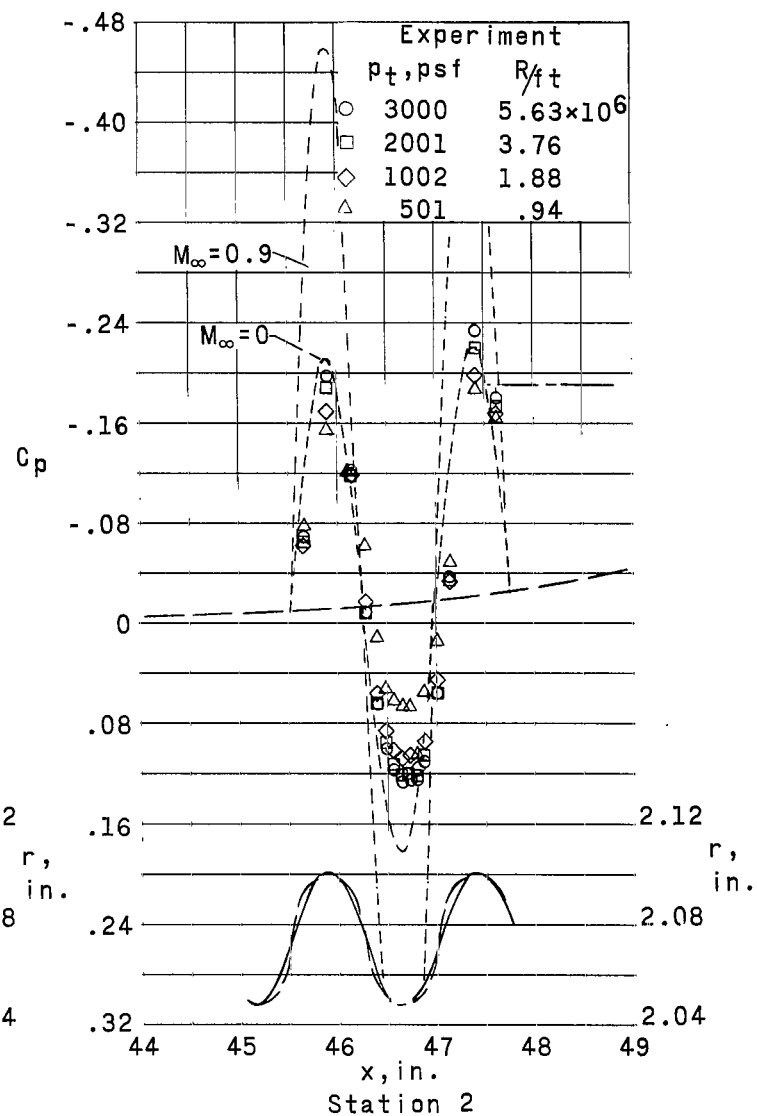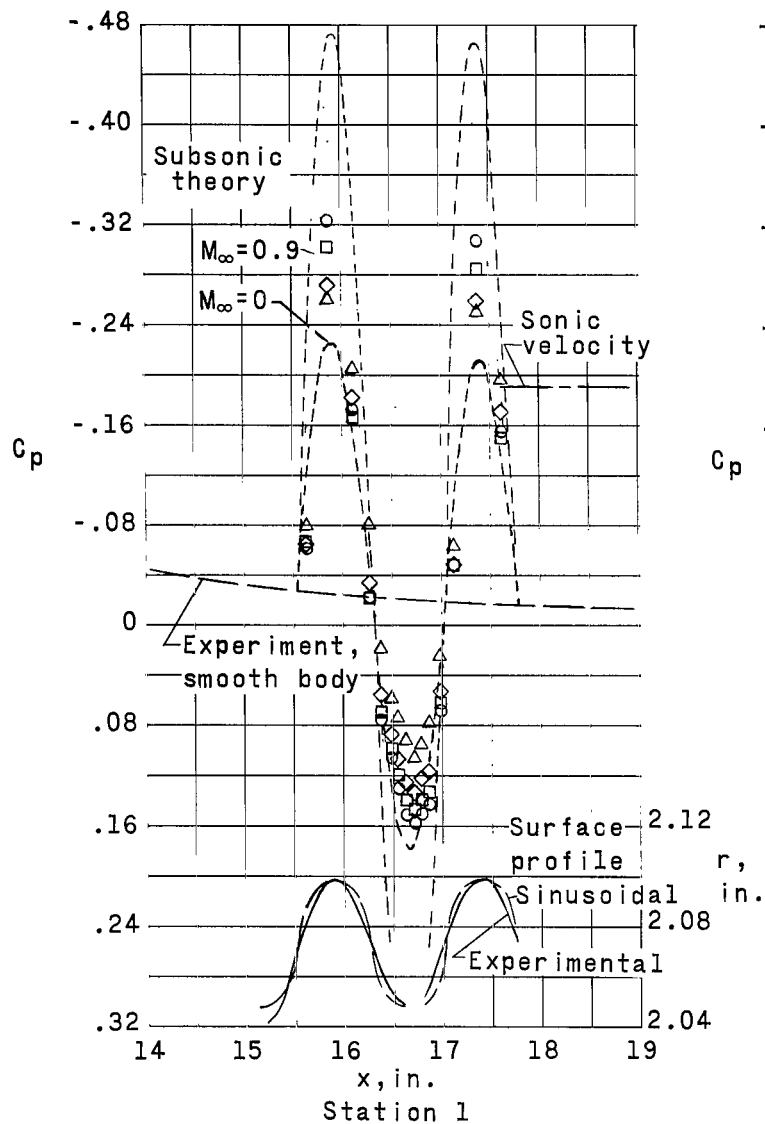
(b) $M_\infty = 0.90.$

Figure 7.- Continued.
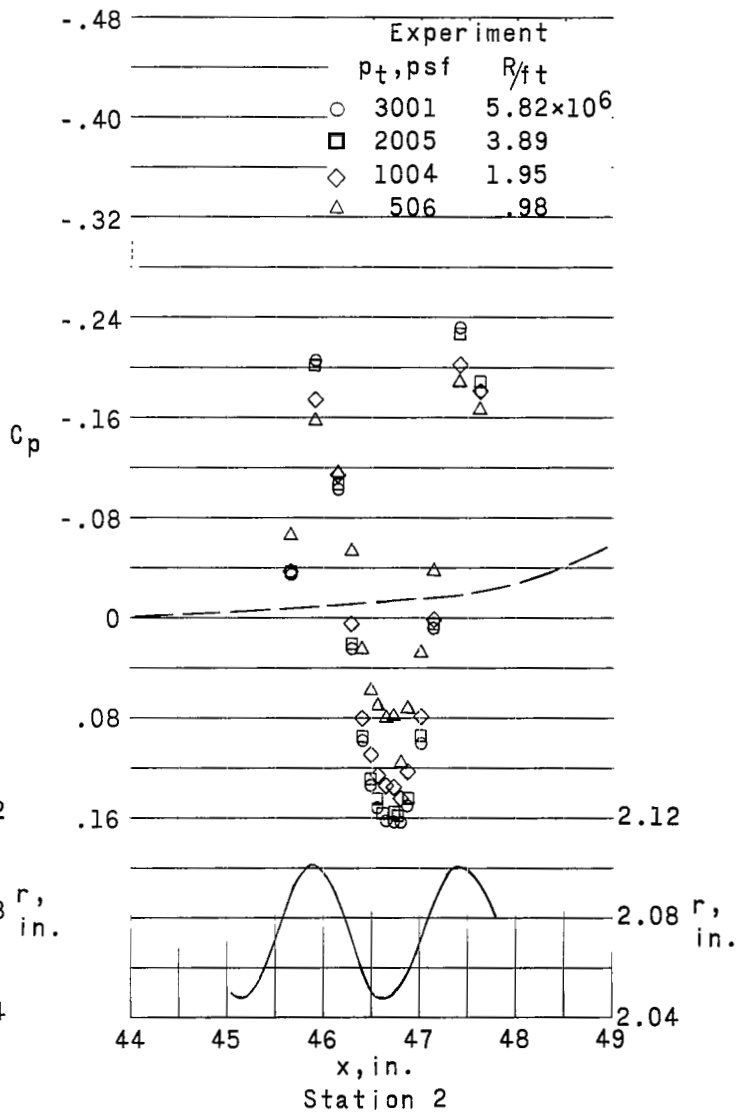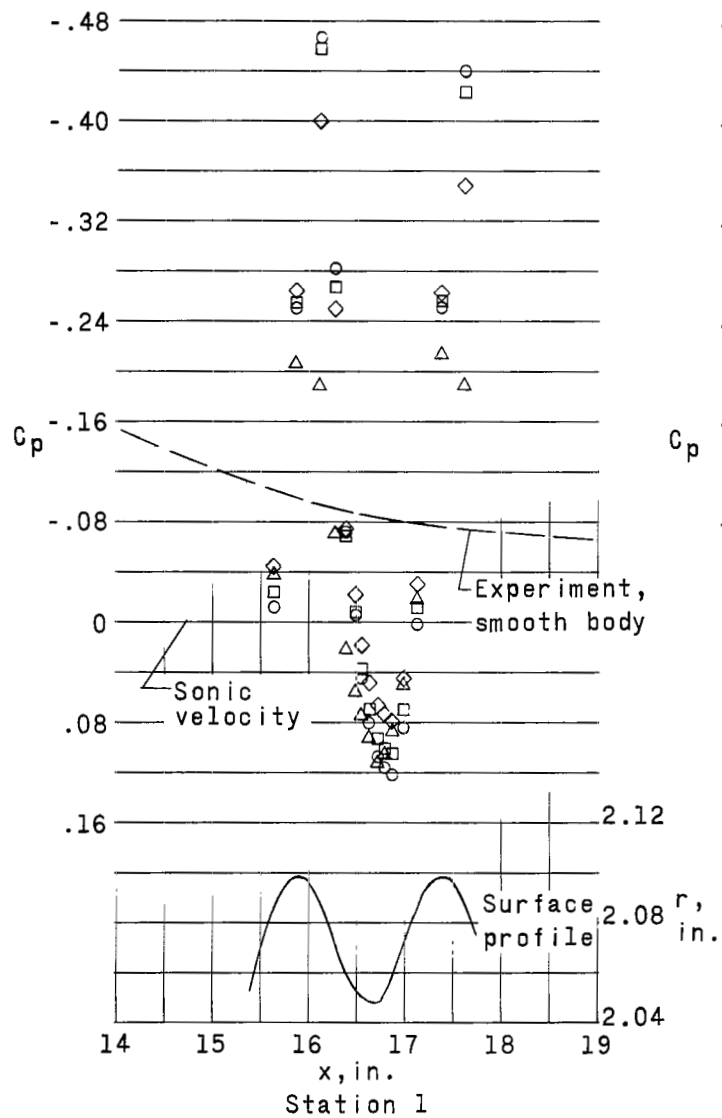
(c) $M_\infty = 1.00$.

Figure 7.- Continued.
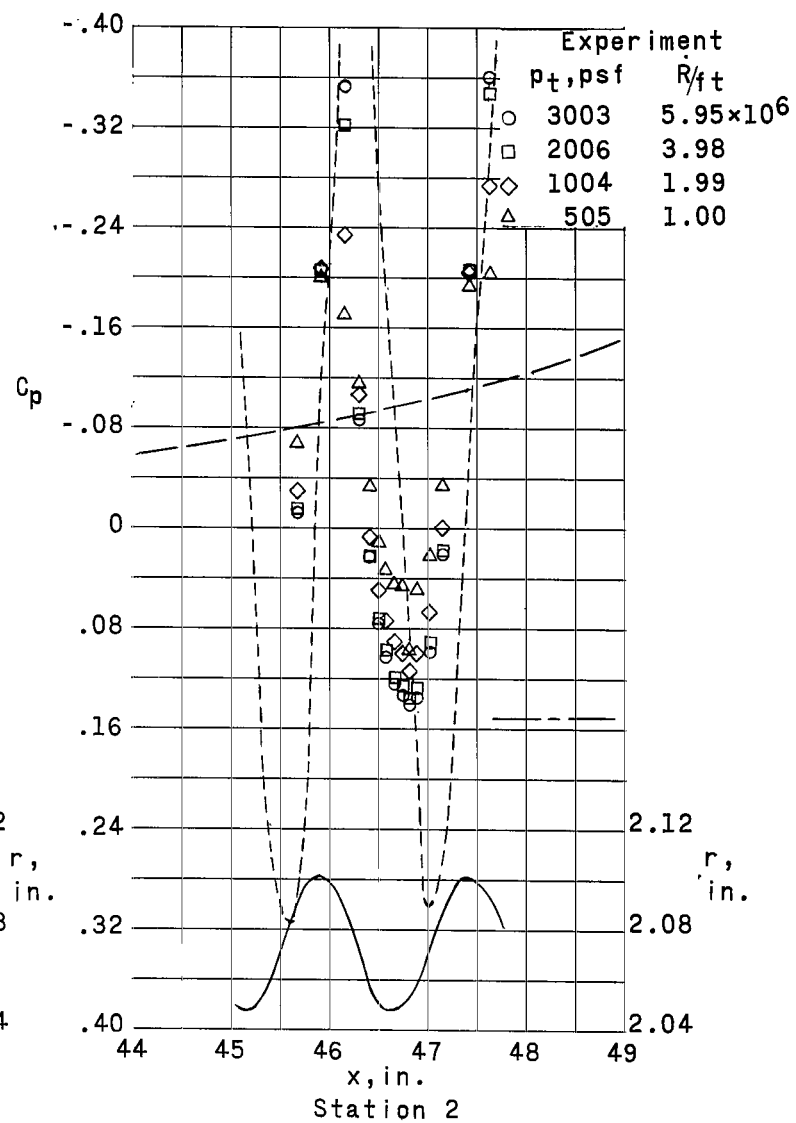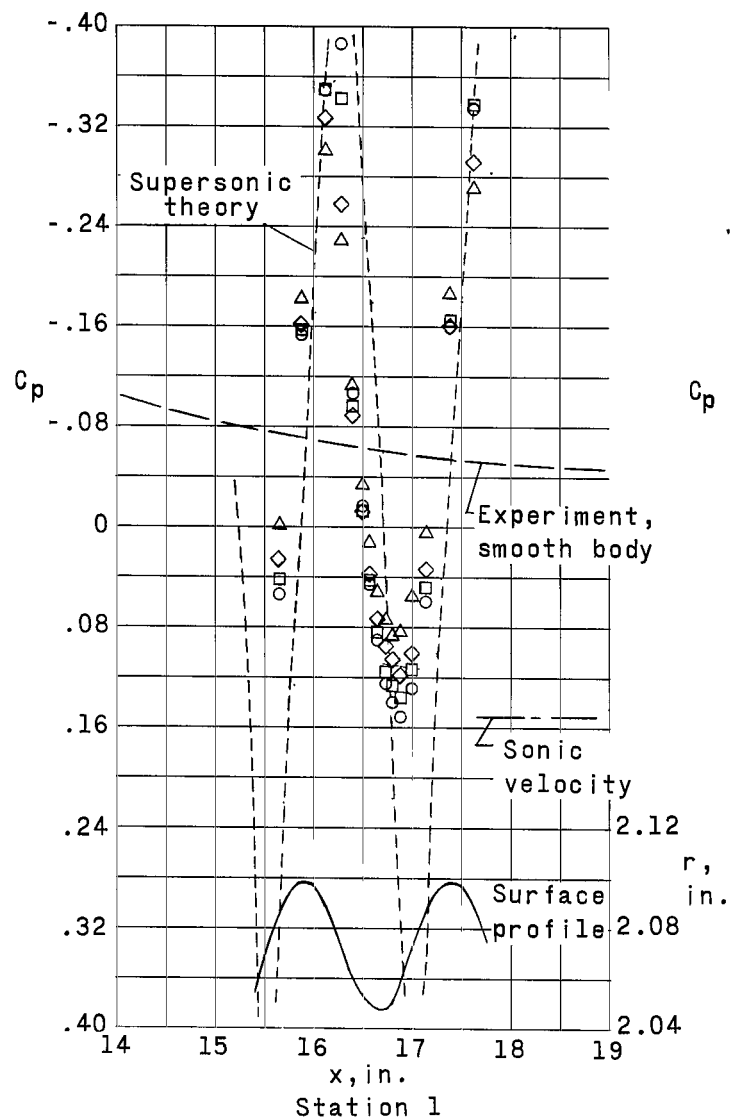
(d) $M_\infty = 1.10$.

Figure 7.- Continued.
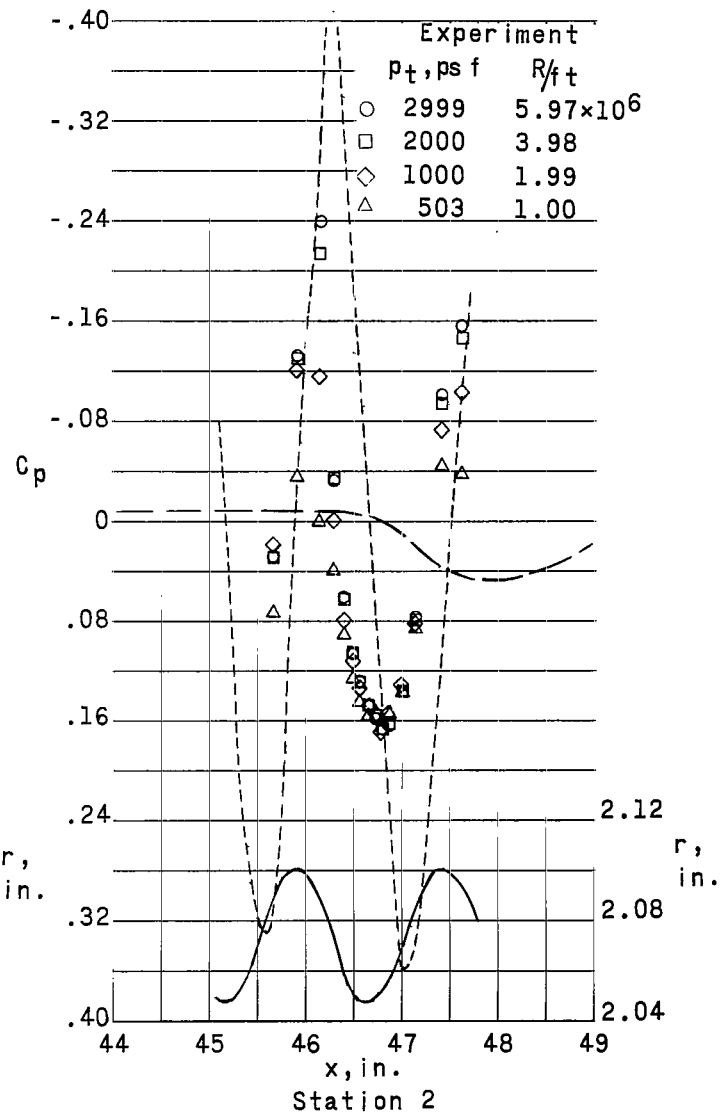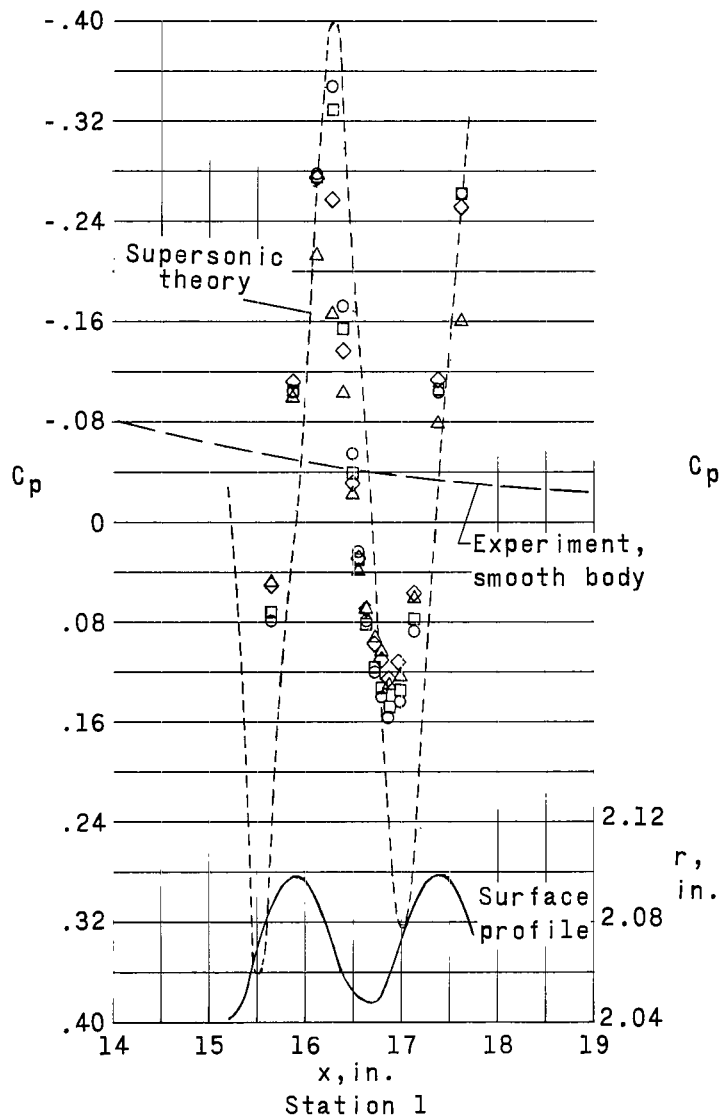
(e) $M_\infty = 1.20$.

Figure 7.- Concluded.
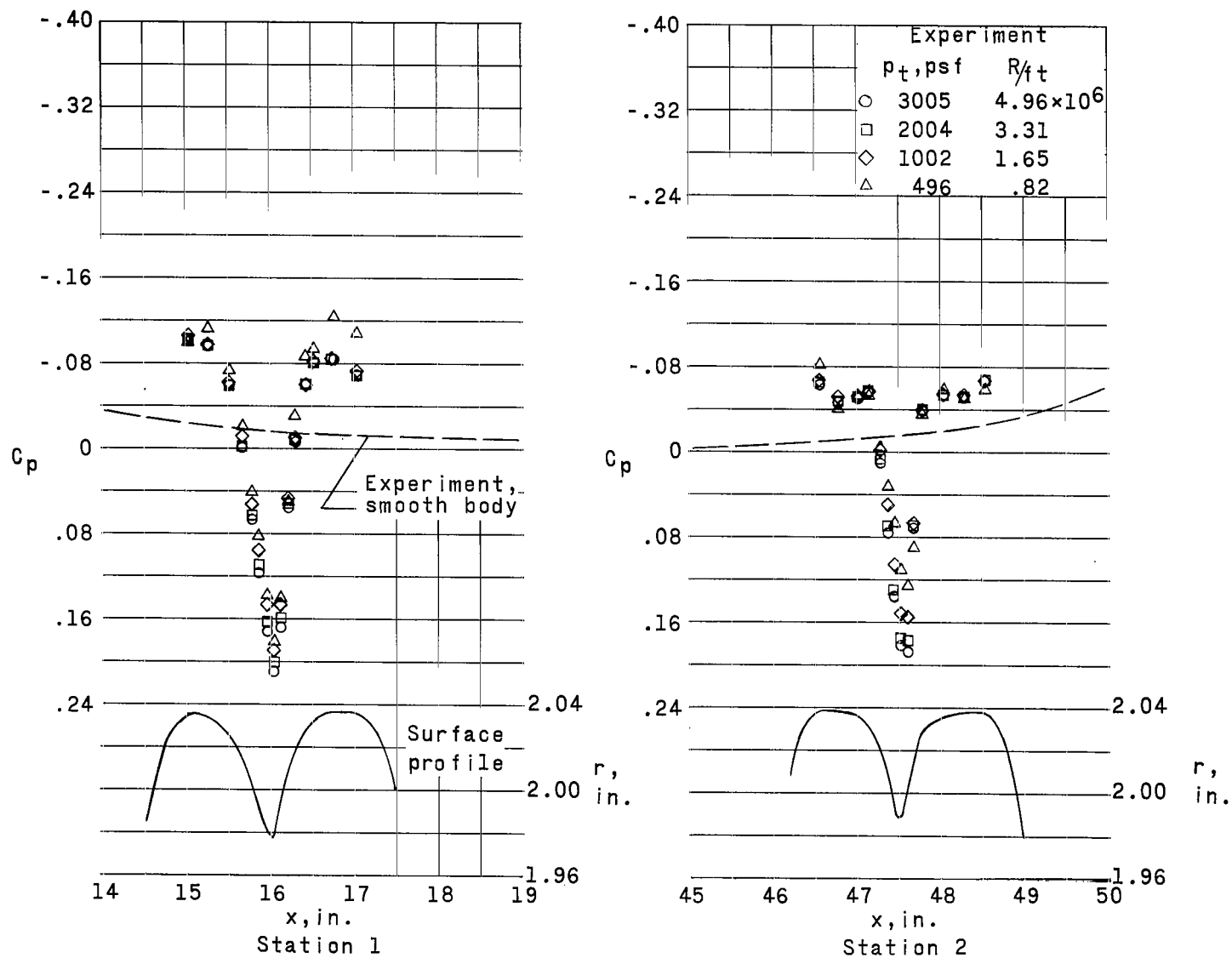
(a) $M_\infty = 0.70$.

Figure 8.- Pressure distributions over model with 0.053-inch transverse creases at constant M_∞.
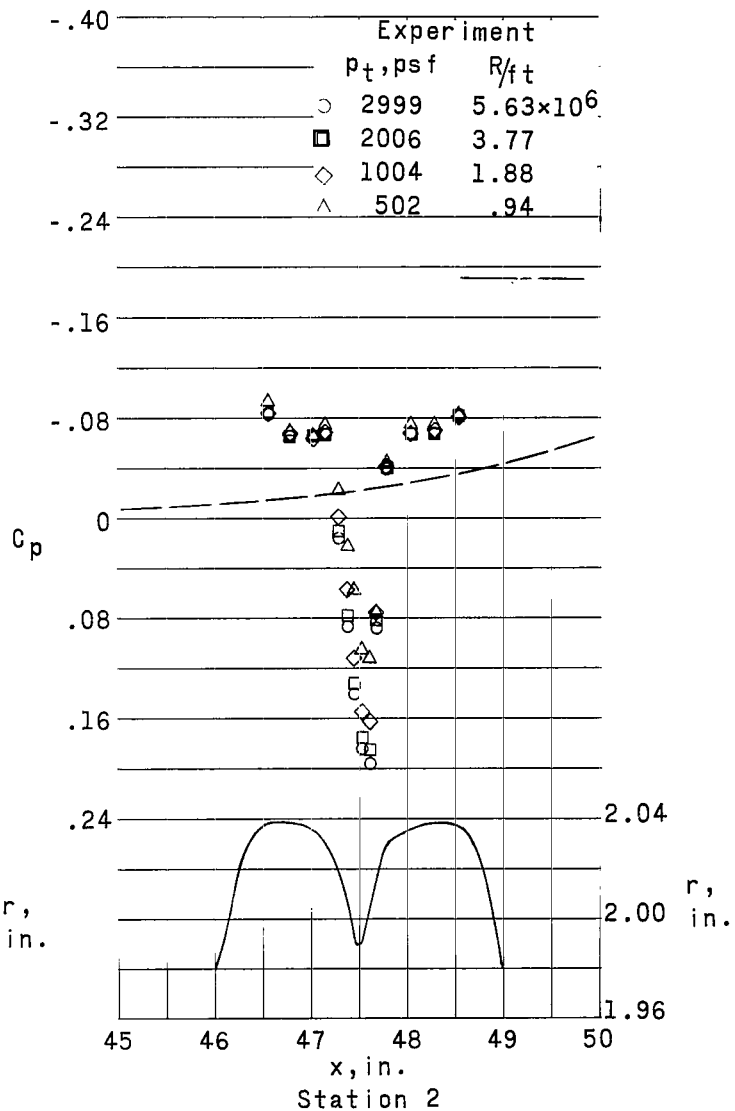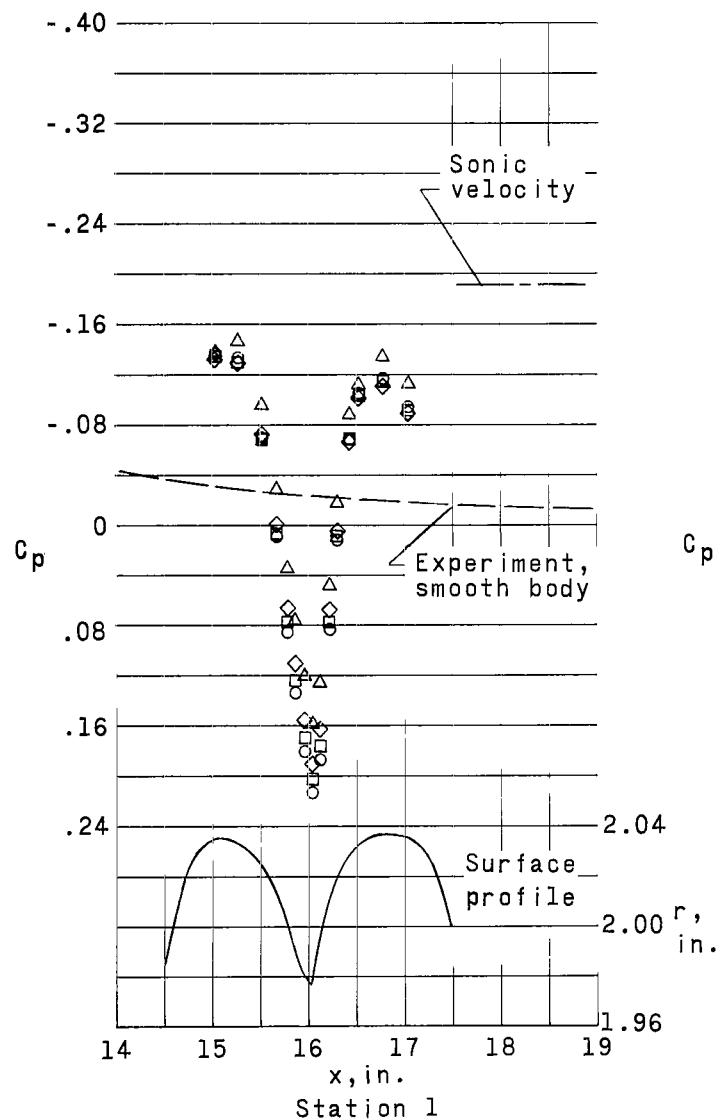
(b) $M_\infty = 0.90$.

Figure 8.- Continued.
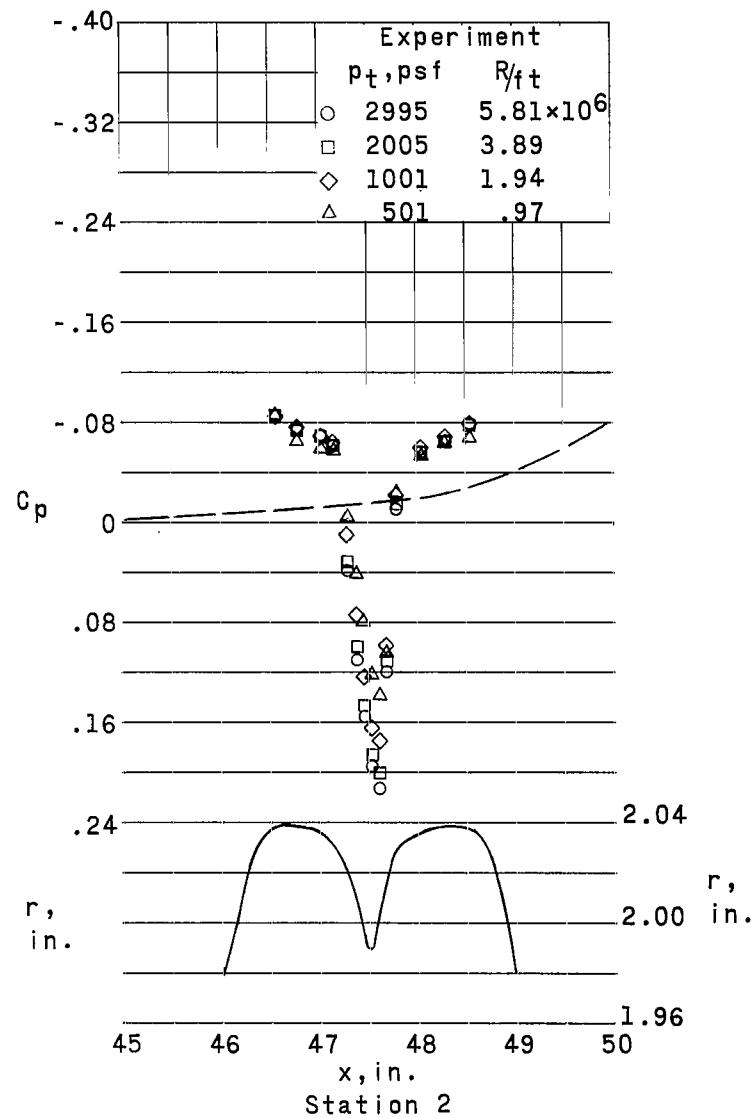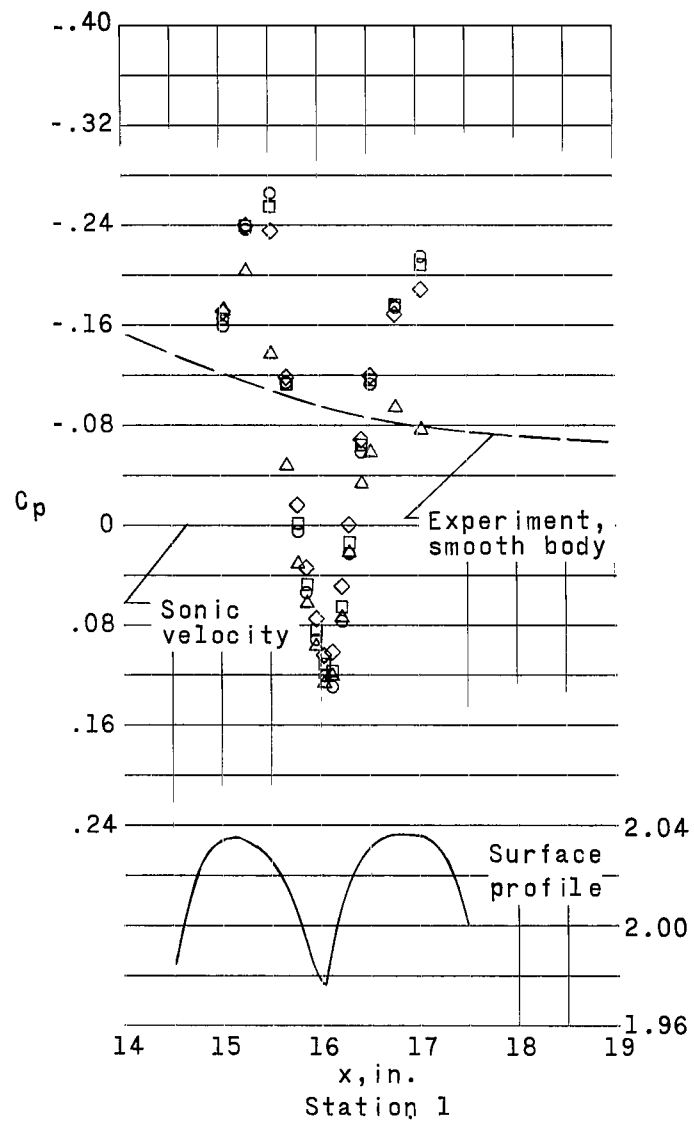
(c) $M_\infty = 1.00$.

Figure 8.- Continued.
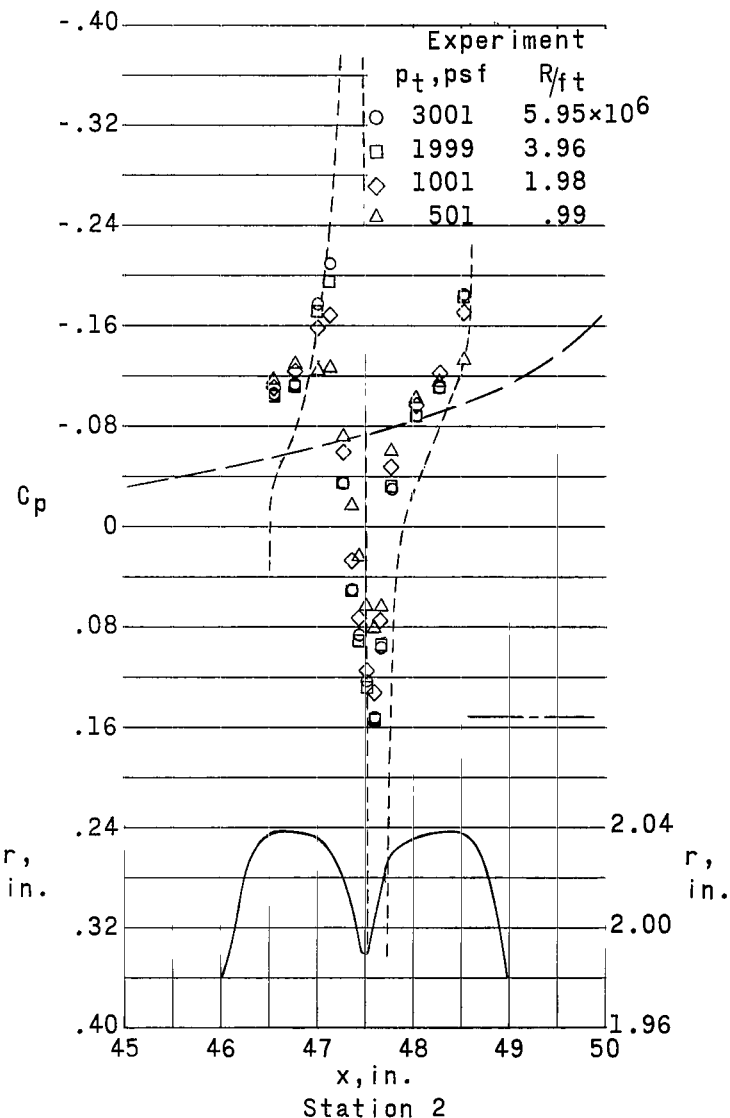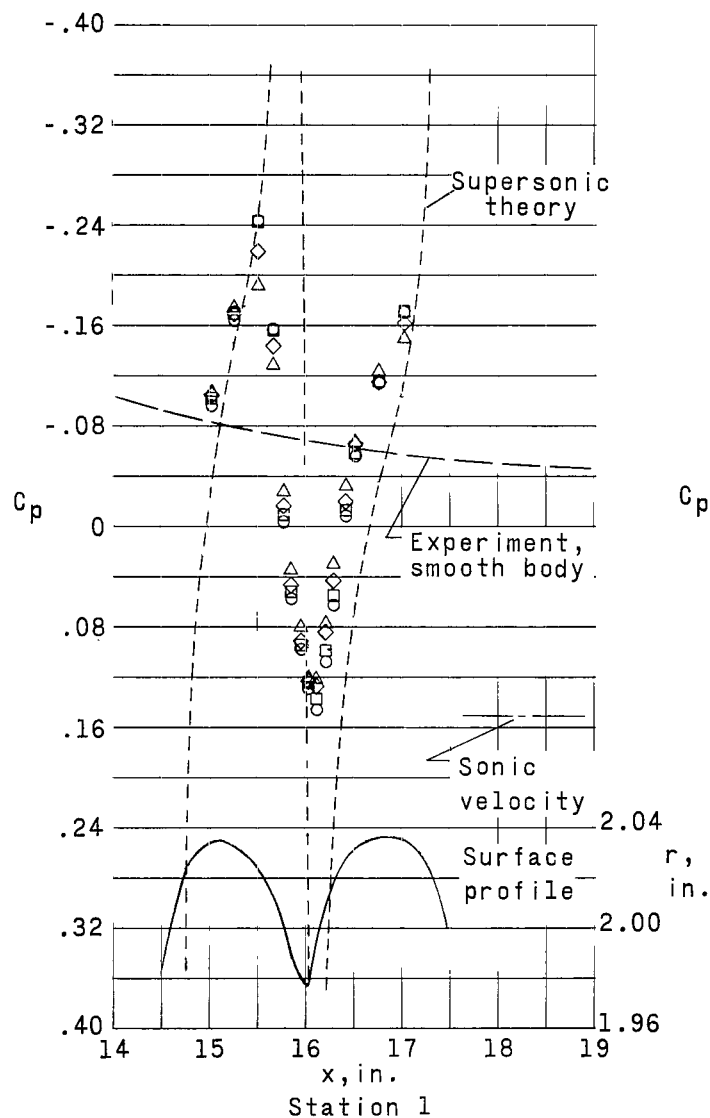
(d) $M_\infty = 1.10$.

Figure 8.- Continued.
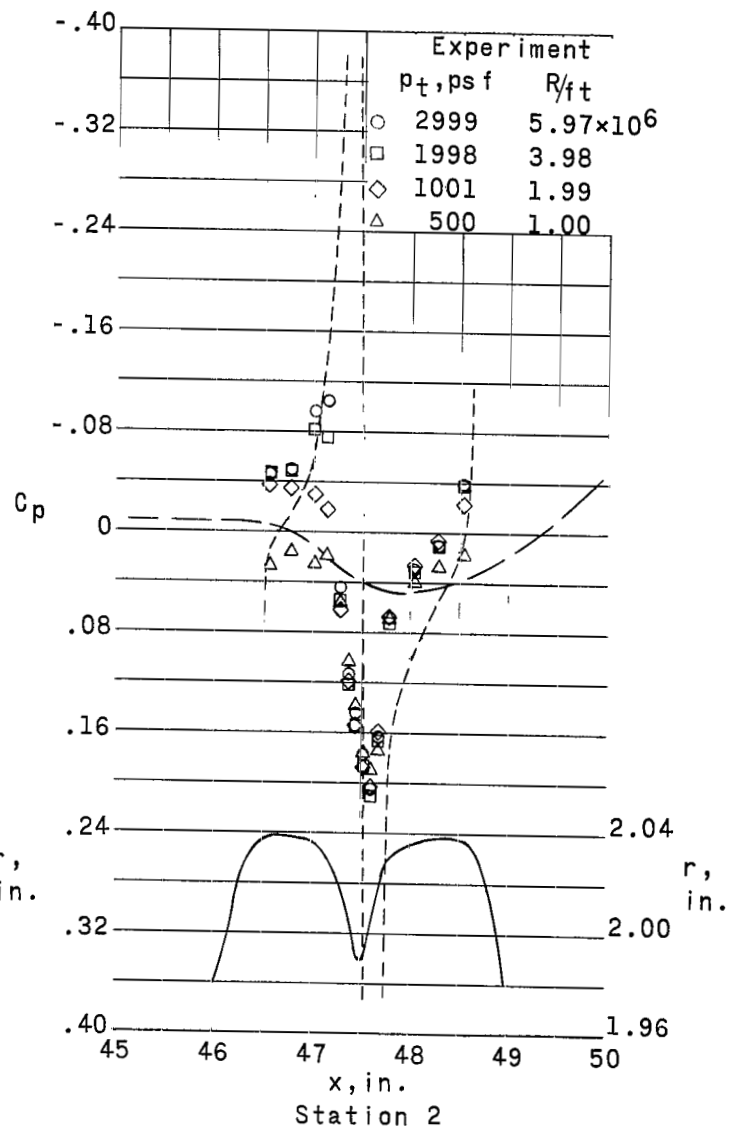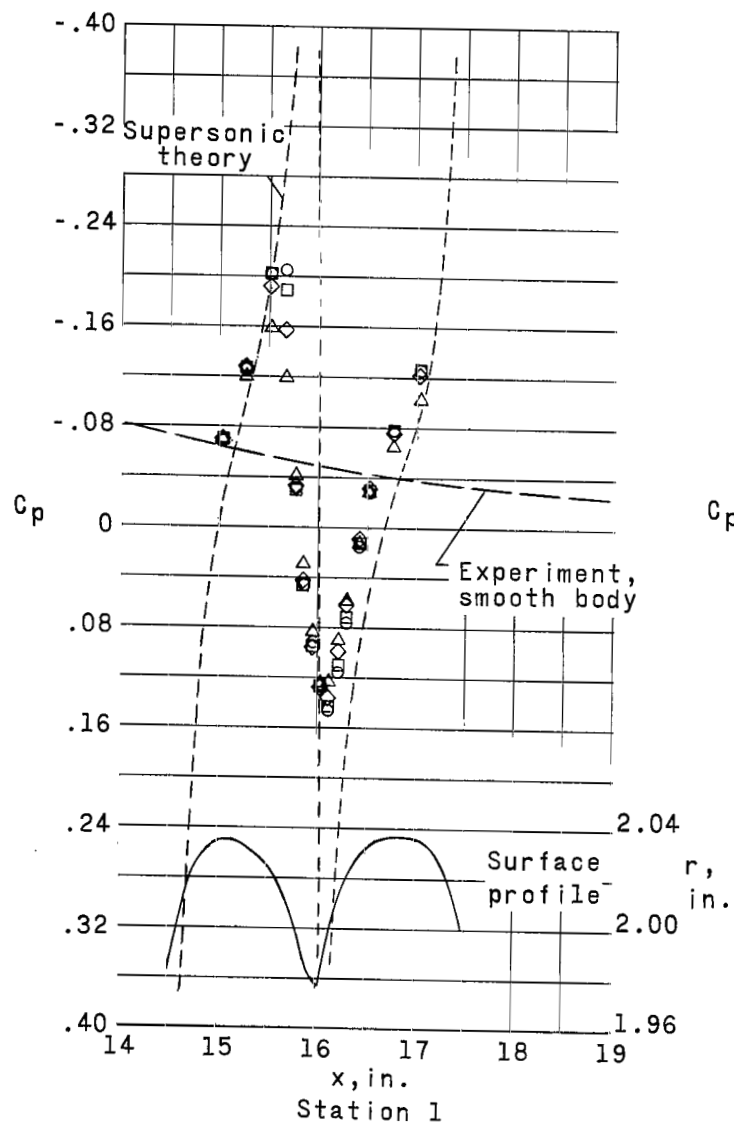
(e) $M_\infty = 1.20$.

Figure 8.- Concluded.
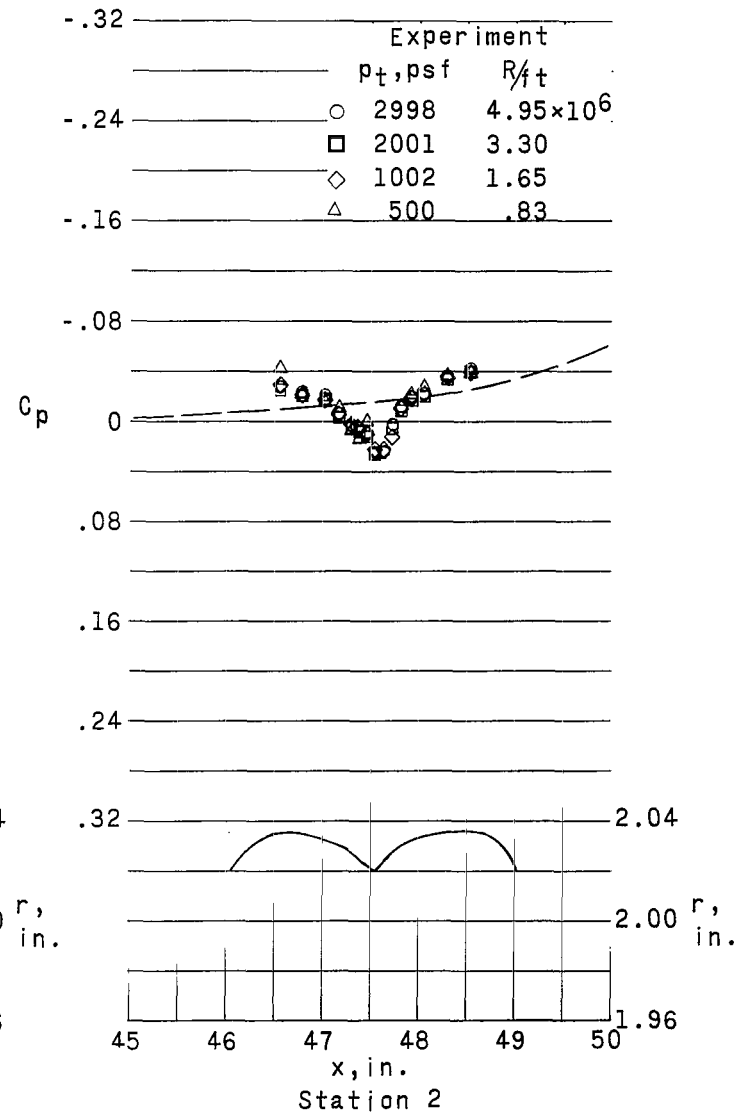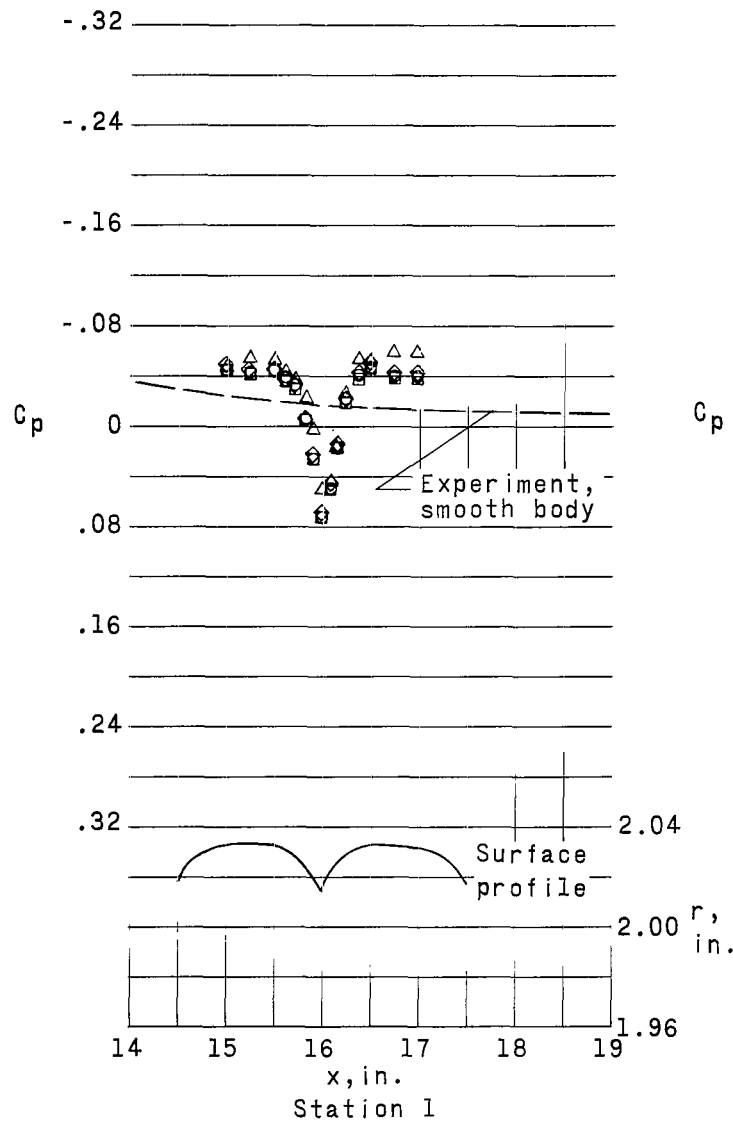
(a) $M_\infty = 0.70$.

Figure 9.- Pressure distributions over model with 0.017-inch transverse creases at constant M_∞.
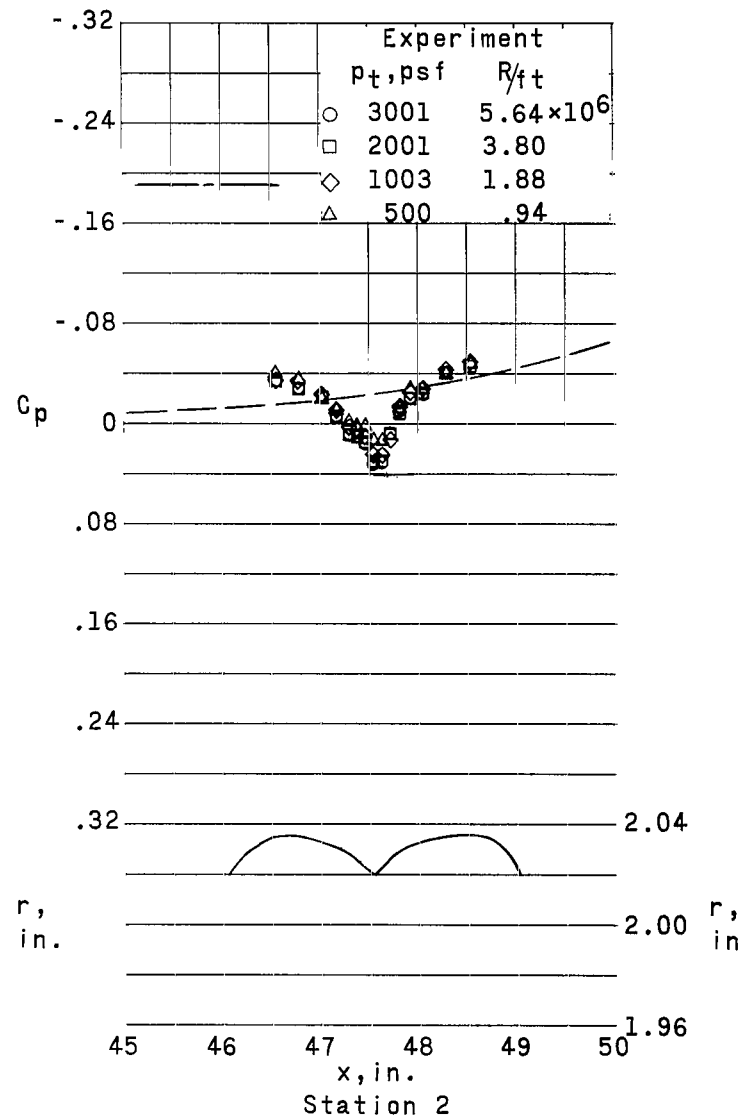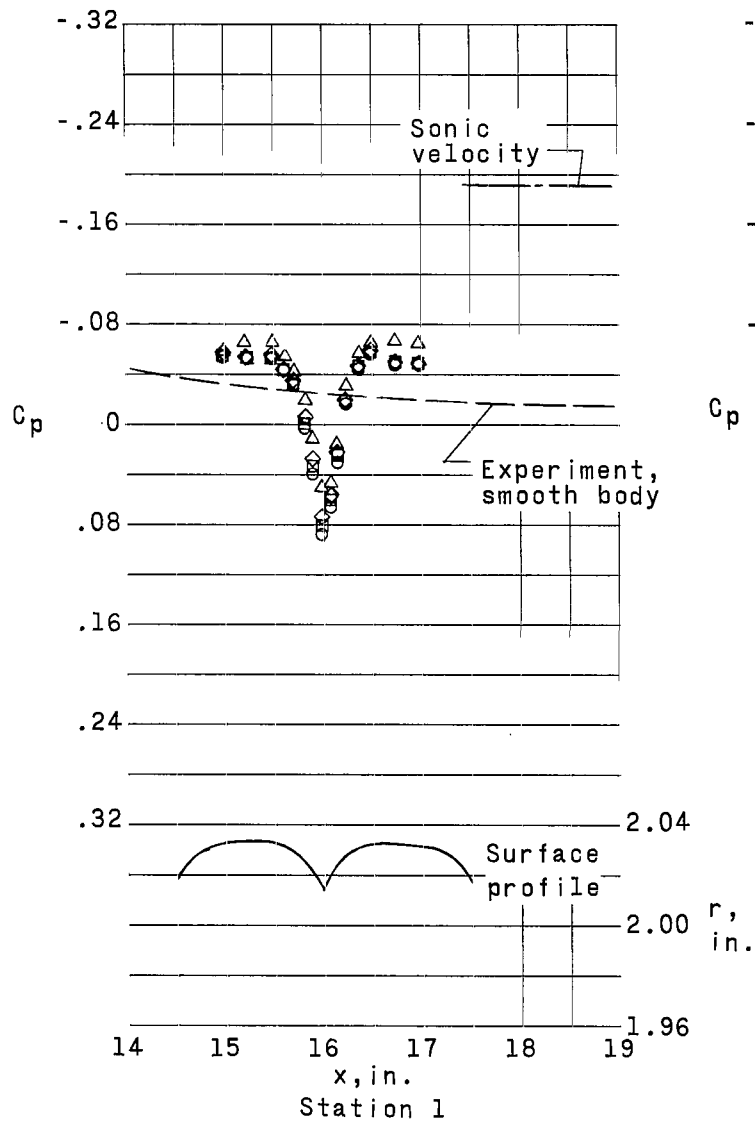
(b) $M_\infty = 0.90$.

Figure 9.- Continued.
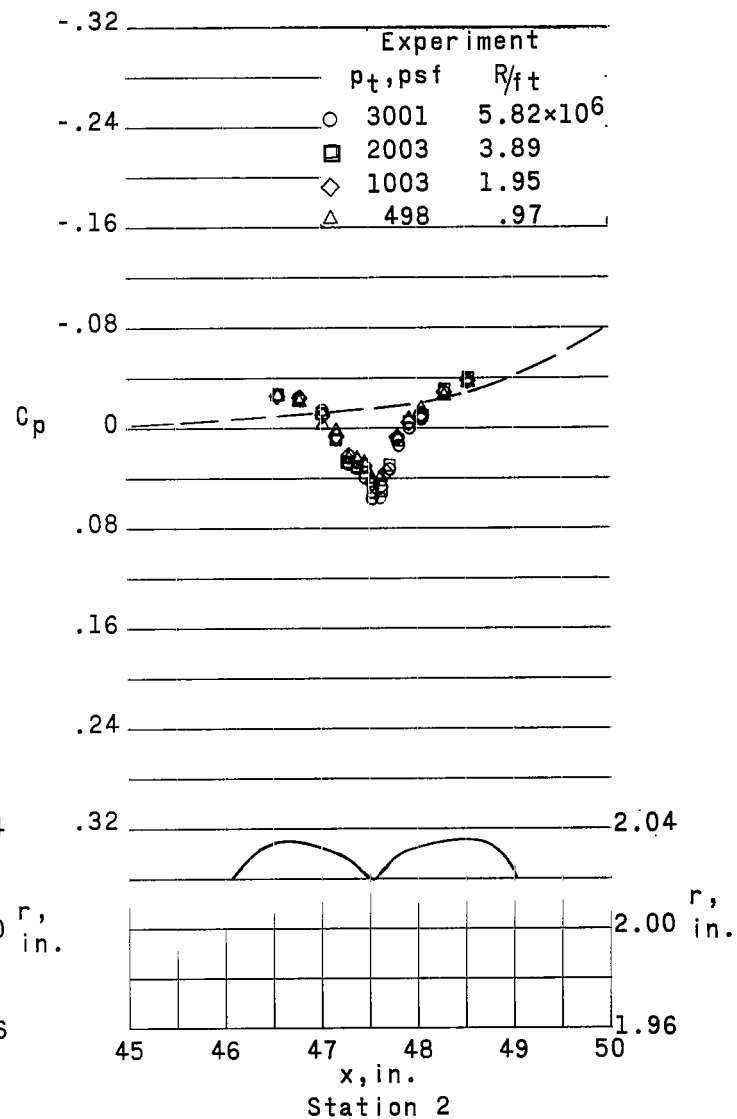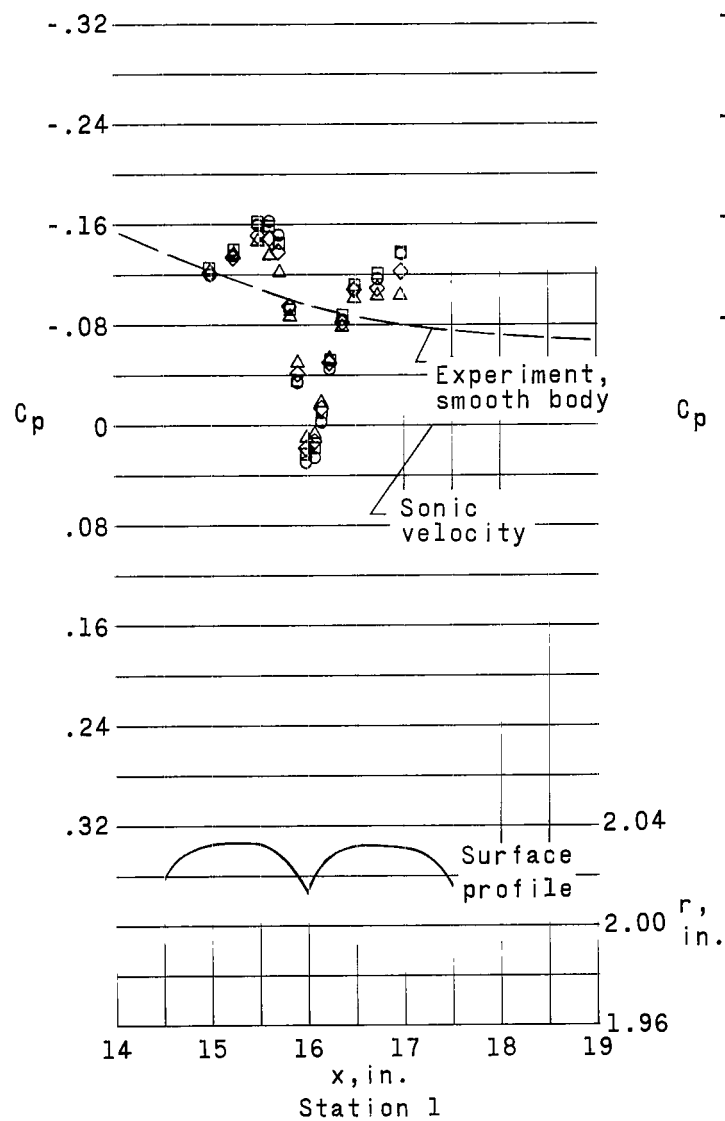
(c) $M_\infty = 1.00$.

Figure 9.- Continued.
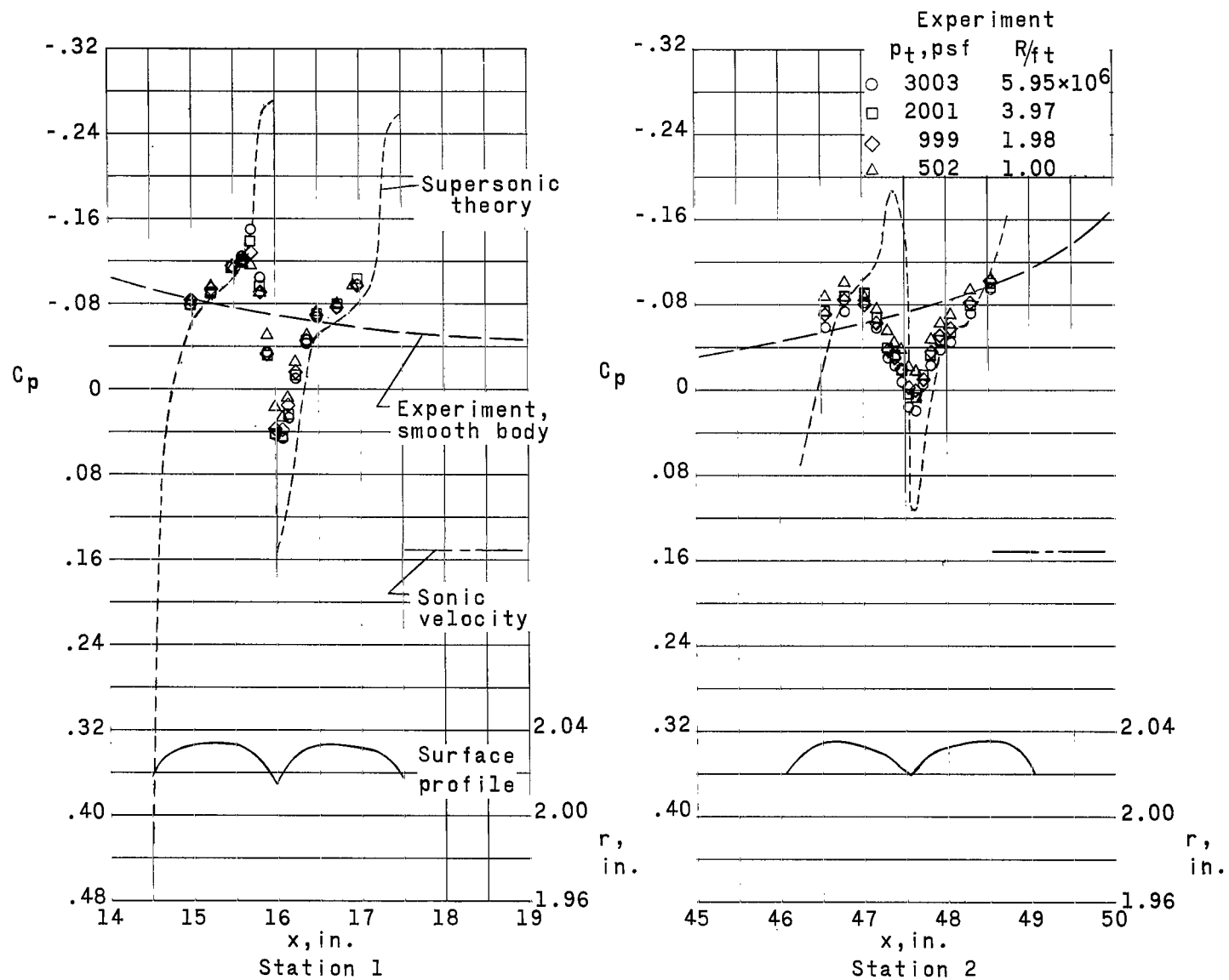
(d) $M_\infty = 1.10$.

Figure 9.- Continued.
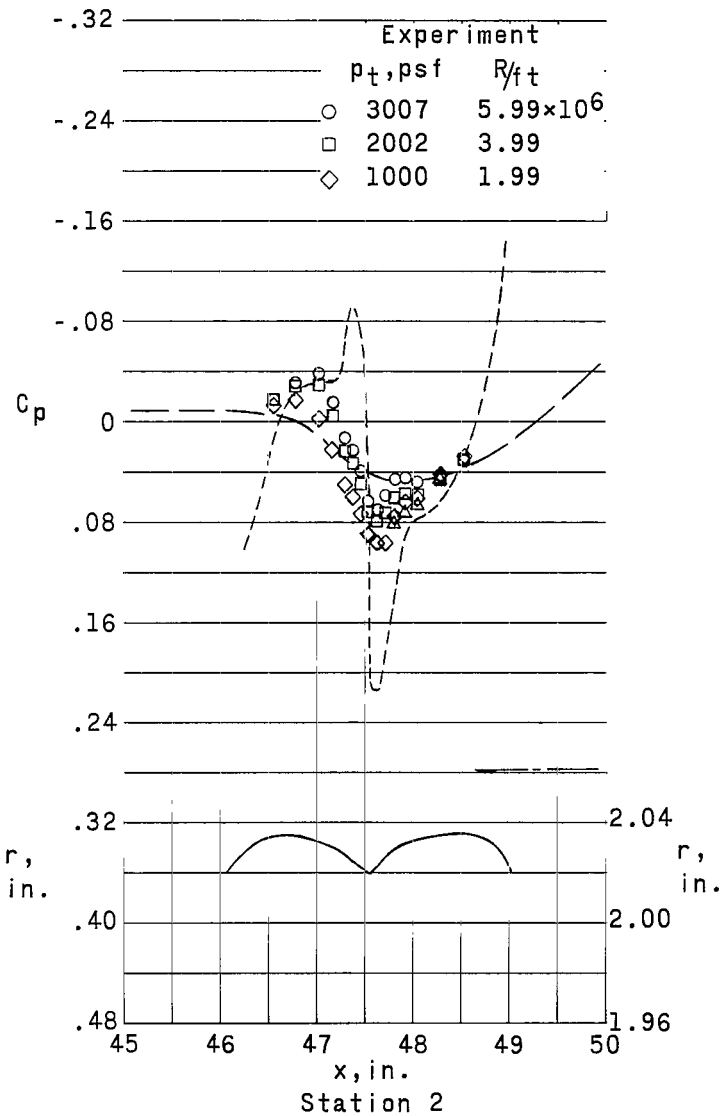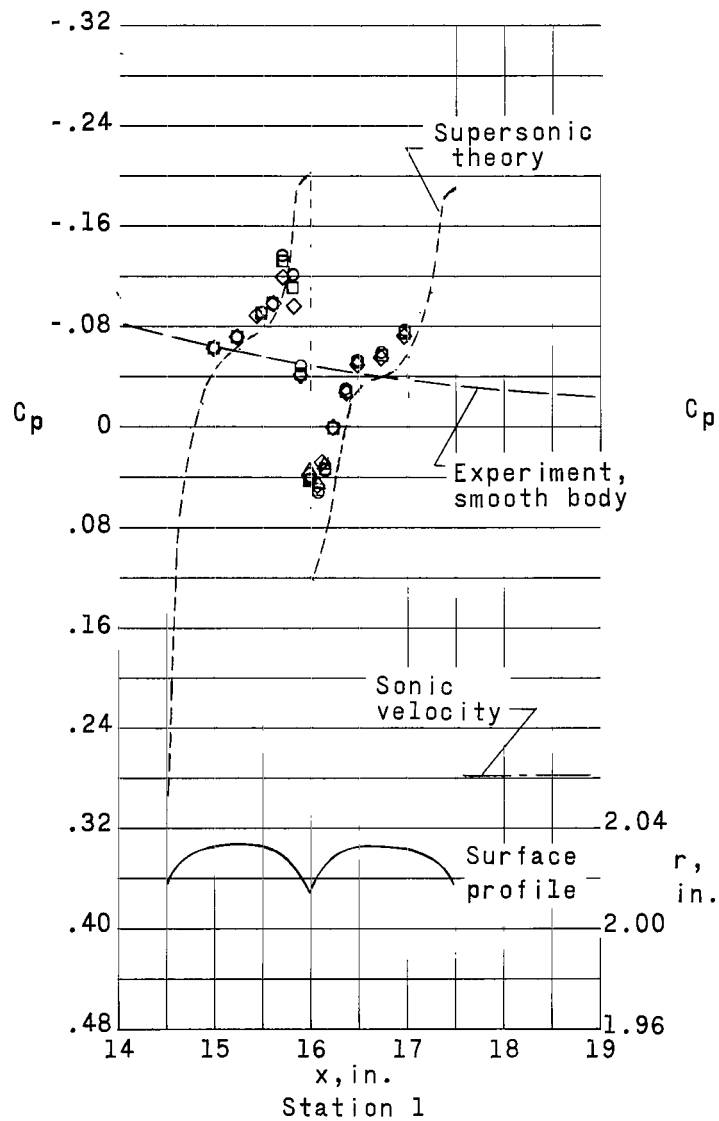
(e) $M_\infty = 1.20$.

Figure 9.- Concluded.
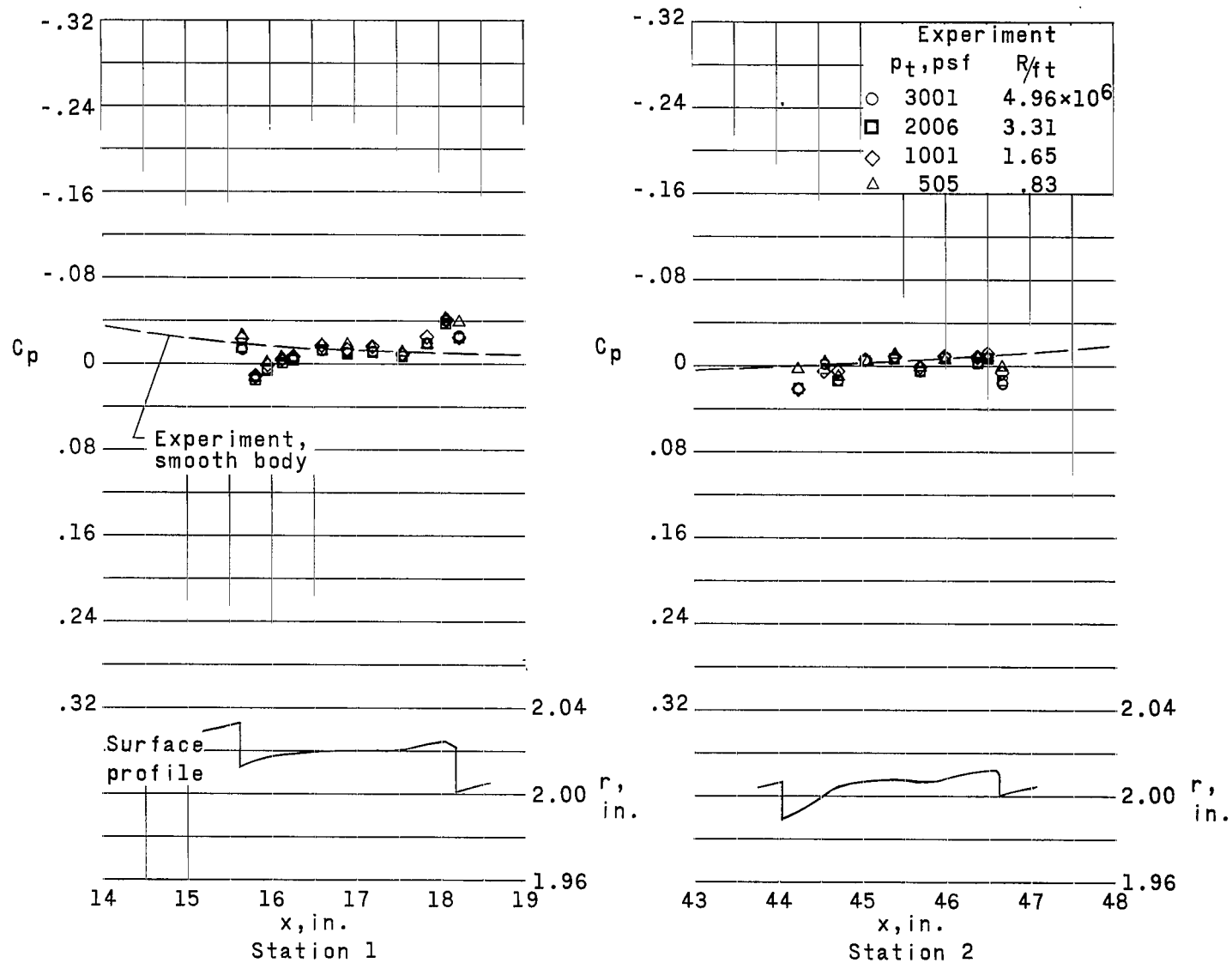
(a) $M_\infty = 0.70$.

Figure 10.- Pressure distributions over model with 0.020-inch 45° rearward steps at constant M_∞.
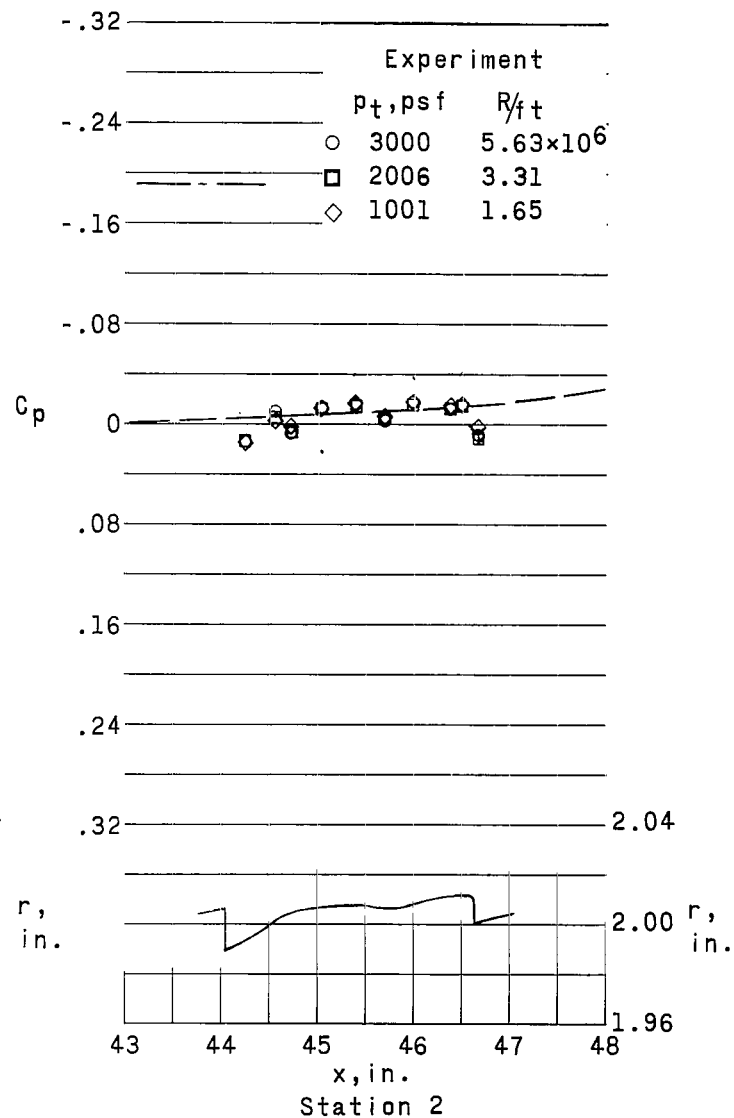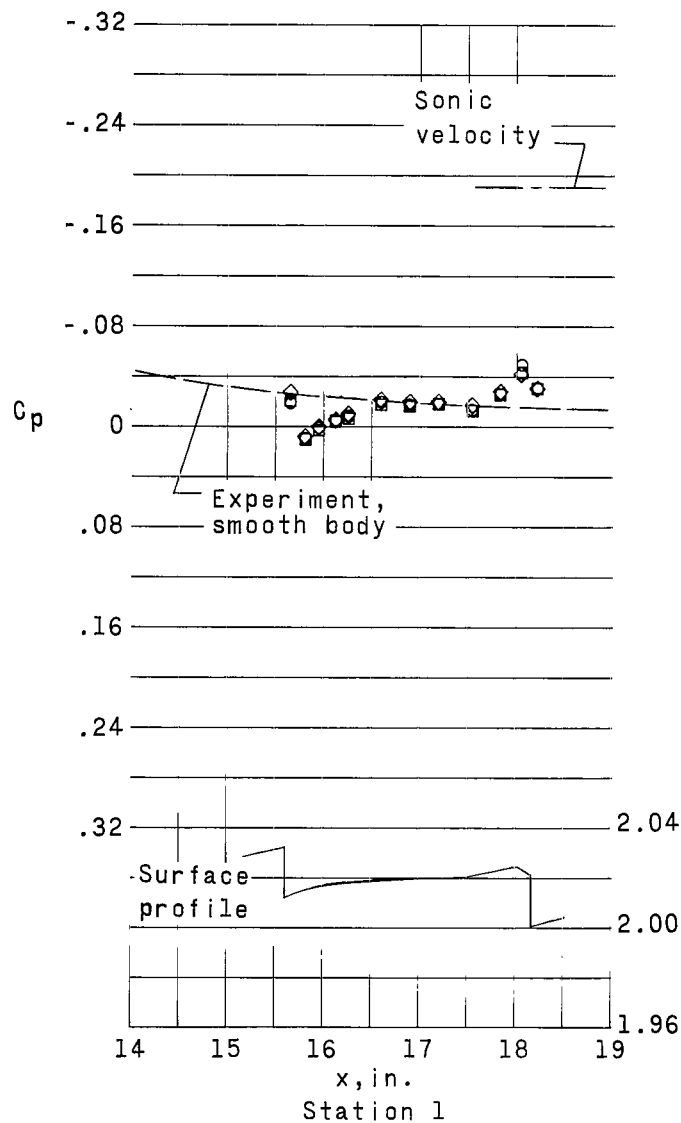
(b) $M_\infty = 0.90$.

Figure 10.- Continued.
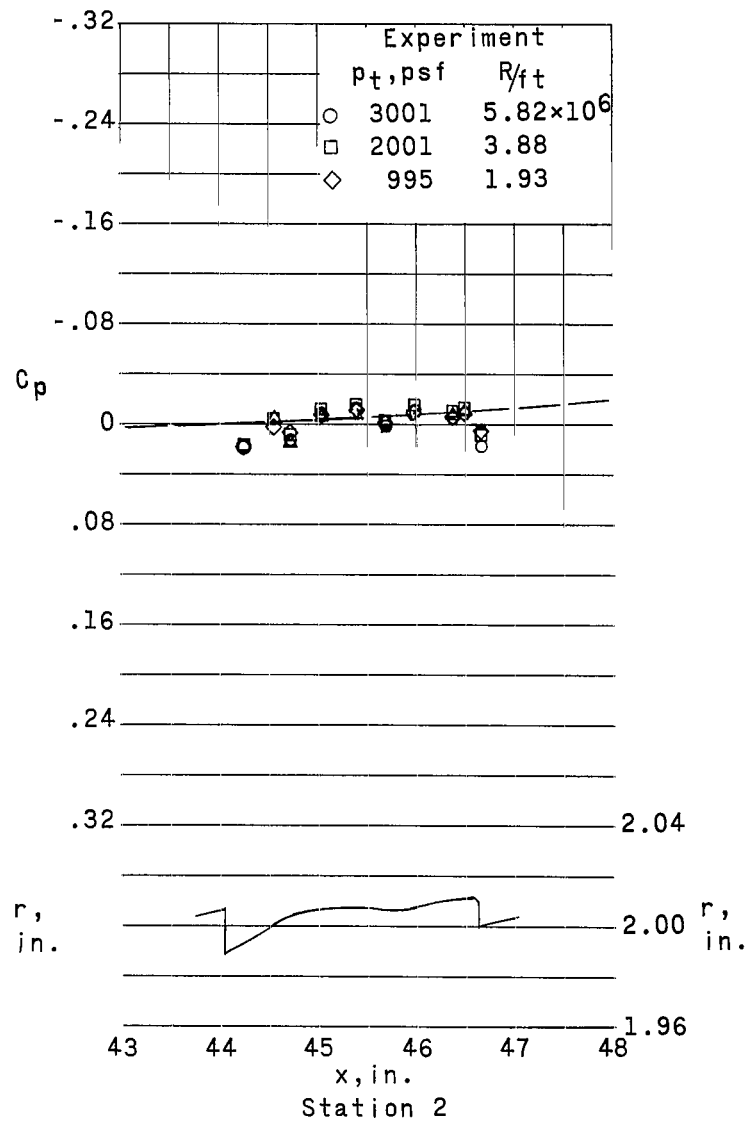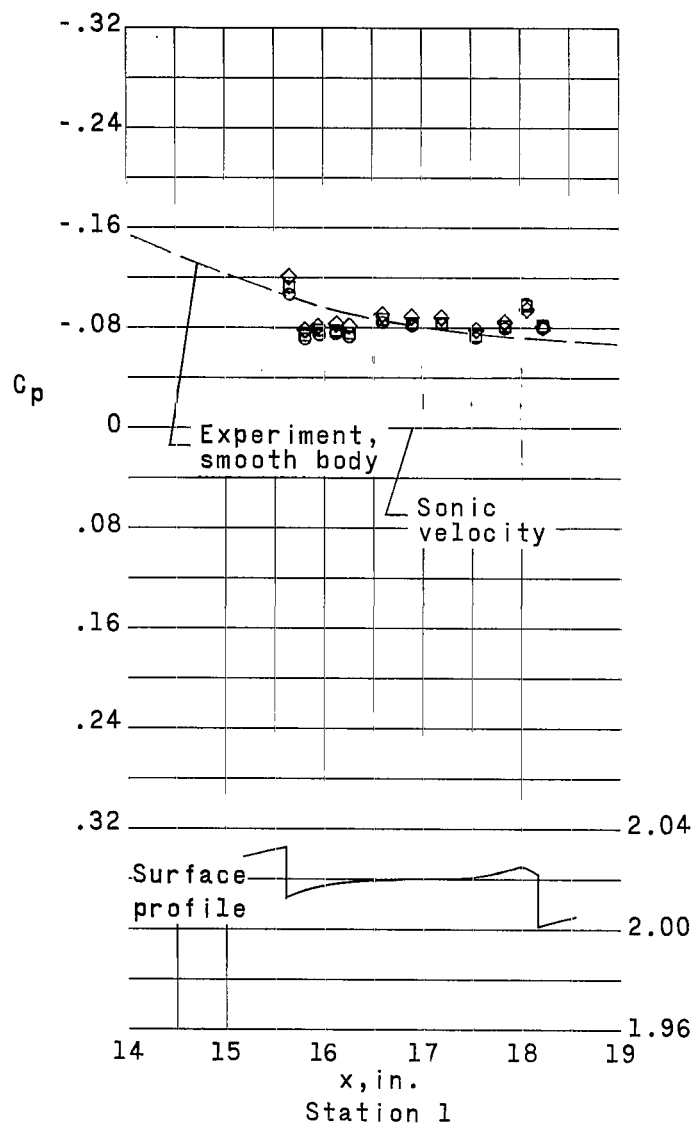
(c) $M_\infty = 1.00$.

Figure 10.- Continued.
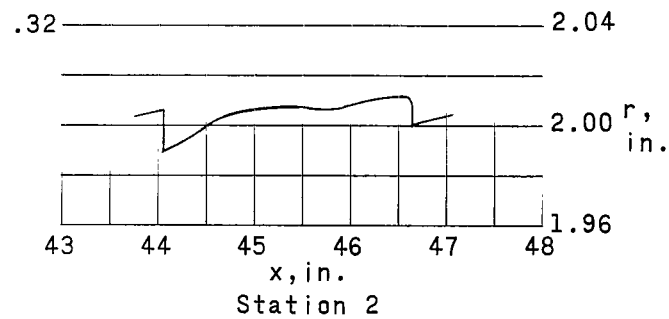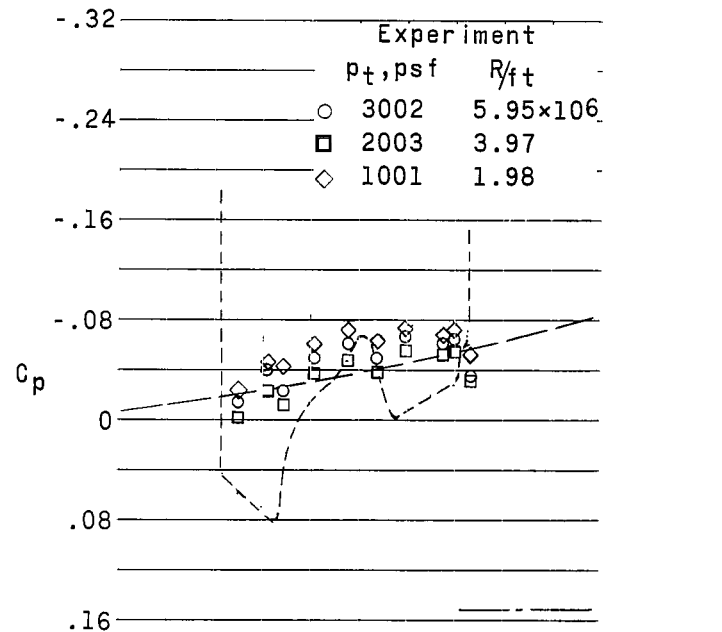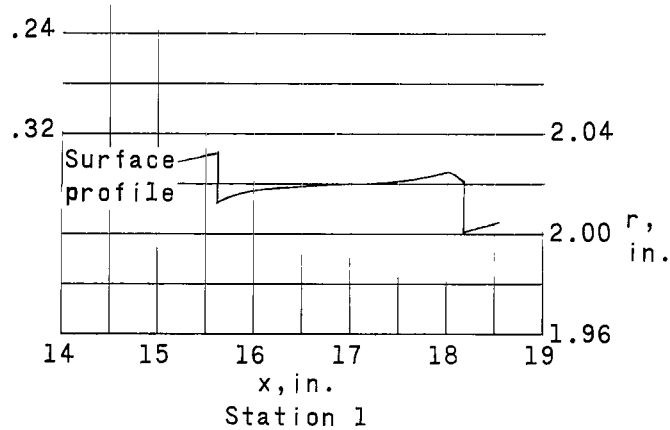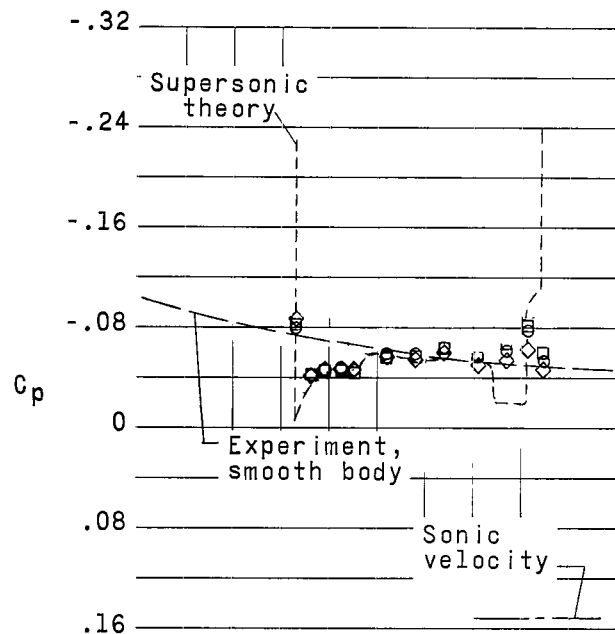
(d) $M_\infty = 1.10$.

Figure 10.- Continued.
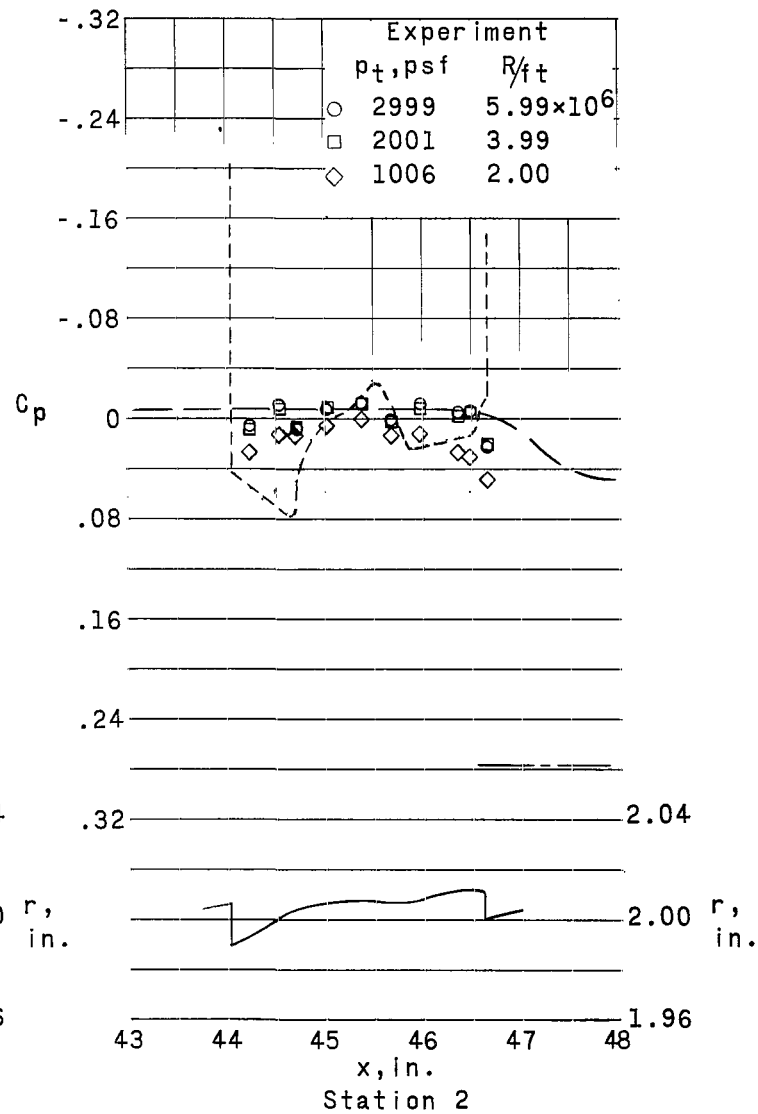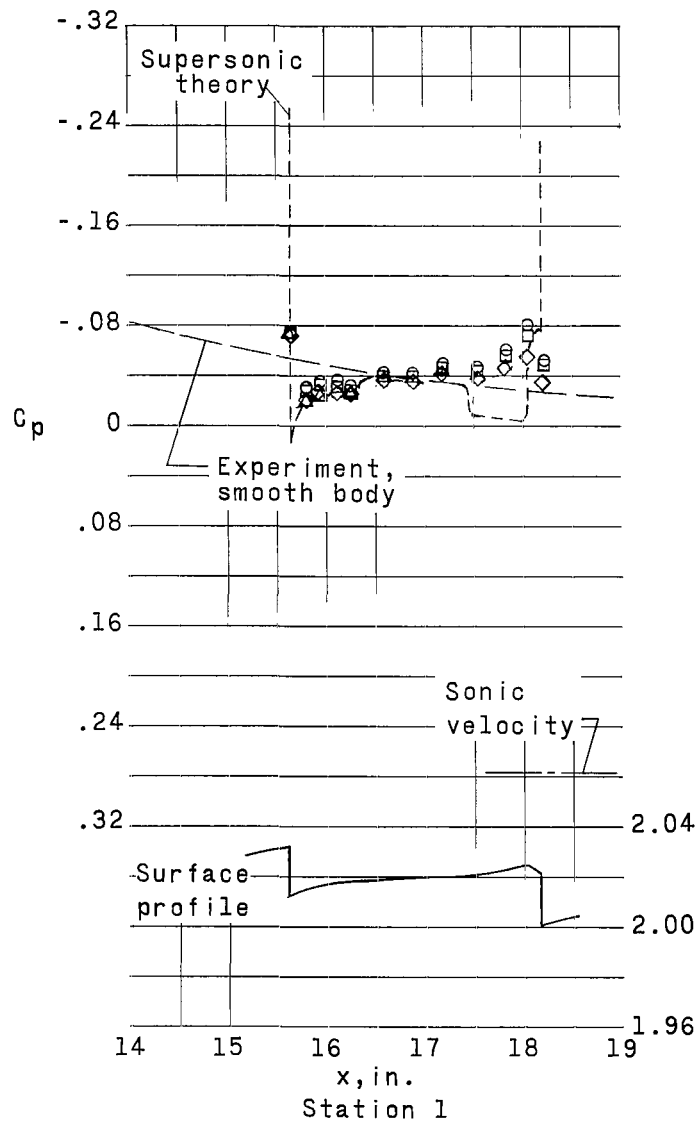
(e) $M_\infty = 1.20$.

Figure 10.- Concluded.
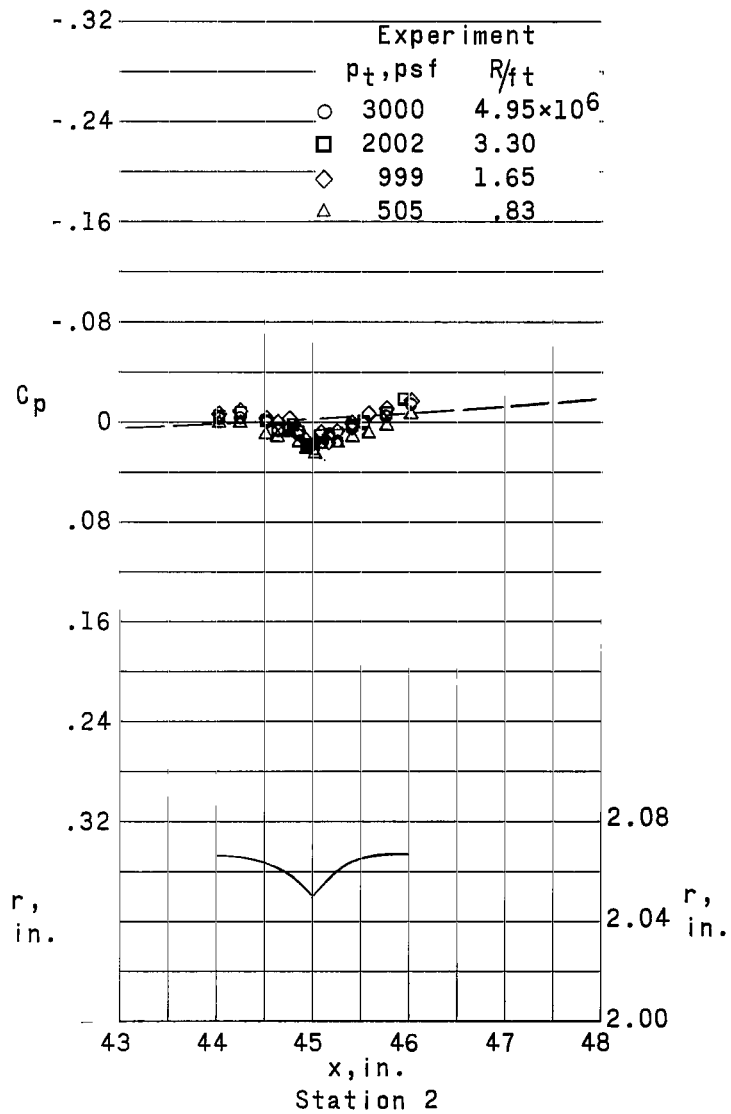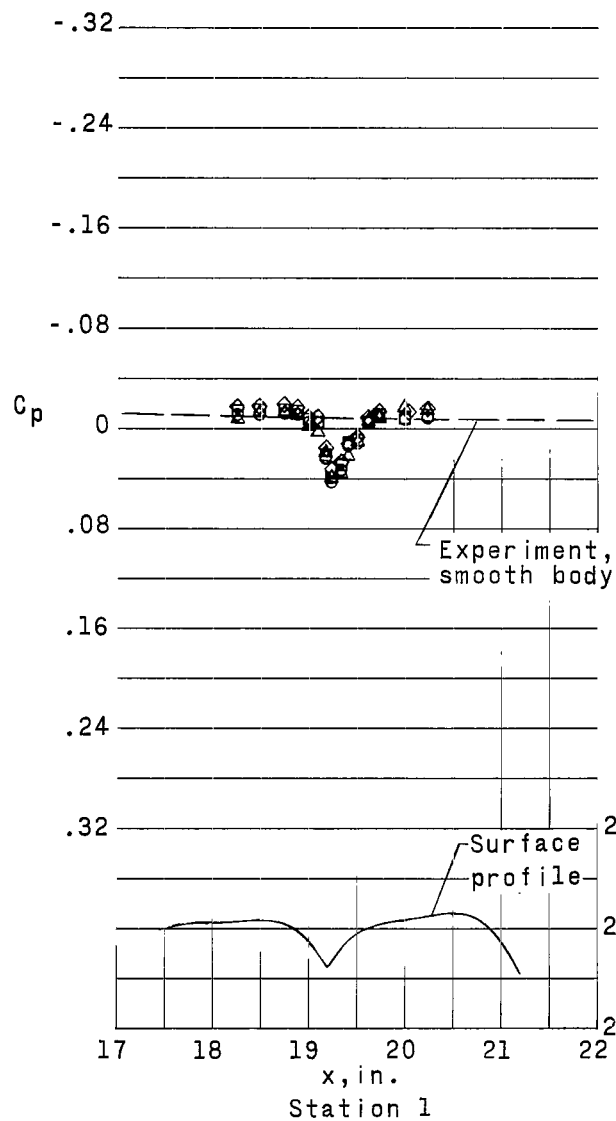
(a) $M_\infty = 0.70.$

Figure 11.-   Pressure distributions over model with 0.014-inch 45° creases at constant M_∞.
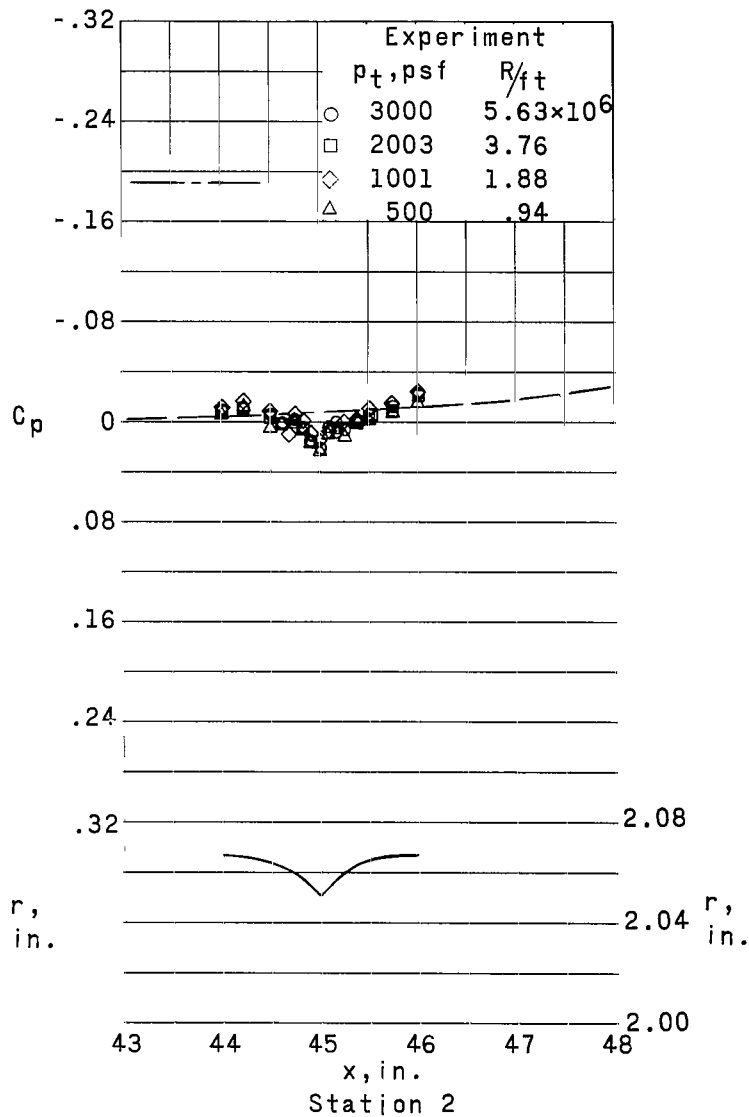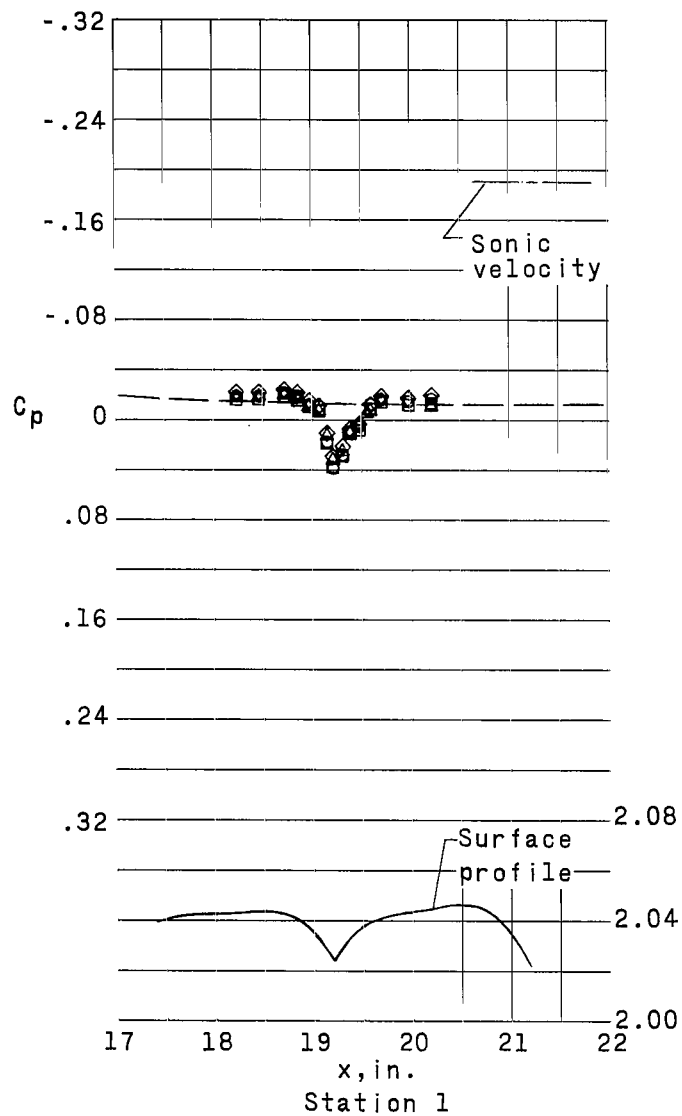
(b) $M_\infty = 0.90$.

Figure 11.- Continued.
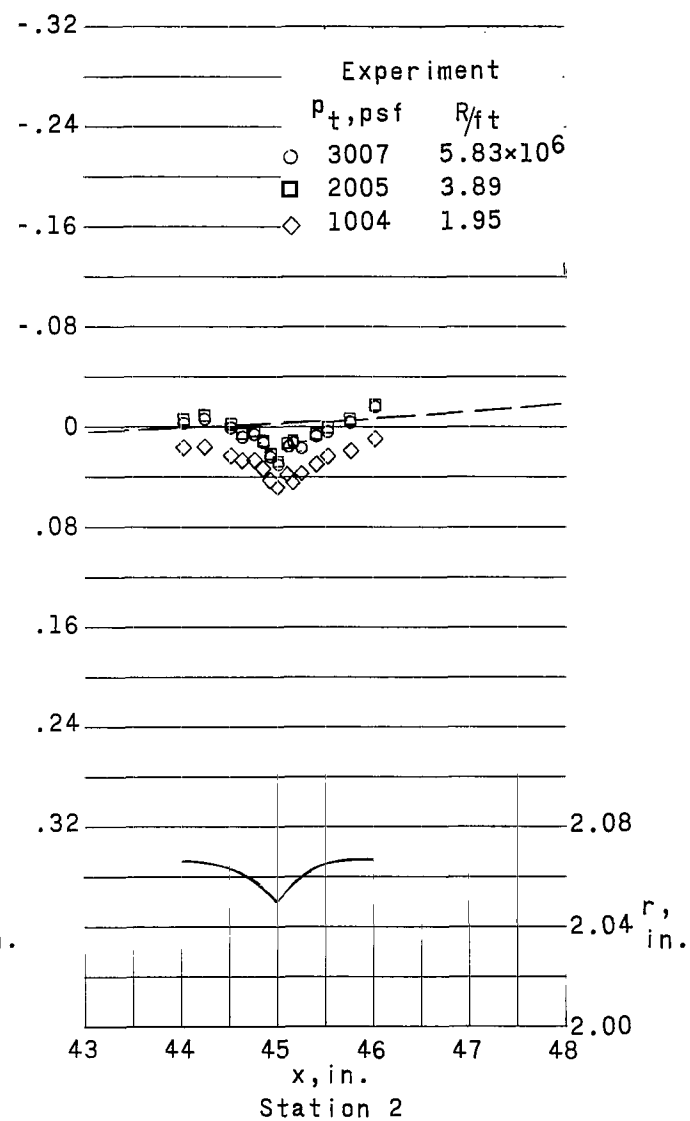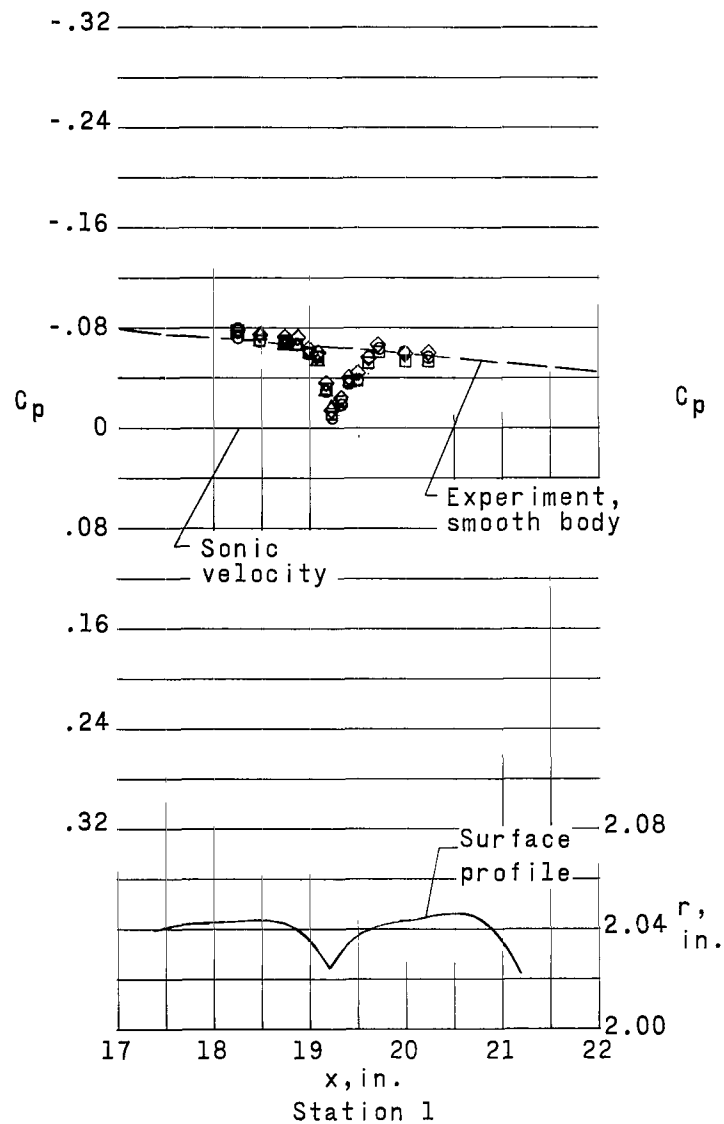
(c) $M_\infty = 1.00$.

Figure 11.- Continued.

(d) $M_\infty = 1.10$.

Figure 11.- Continued.

C_p

−.32
−.24
−.16
−.08
0
.08
.16
.24
.32

Supersonic theory

Experiment, smooth body

Sonic velocity

Surface profile

2.08
2.04 r, in.
2.00

17   18   19   20   21   22

x, in.

Station 1

C_p

−.32
−.24
−.16
−.08
0
.08
.16
.24
.32

Experiment		
p_t, psf	R/ft	
○	3009	5.99×10^6
□	2011	4.01
◇	1000	1.99

2.08
2.04 r, in.
2.00

43   44   45   46   47   48

x, in.

Station 2
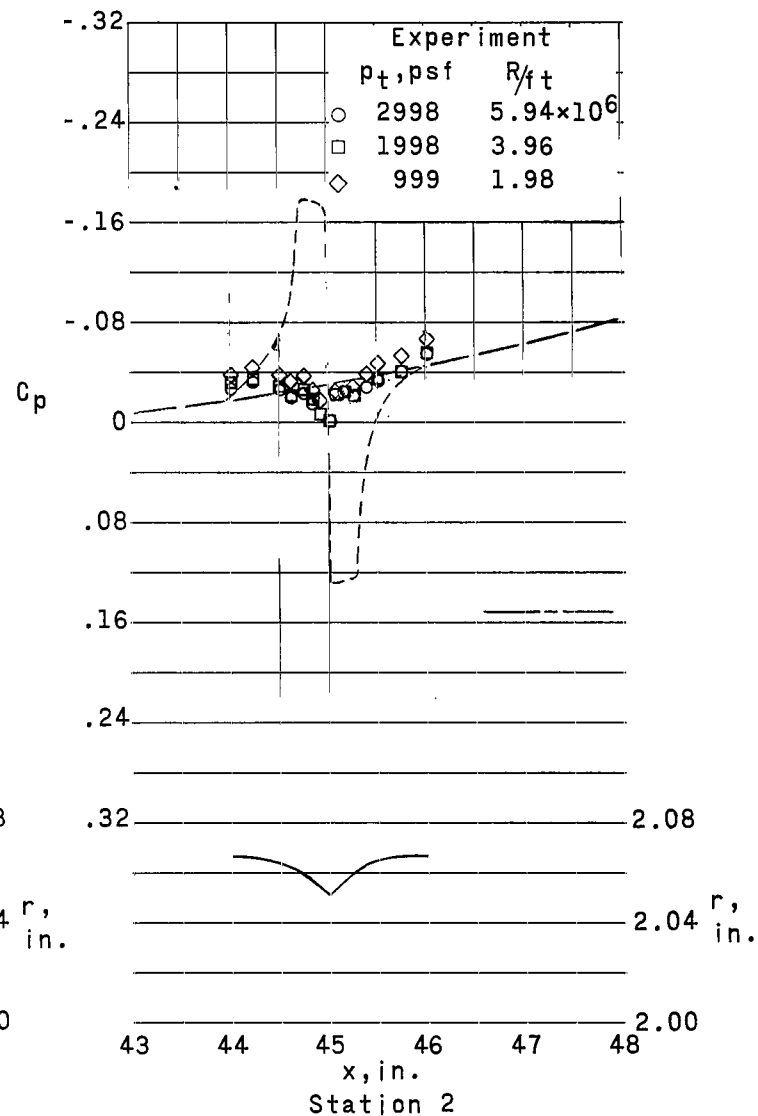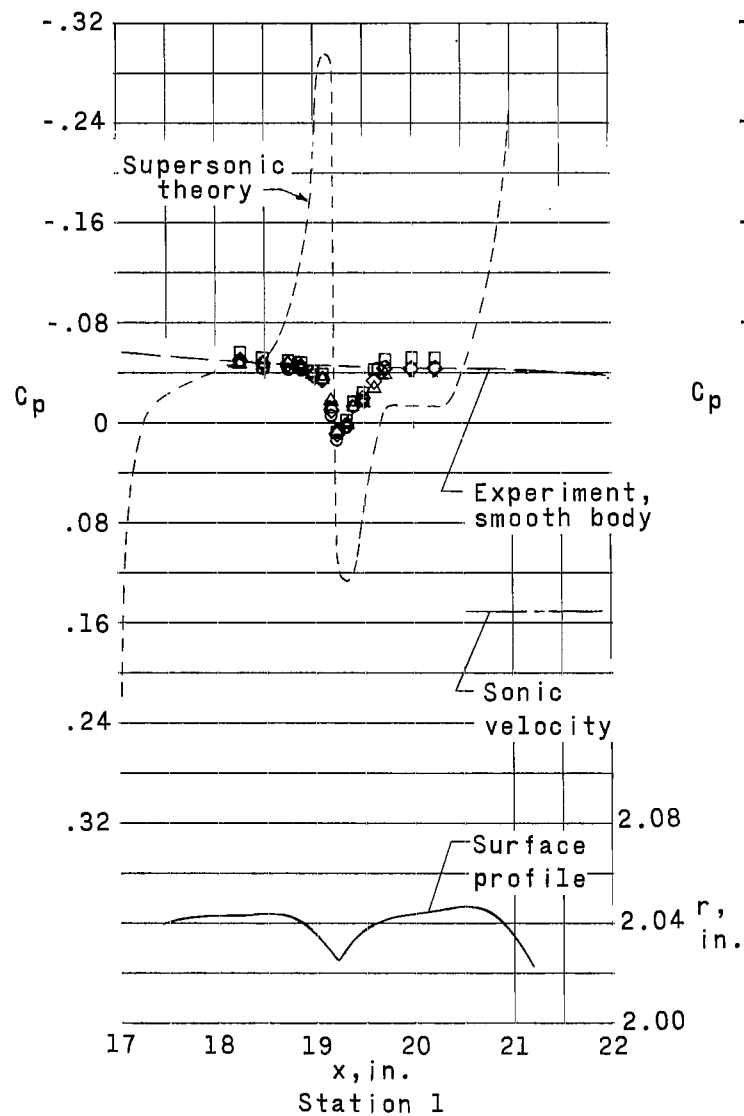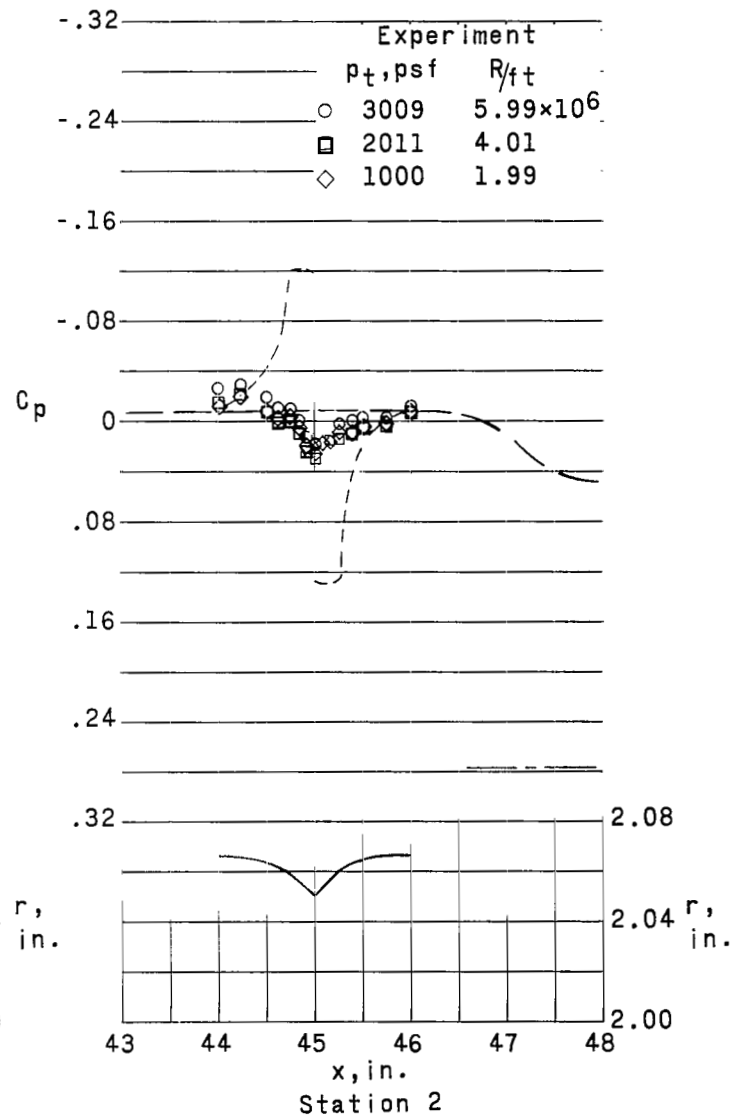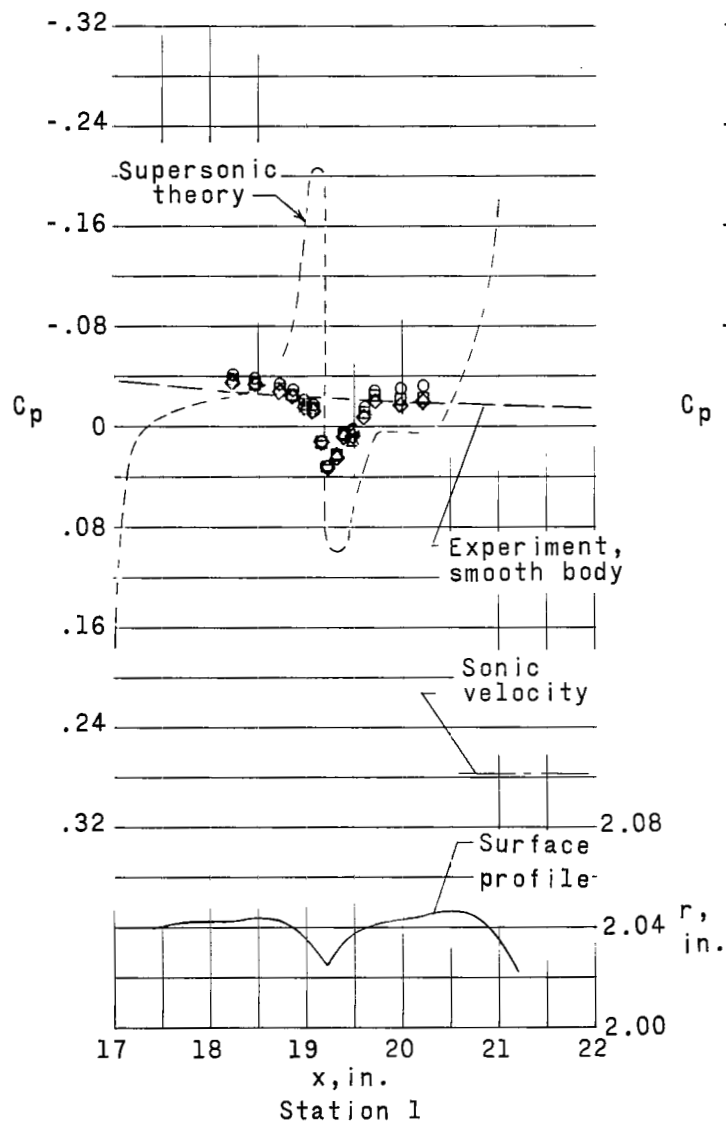
(e) $M_\infty = 1.20$.

Figure 11.- Concluded.
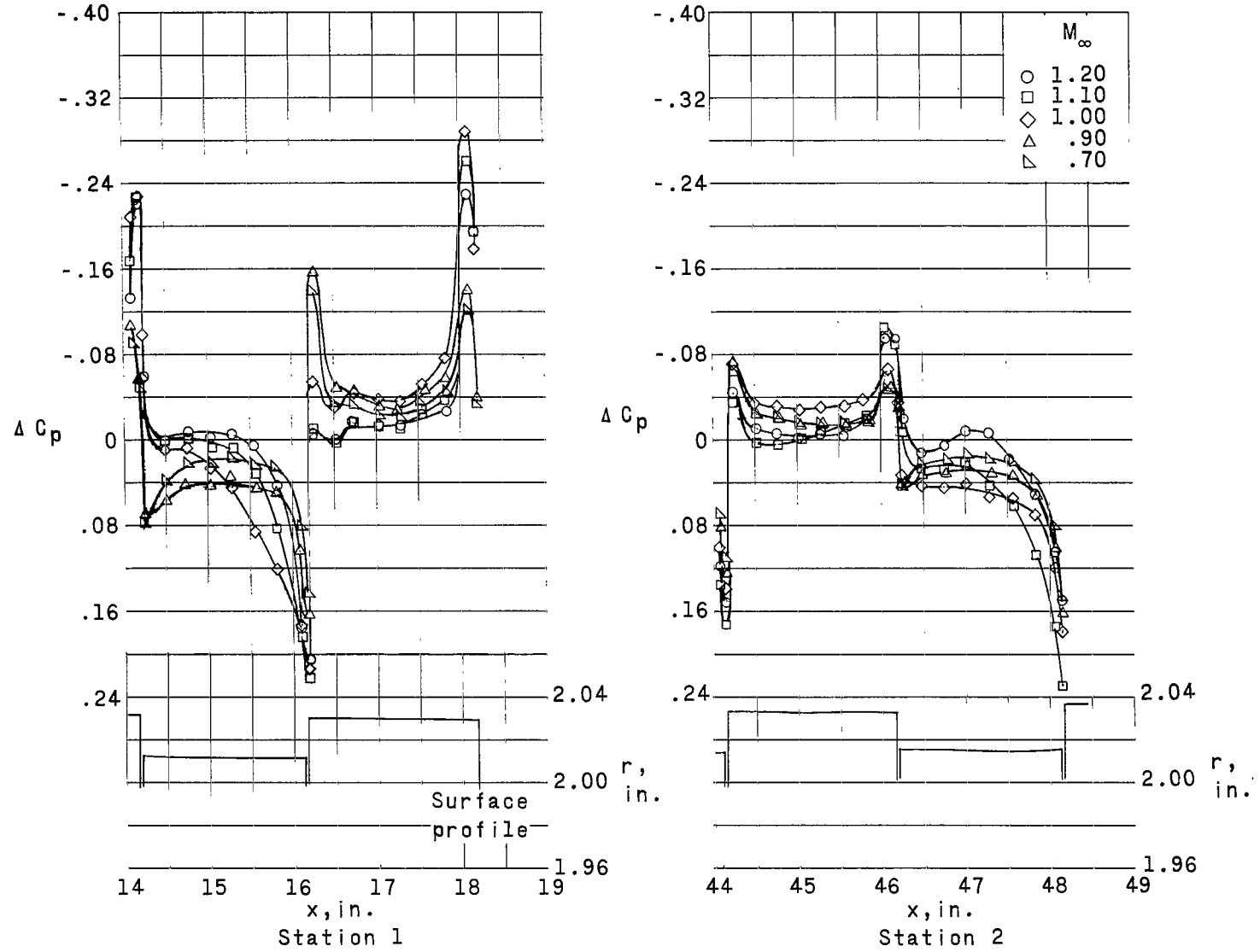
(a) p_t = 3000 psf.

Figure 12.- Pressure distributions over model with 0.021-inch steps with grooves at constant p_t.
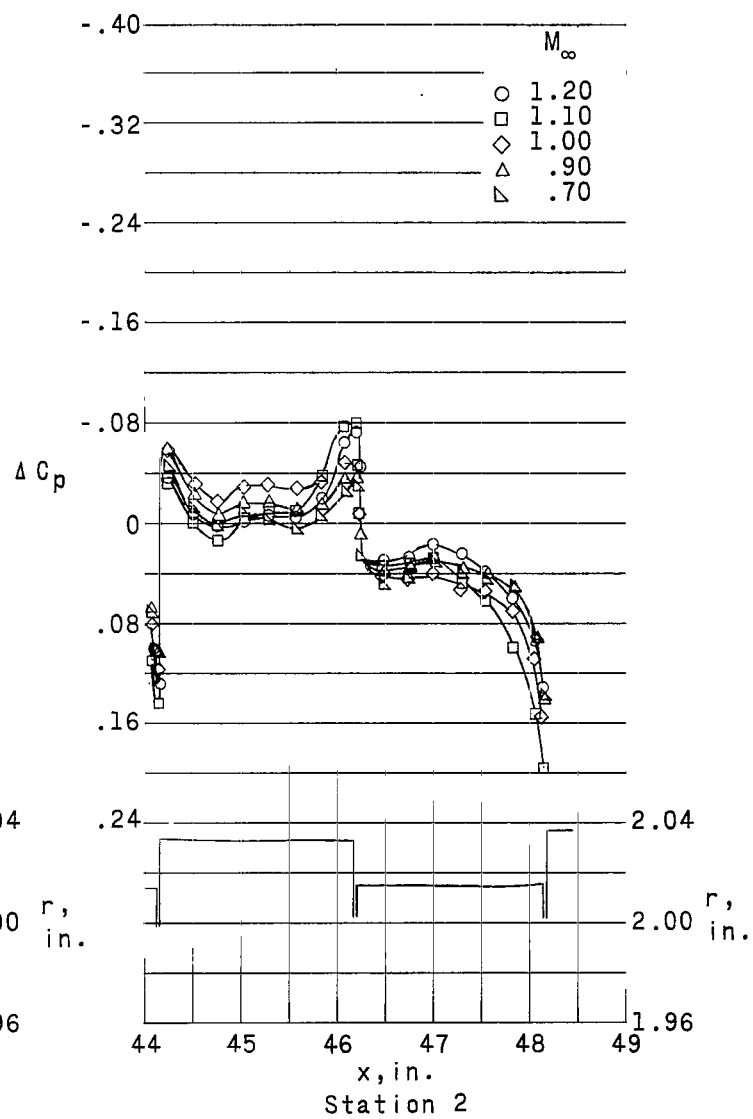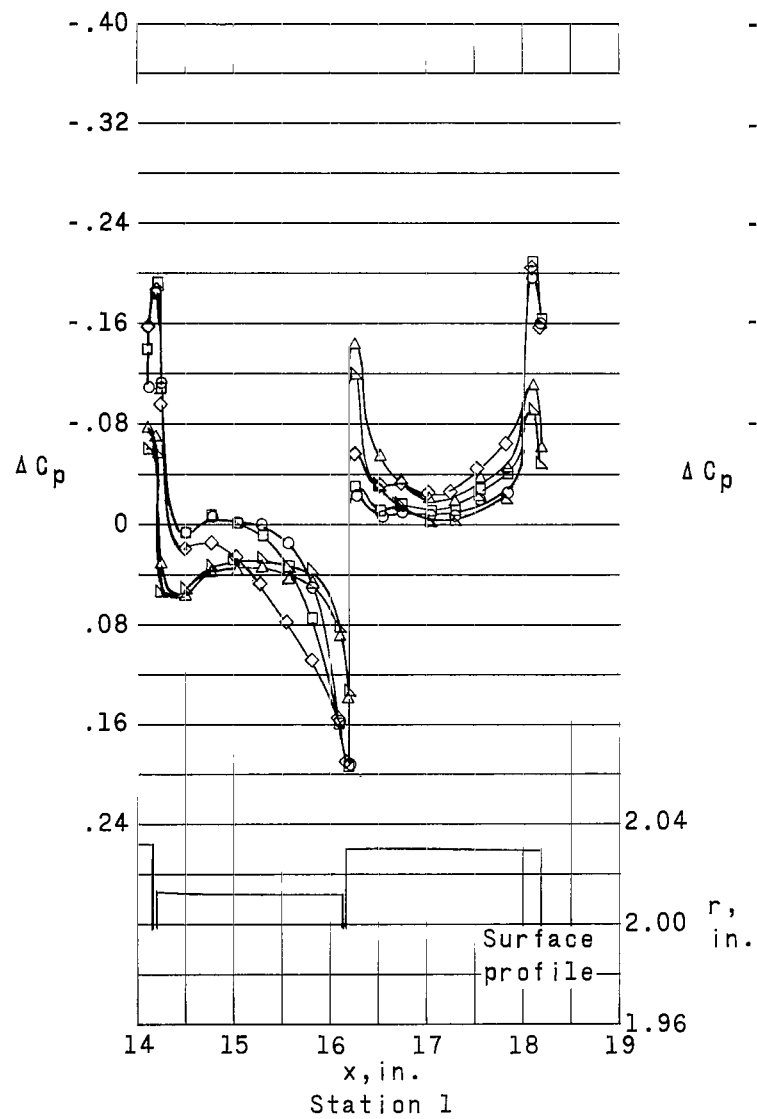
(b) $p_t = 1000$ psf.

Figure 12.- Concluded.
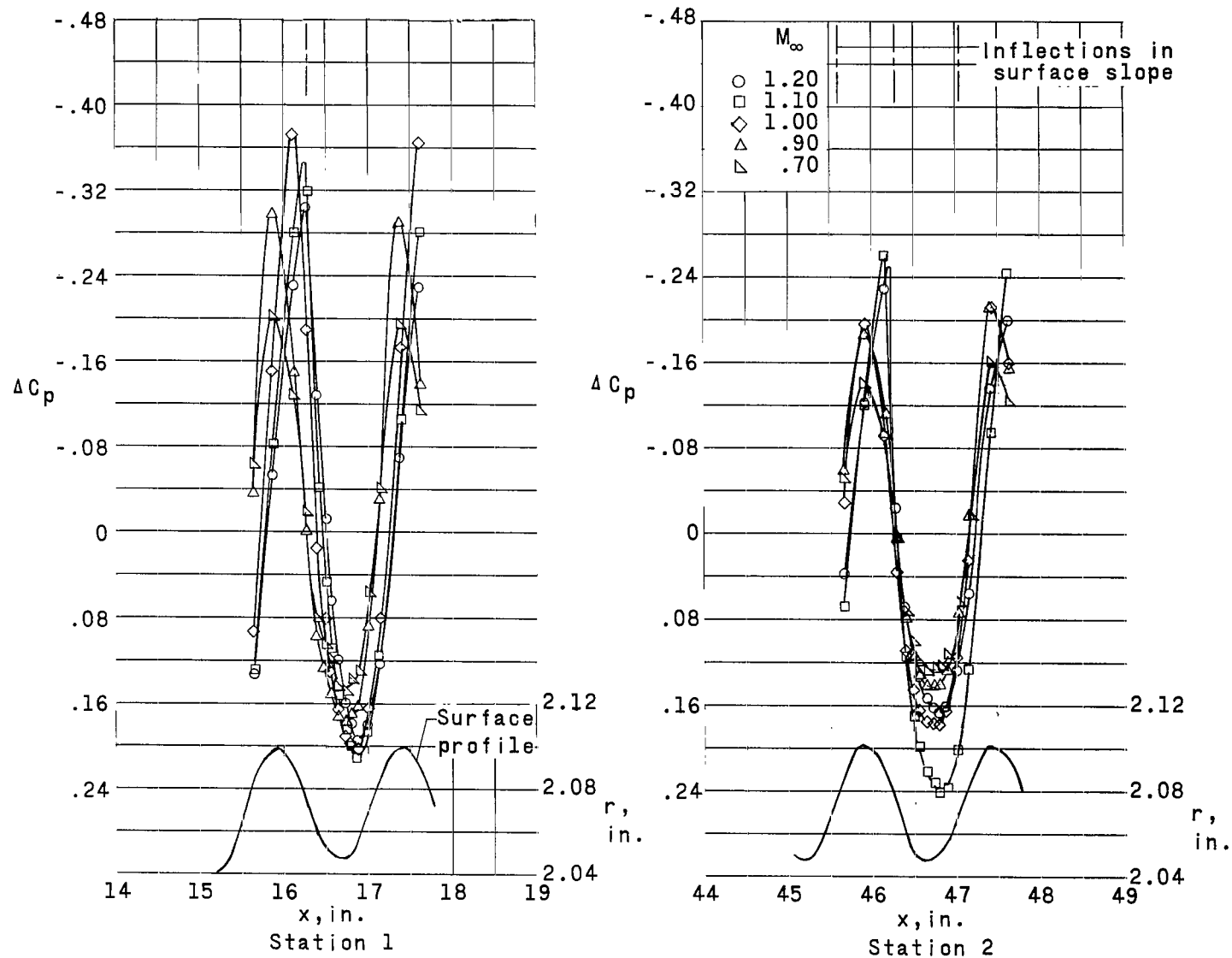
(a) p_t = 3000 psf.

Figure 13.-   Pressure distributions over model with 0.053-inch protruding waves at constant p_t.
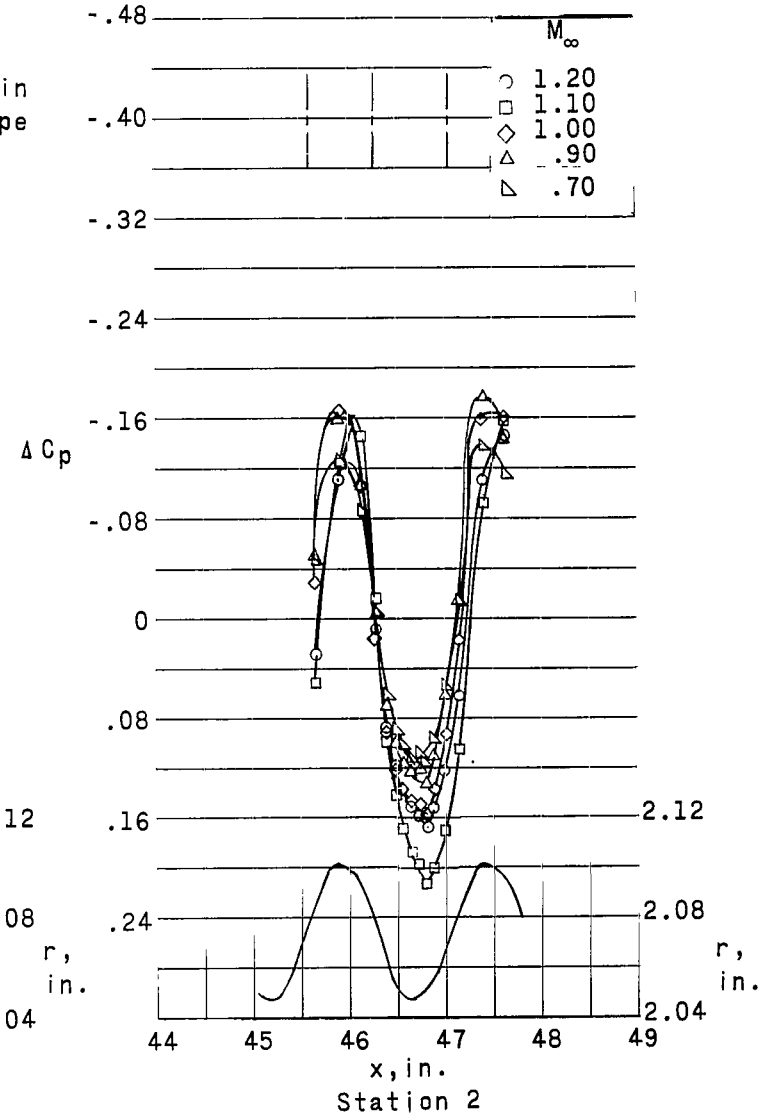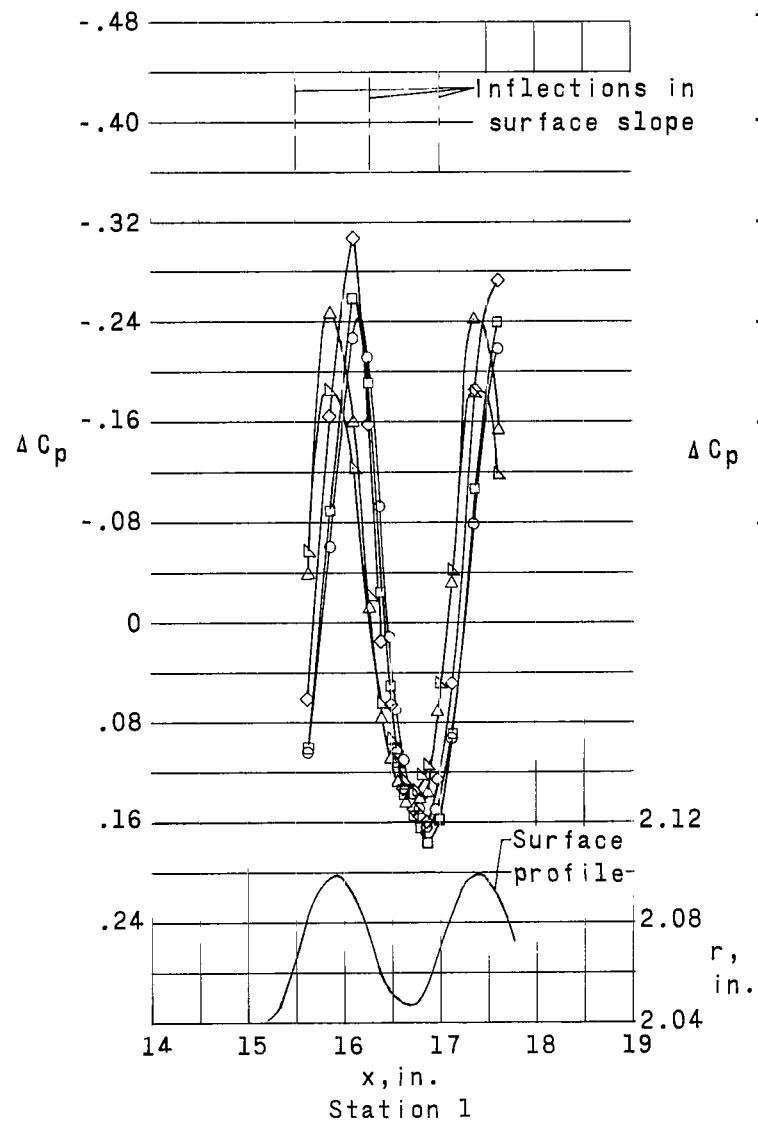
(b) p_t = 1000 psf.

Figure 13.- Concluded.
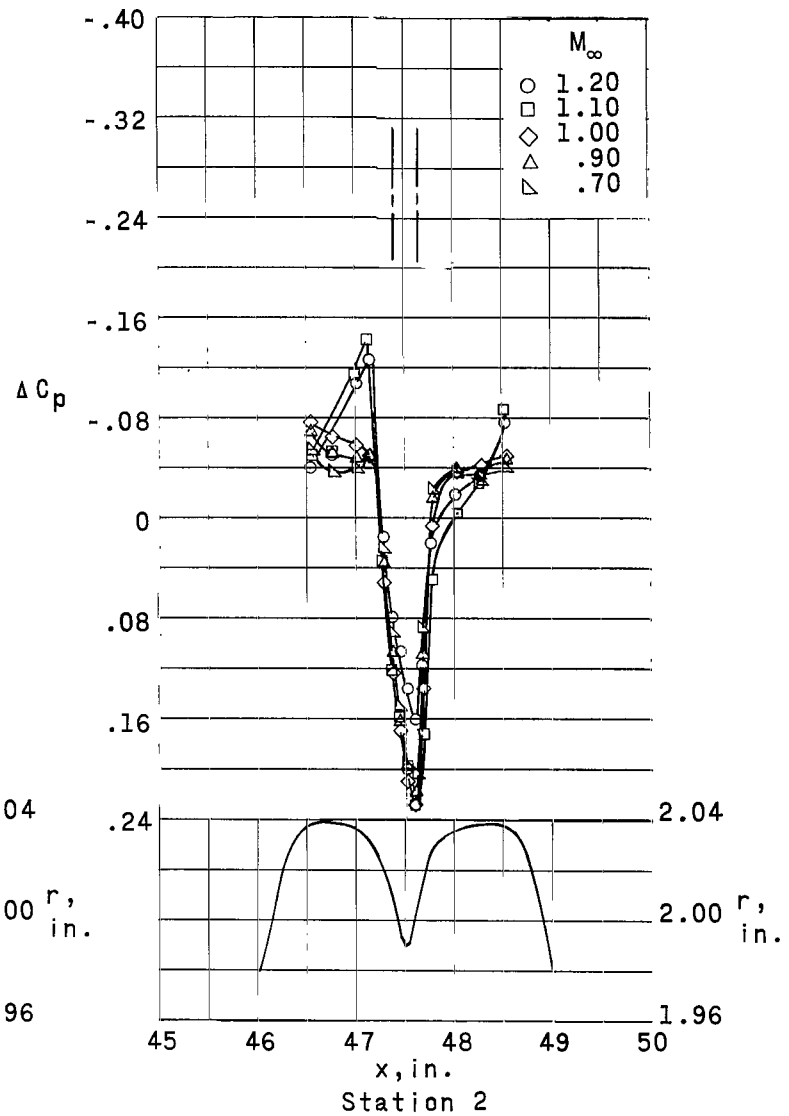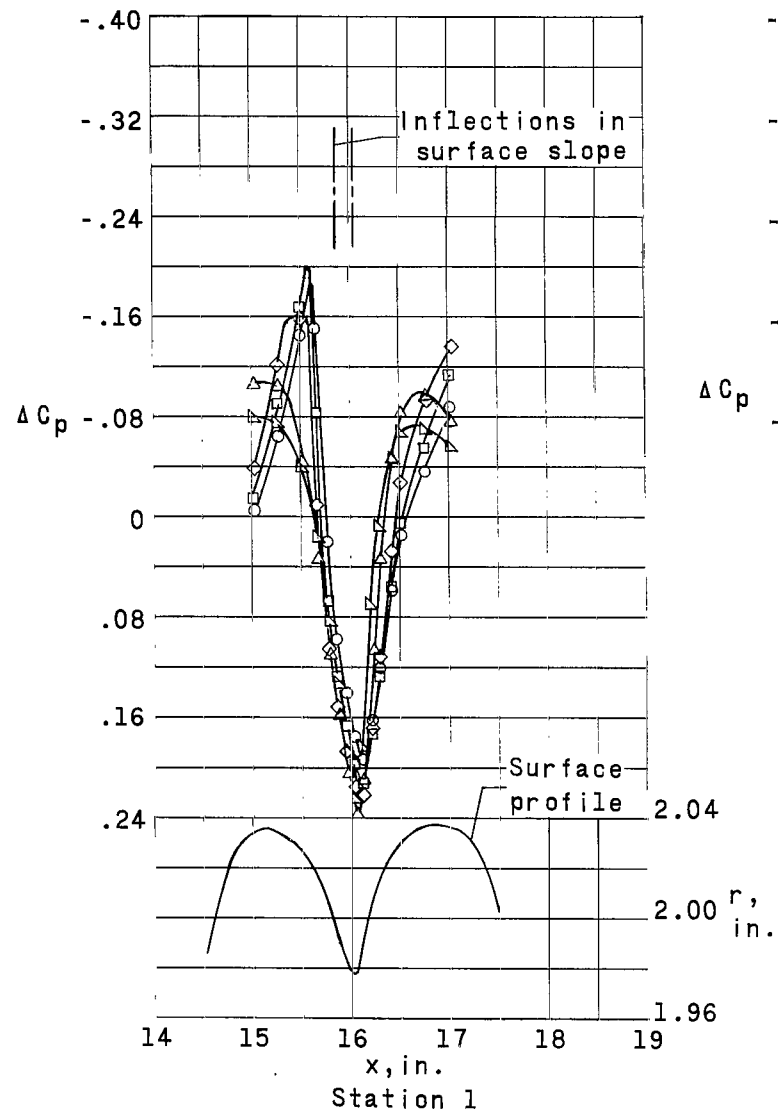
(a) p_t = 3000 psf.

Figure 14.- Pressure distributions over model with 0.053-inch transverse creases at constant p_t.
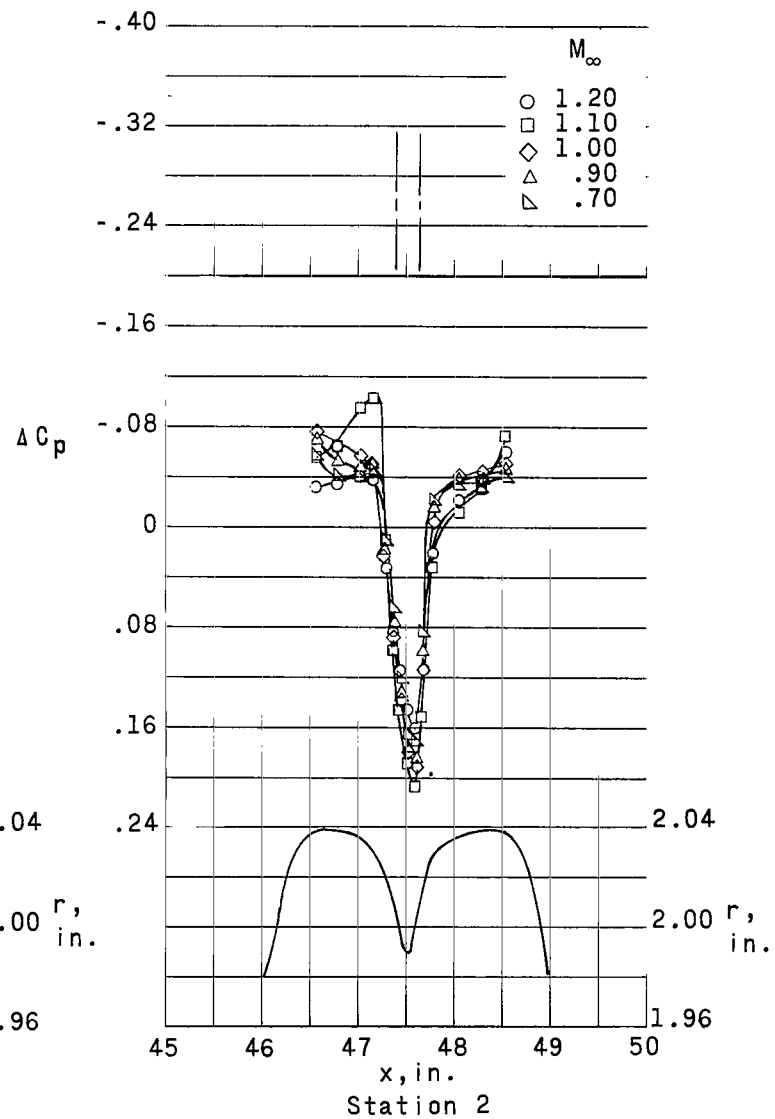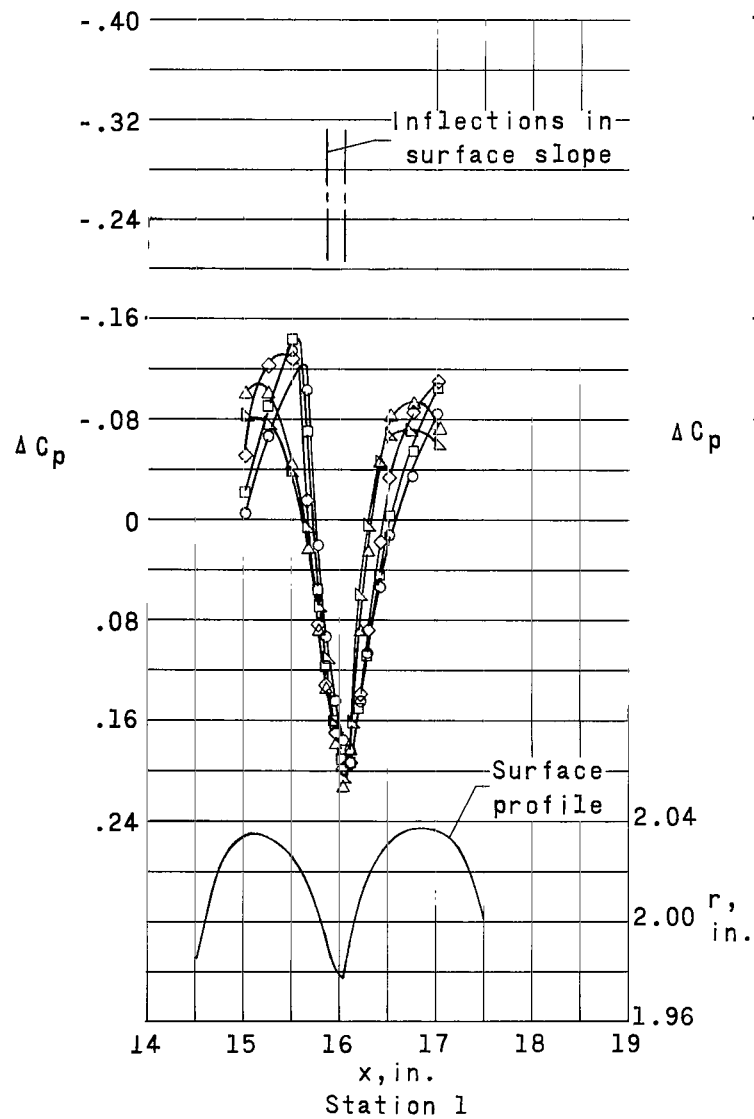
(b) $p_t = 1000$ psf.

Figure 14.- Concluded.
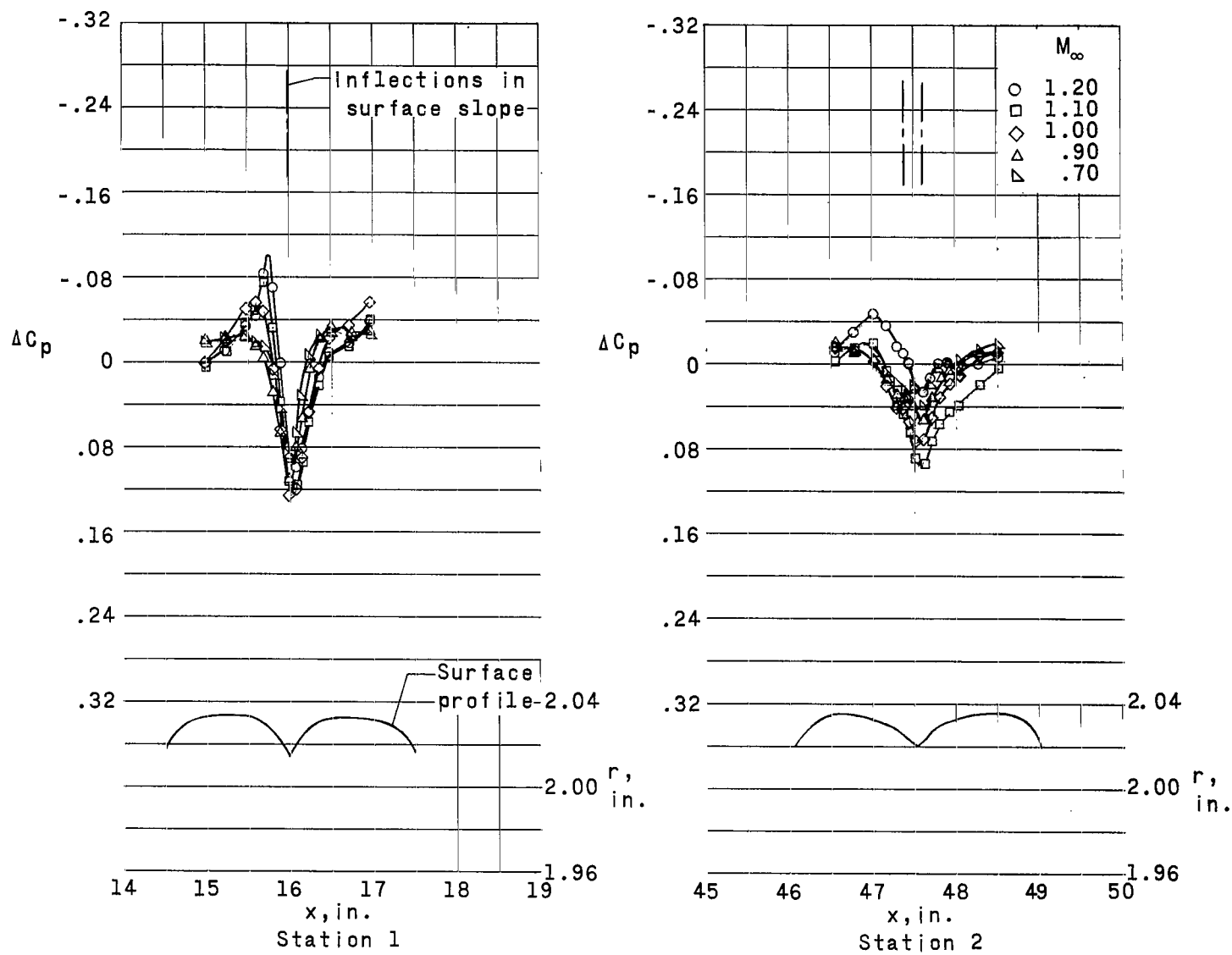
(a) p_t = 3000 psf.

Figure 15.- Pressure distributions over model with 0.017-inch transverse creases at constant p_t.
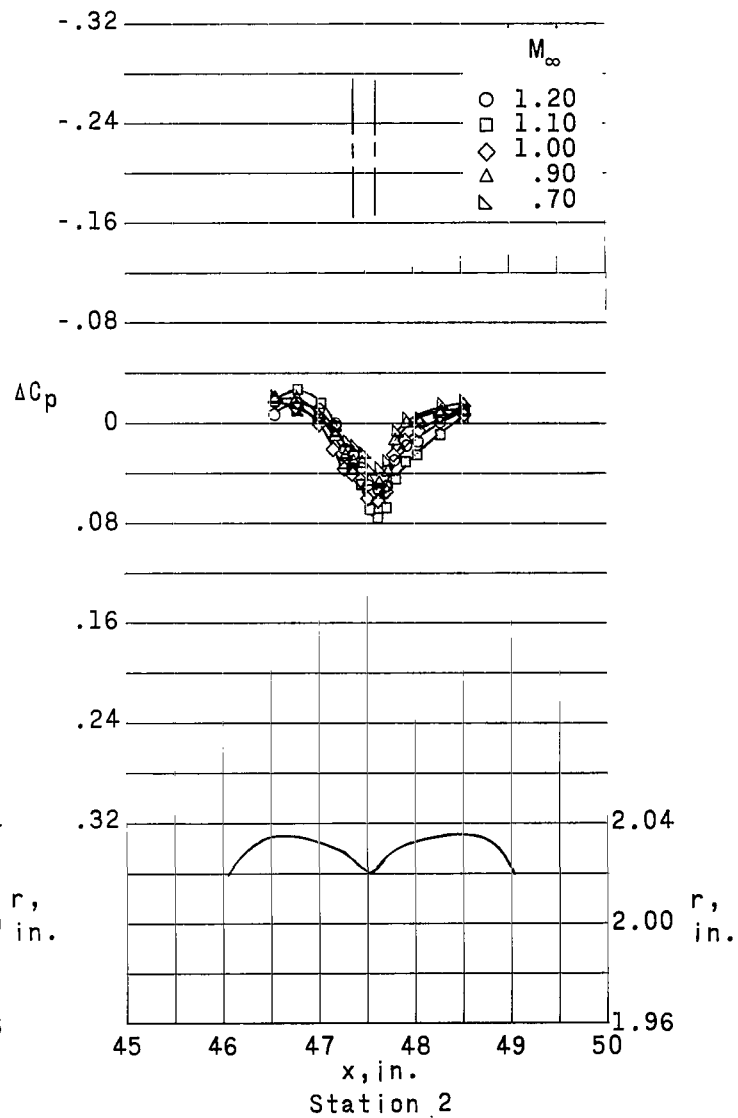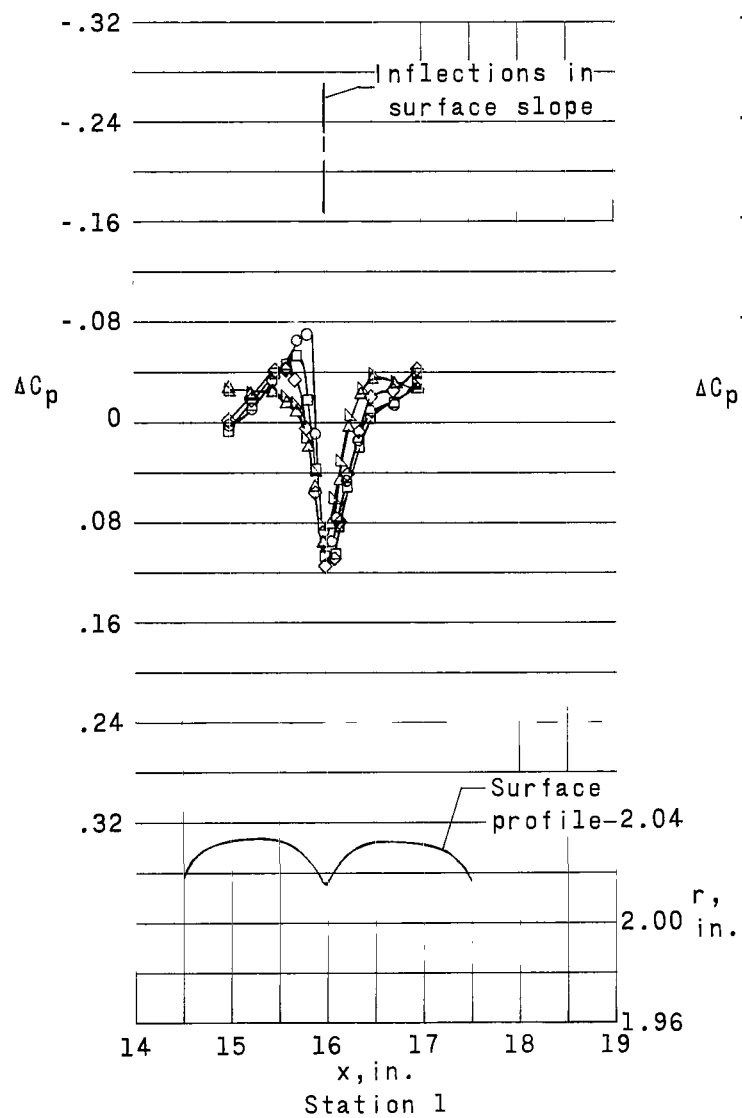
(b) $p_t = 1000$ psf.

Figure 15.- Concluded.
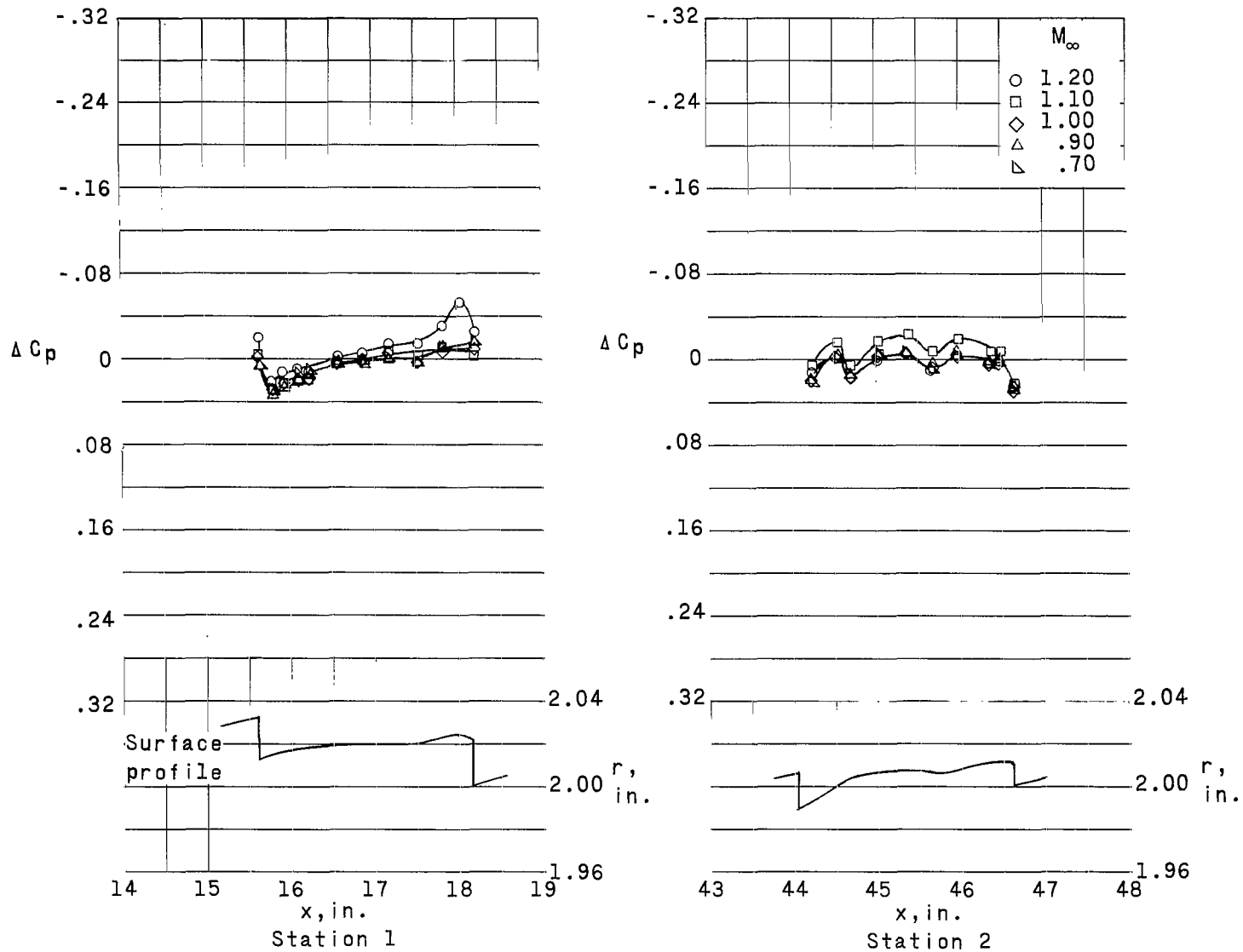
(a) p_t = 3000 psf.

Figure 16.- Pressure distributions over model with 0.020-inch 45⁰ rearward steps.
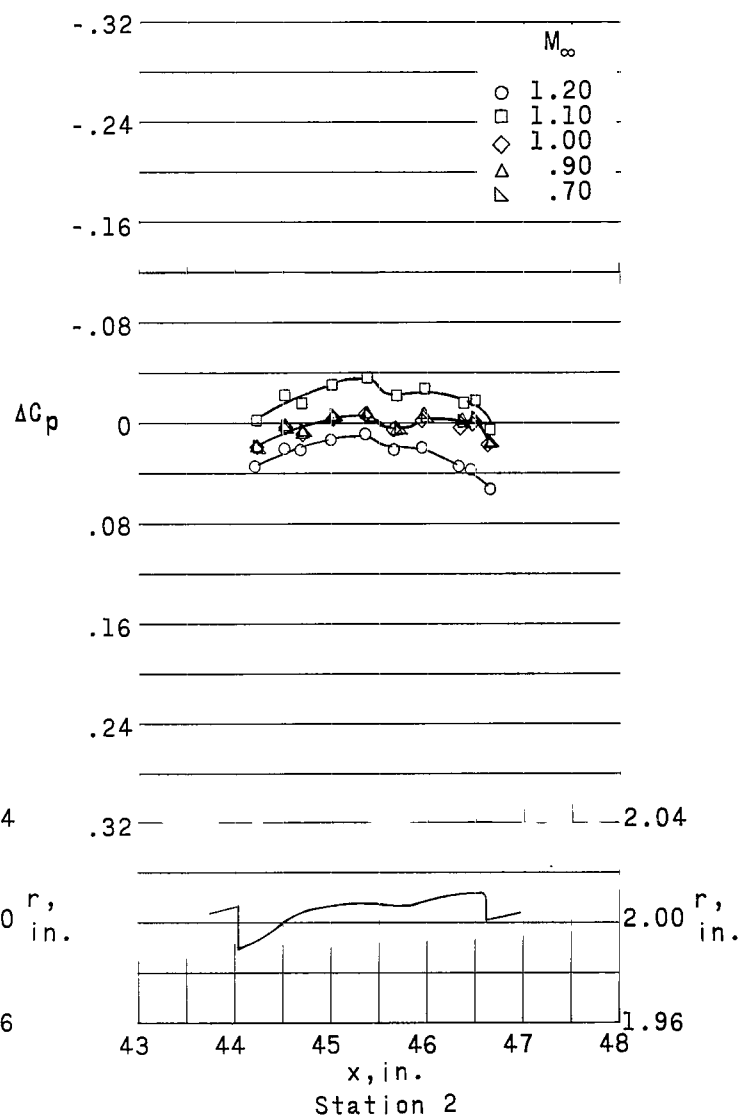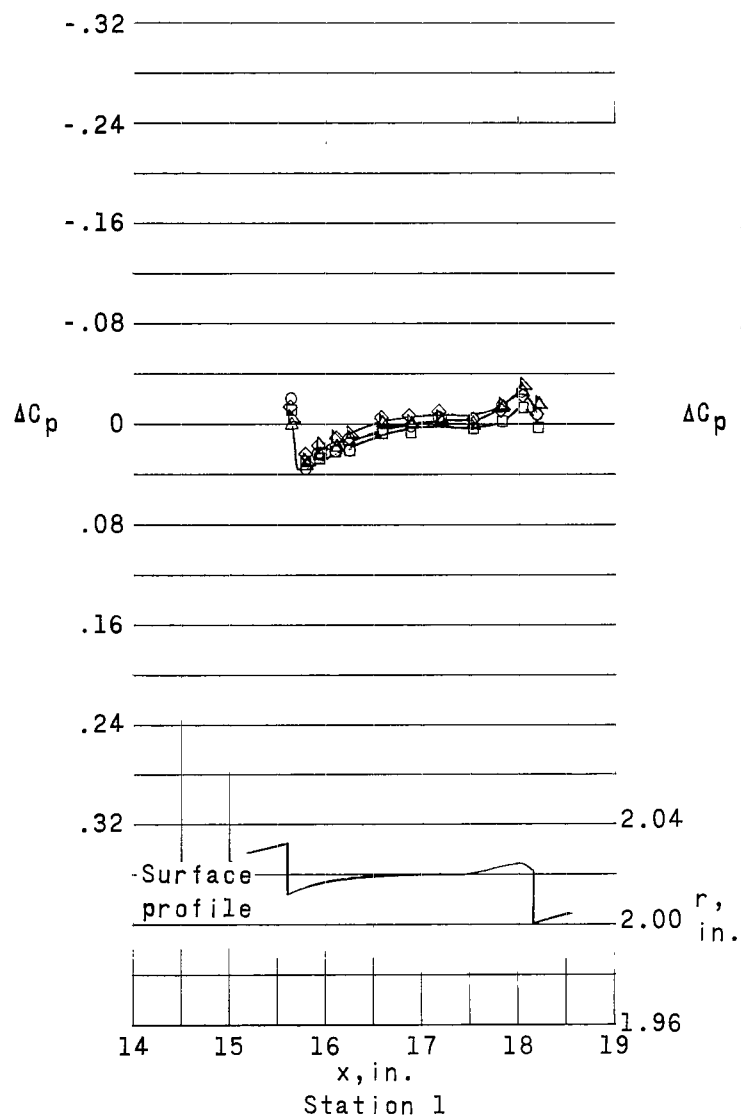
(b) $p_t = 1000$ psf.

Figure 16.- Concluded.
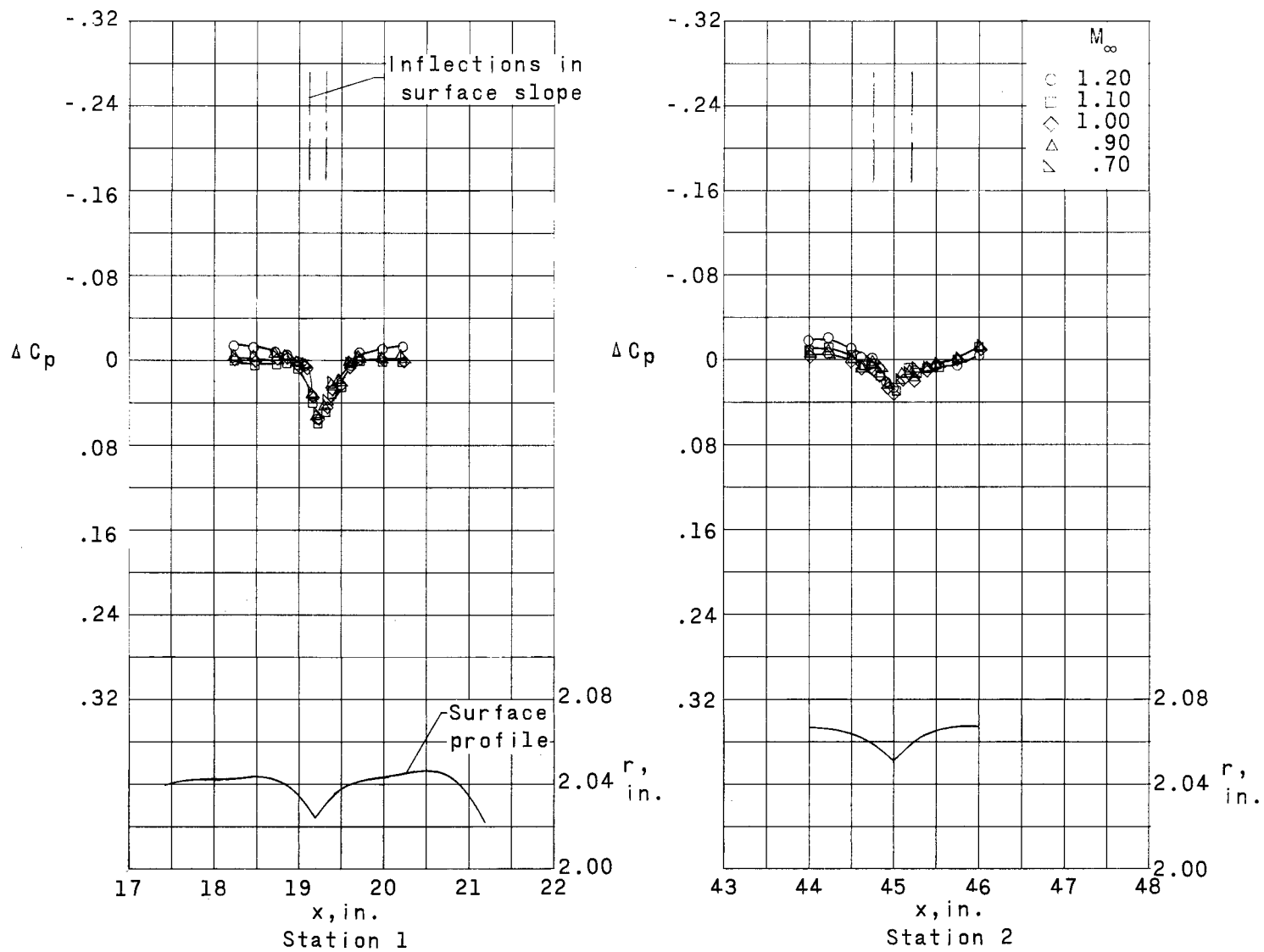
(a) p_t = 3000 psf.

Figure 17.- Pressure distributions over model with 0.014-inch 45^0 creases.
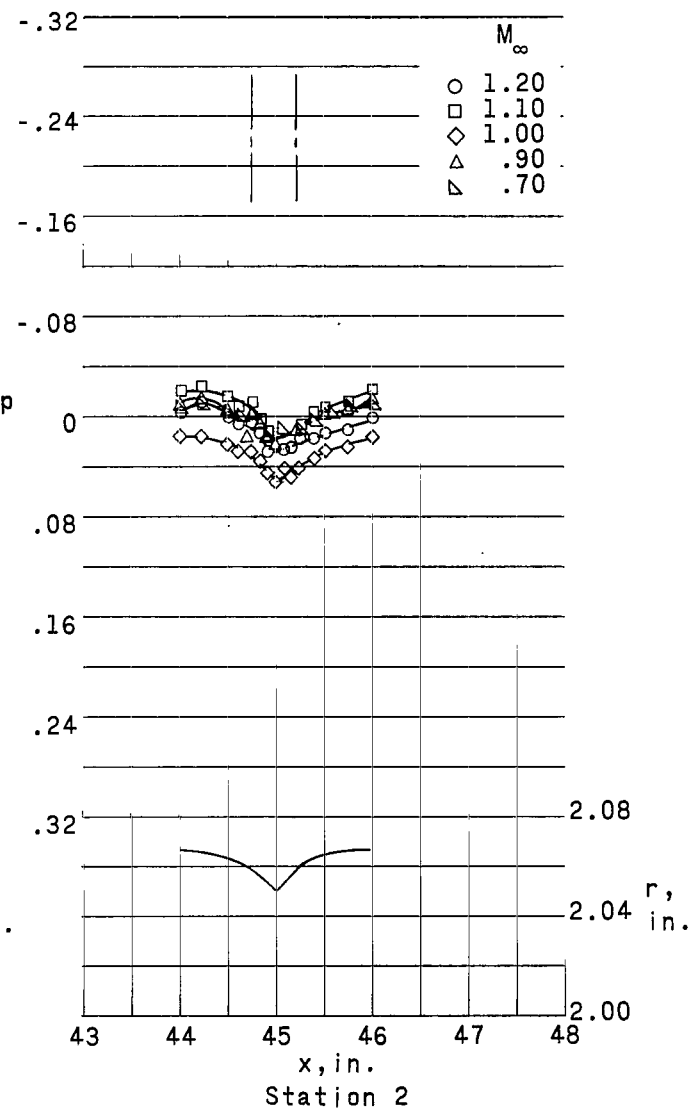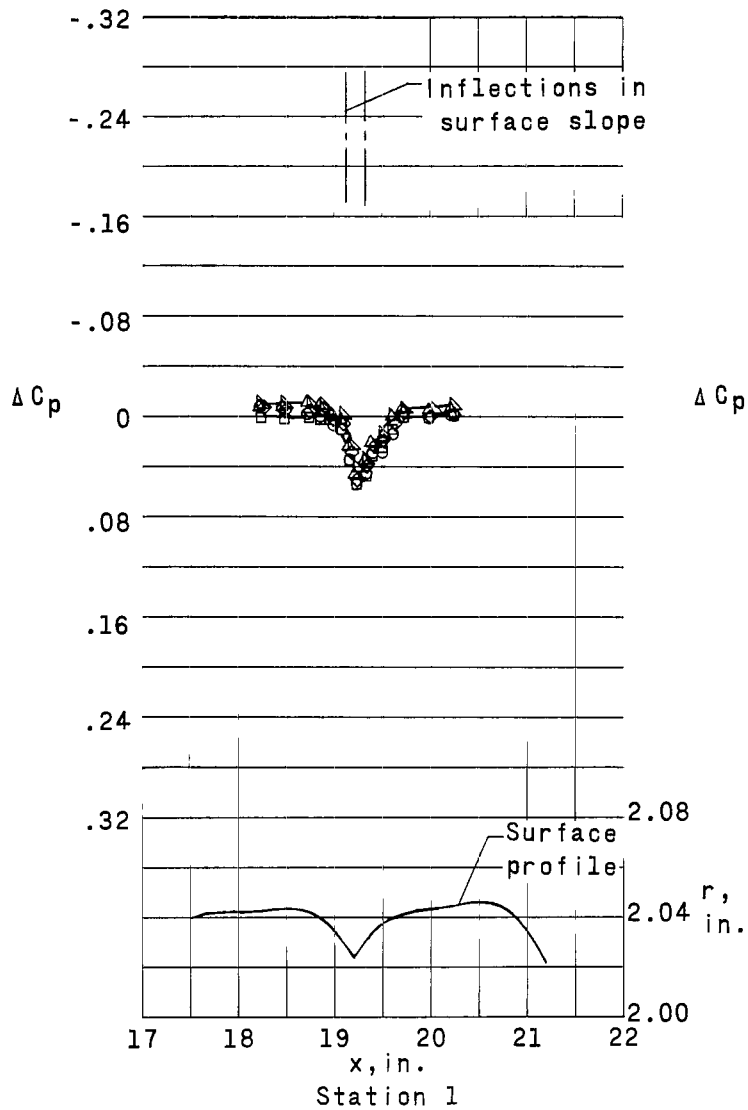
(b) $p_t = 1000$ psf.

Figure 17.- Concluded.
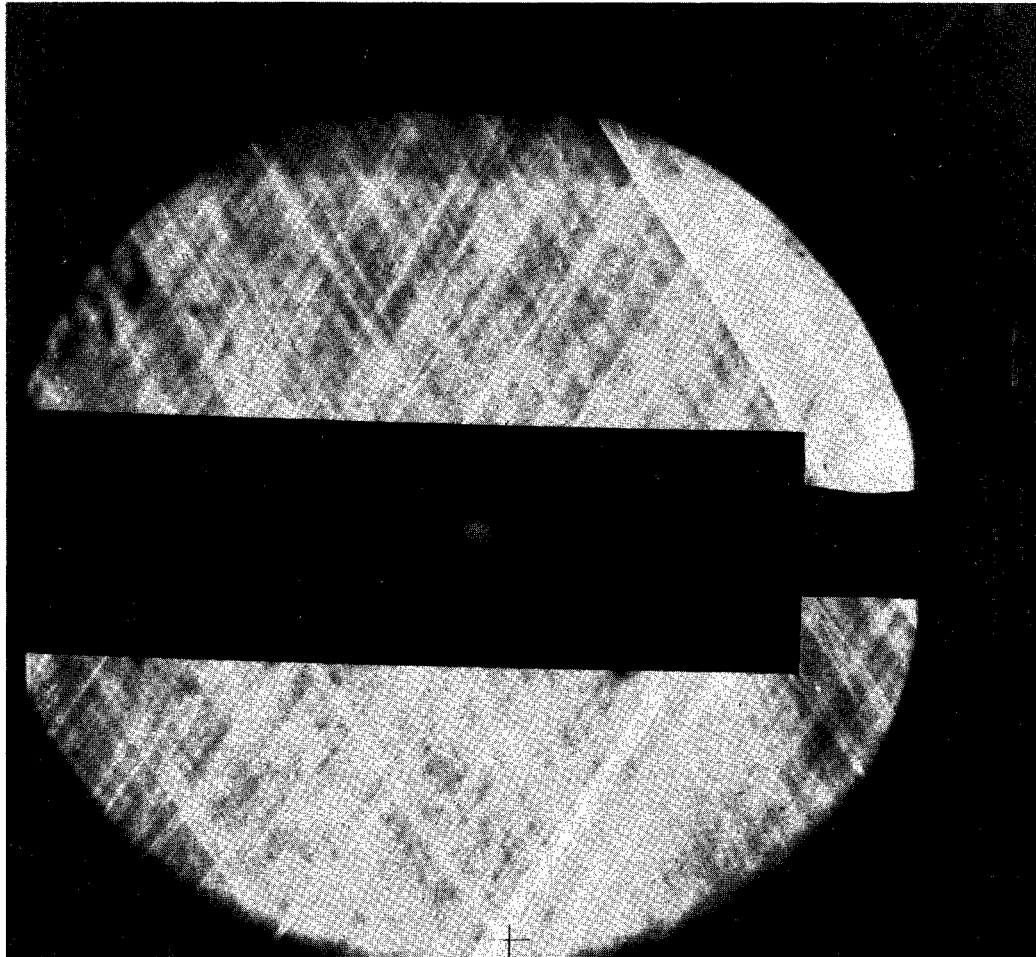
Figure 18.- Schlieren photograph of flow over rear part of basic smooth model. $M_\infty = 1.20$.

M$_\infty$

0.70

0.90

1.00

1.10

1.20
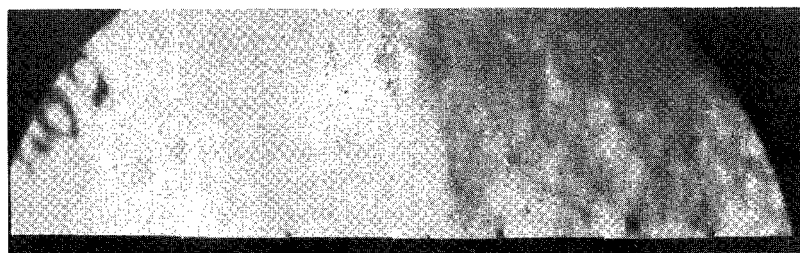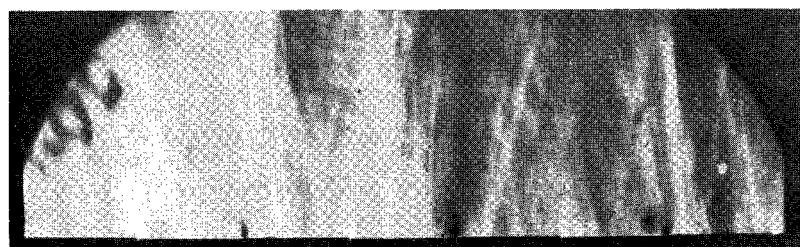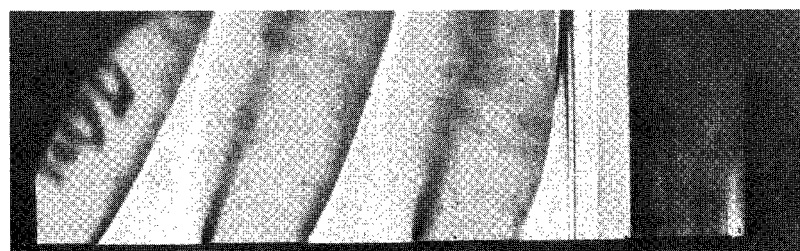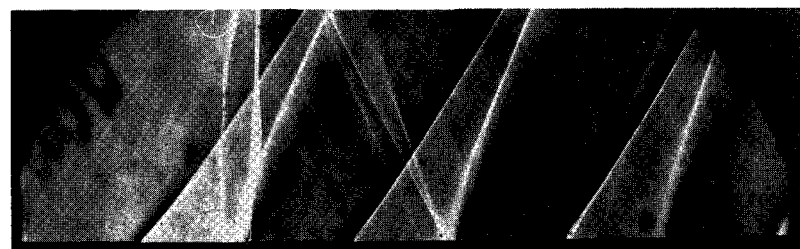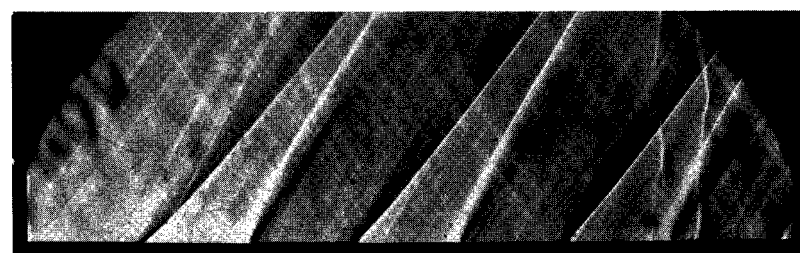
(a) In vicinity of station 1.

L-66-1125

Figure 19.-   Schlieren photographs of flow over model with 0.021-inch steps with grooves. Variable R/ft.

M_∞

0.70

0.90

1.00

1.10

1.20
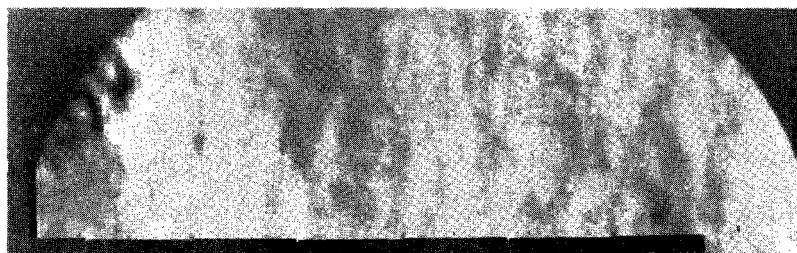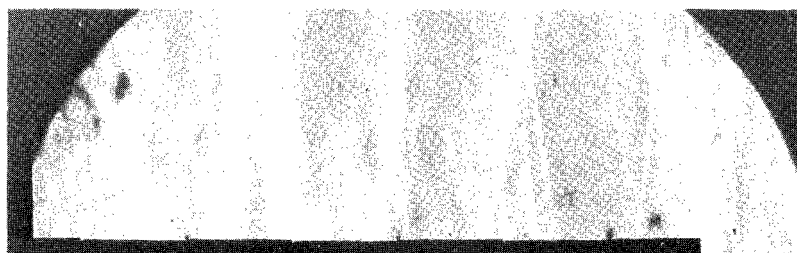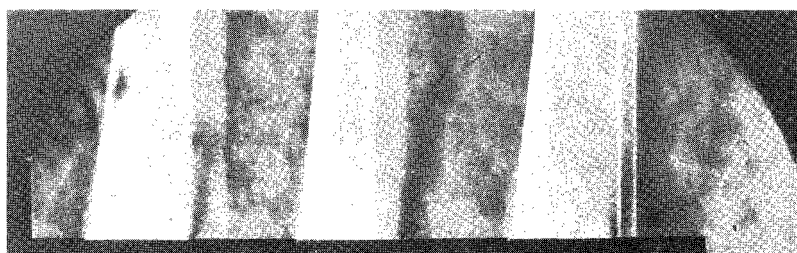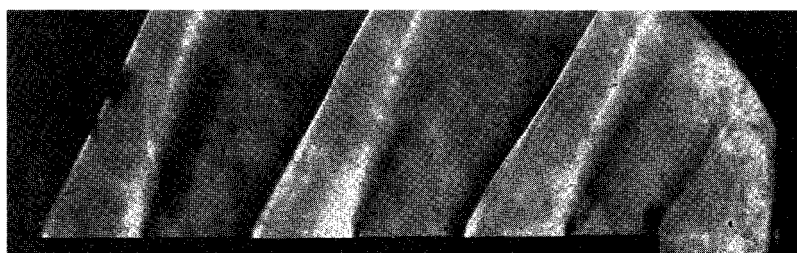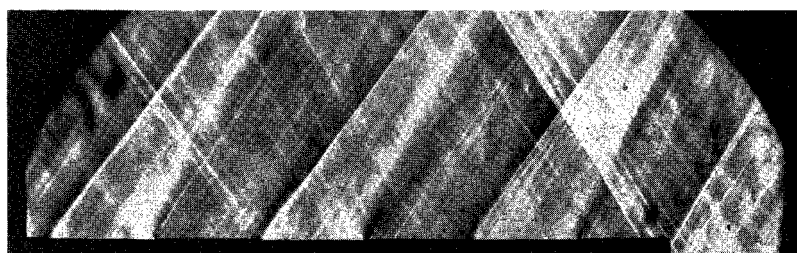
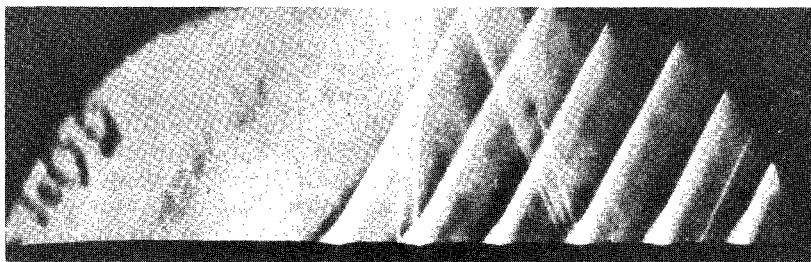(b) In vicinity of station 2.

L-66-1126

Figure 19.- Concluded.

Schlieren photograph
not available

M_∞

0.70

0.90

1.00

1.10

1.20
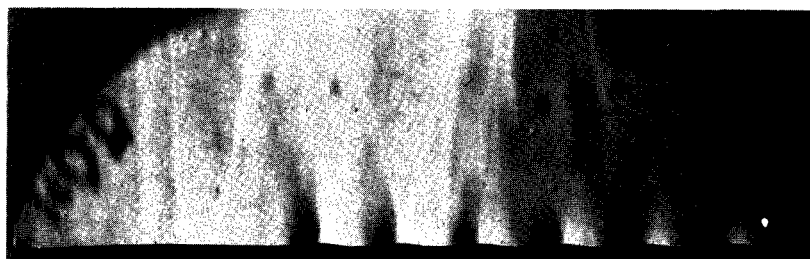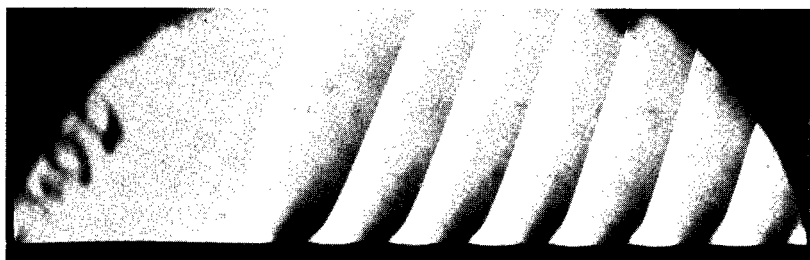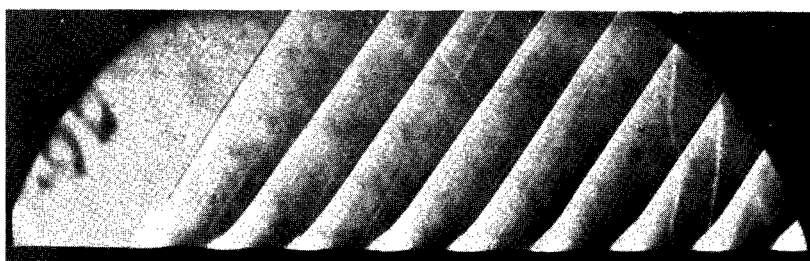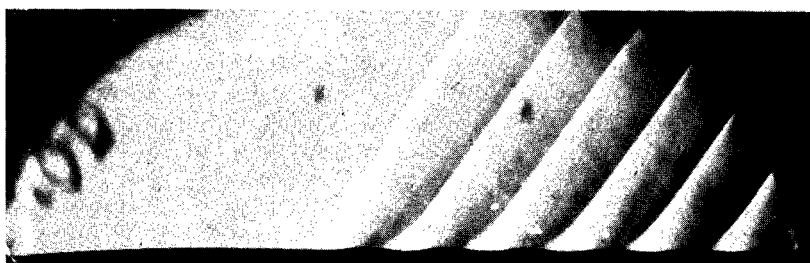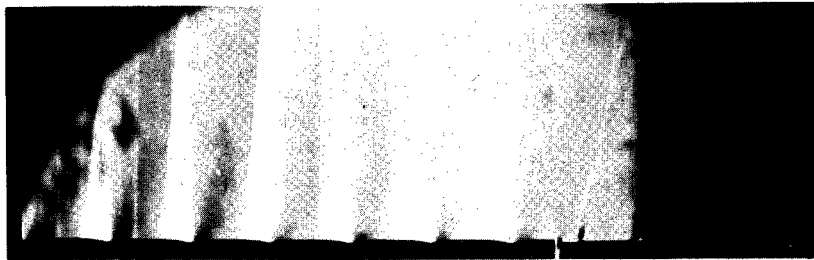
(a) In vicinity of station 1.   L-66-1127

Figure 20.-   Schlieren photographs of flow over model with 0.053-inch protruding waves. Variable R/ft.
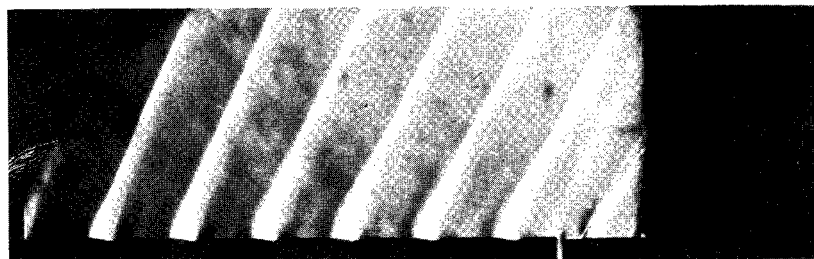
Schlieren photograph
not available

M_∞

0.70

0.90

1.00

1.10

1.20
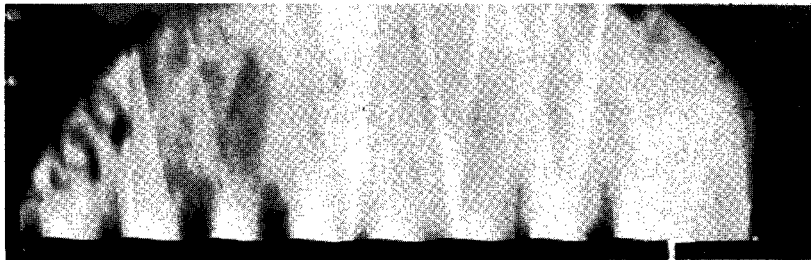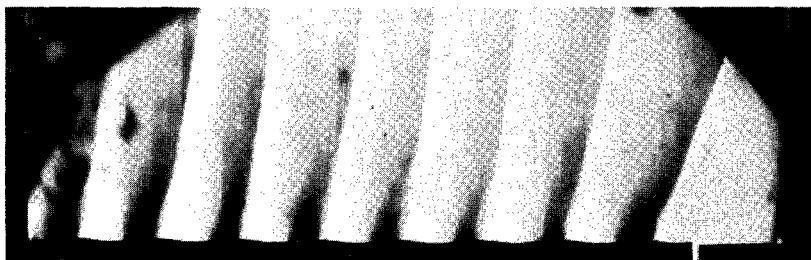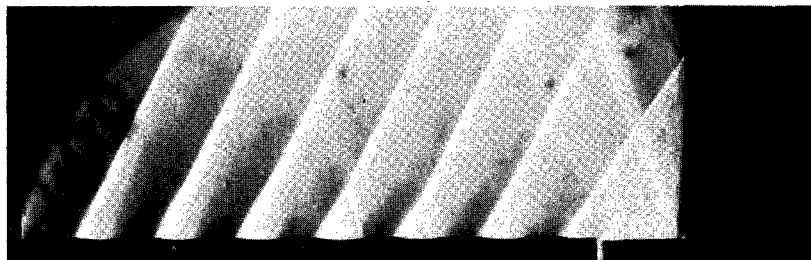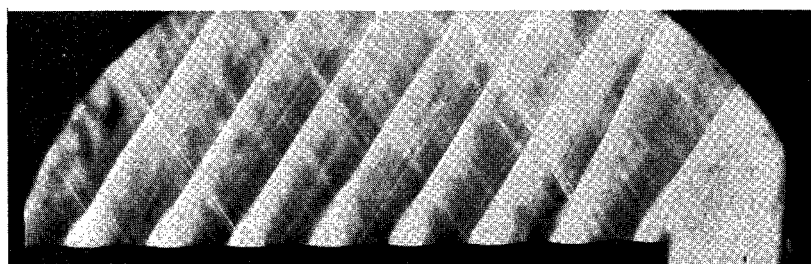
(b) In vicinity of station 2.

L-66-1128

Figure 20.- Concluded.
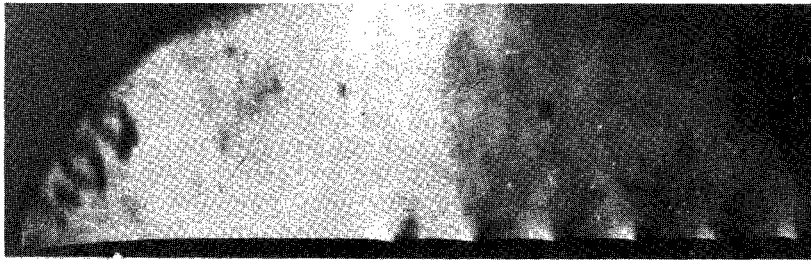
M$_\infty$

0.70

0.90

1.00

1.10
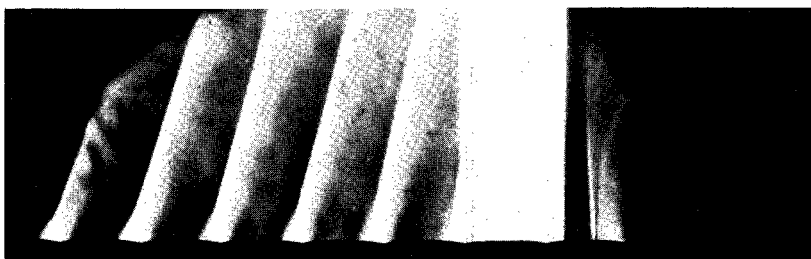
Schlieren photograph
not available

1.20

(a) In vicinity of station 1.

L-66-1129

Figure 21.- Schlieren photographs of flow over model with 0.053-inch transverse creases. Variable R/ft.

$$M_\infty$$

Schlieren photograph
not avilable

0.70

Schlieren photograph
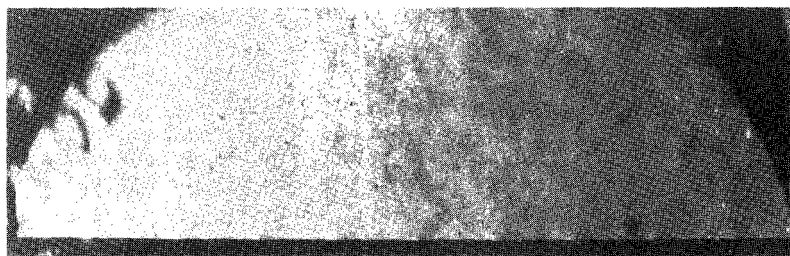not available

0.90

1.00

1.10

Schlieren photograph
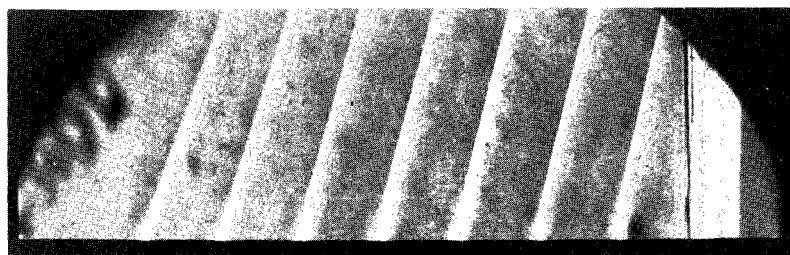not available

1.20

(b) In vicinity of station 2.
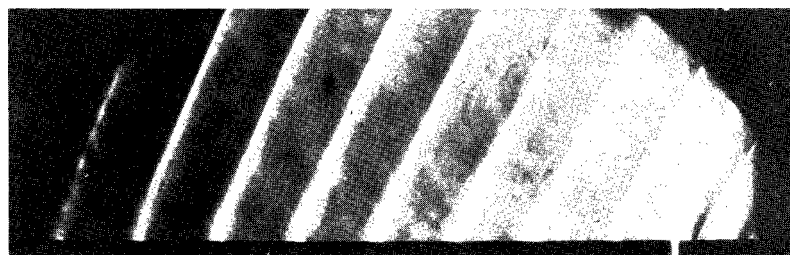
Figure 21.- Concluded.

L-66-1130

M_∞
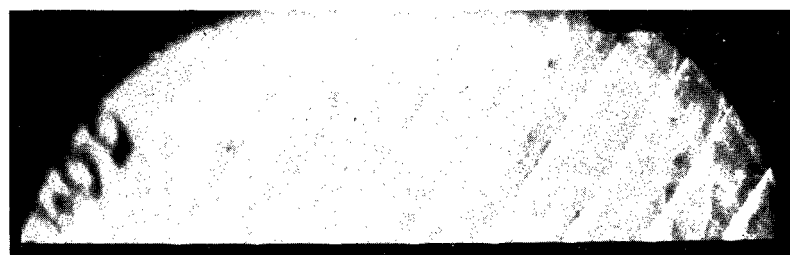
0.70

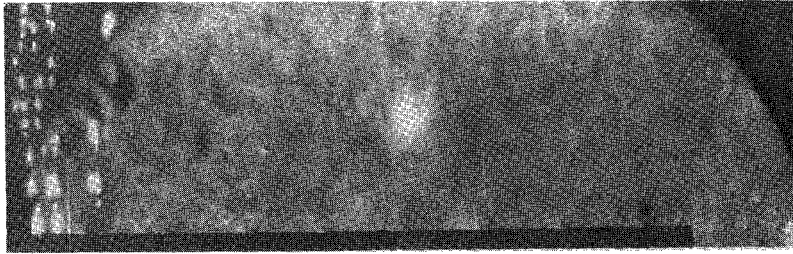Schlieren photograph
not available

0.90

1.00

1.10

1.20
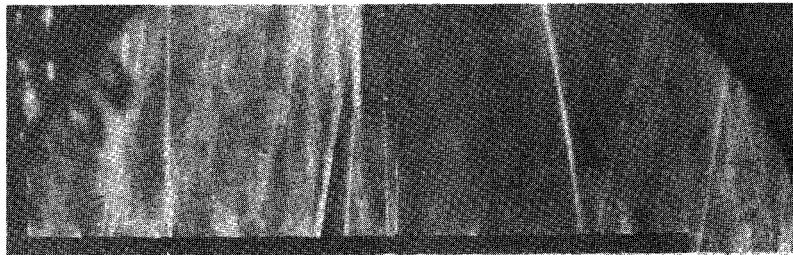
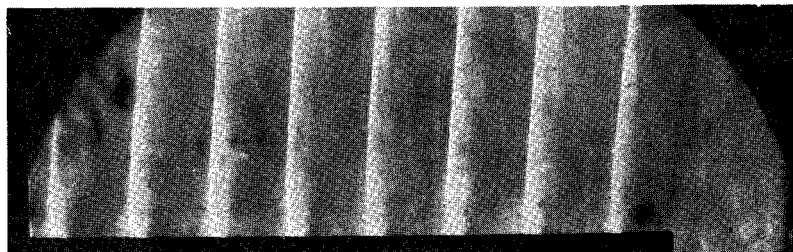(a) In vicinity of station 1.   L-66-1131

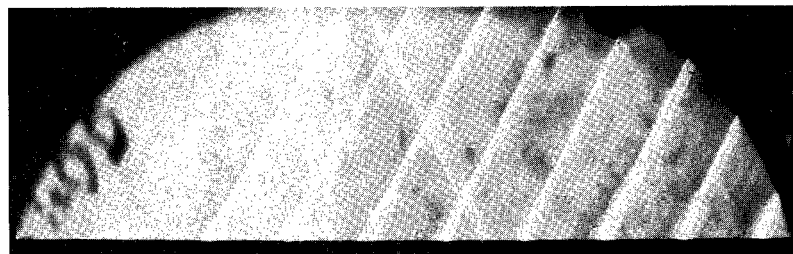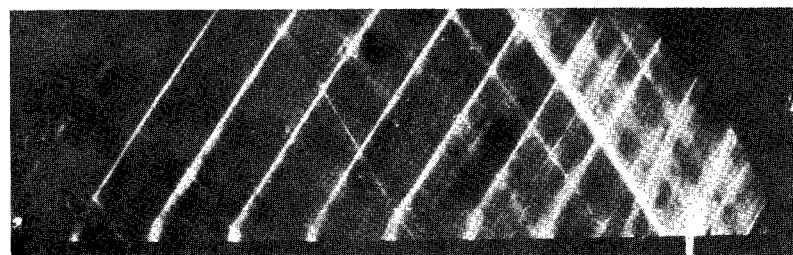Figure 22.- Schlieren photographs of flow over model with 0.017-inch transverse creases. Variable R/ft.

M_∞

0.70

0.90

1.00

1.10

1.20

(b) In vicinity of station 2.

Figure 22.- Concluded.

L-66-1132

78   NASA-Langley, 1966   L-4202

"The aeronautical and space activities of the United States shall be conducted so as to contribute . . . to the expansion of human knowledge of phenomena in the atmosphere and space. The Administration shall provide for the widest practicable and appropriate dissemination of information concerning its activities and the results thereof."

—NATIONAL AERONAUTICS AND SPACE ACT OF 1958

NASA SCIENTIFIC AND TECHNICAL PUBLICATIONS

TECHNICAL REPORTS: Scientific and technical information considered important, complete, and a lasting contribution to existing knowledge.

TECHNICAL NOTES: Information less broad in scope but nevertheless of importance as a contribution to existing knowledge.

TECHNICAL MEMORANDUMS: Information receiving limited distribution because of preliminary data, security classification, or other reasons.

CONTRACTOR REPORTS: Technical information generated in connection with a NASA contract or grant and released under NASA auspices.

TECHNICAL TRANSLATIONS: Information published in a foreign language considered to merit NASA distribution in English.

TECHNICAL REPRINTS: Information derived from NASA activities and initially published in the form of journal articles.

SPECIAL PUBLICATIONS: Information derived from or of value to NASA activities but not necessarily reporting the results of individual NASA-programmed scientific efforts. Publications include conference proceedings, monographs, data compilations, handbooks, sourcebooks, and special bibliographies.

Details on the availability of these publications may be obtained from:

SCIENTIFIC AND TECHNICAL INFORMATION DIVISION

NATIONAL AERONAUTICS AND SPACE ADMINISTRATION

Washington, D.C. 20546